A DETERMINATION OF THE EFFECT OF THE DISPERSIVE TERM ON THE FRESNEL DRAG COEFFICIENT USING A RING LASER

By

ALFRED TED ZAVODNY

Bachelor of Science
Oklahoma State University
Stillwater, Oklahoma
1962

Master of Science
Oklahoma State University
Stillwater, Oklahoma
1965

Submitted to the Faculty of the
Graduate College of the
Oklahoma State University
in partial fulfillment of
the requirements for
the Degree of
DOCTOR OF PHILOSOPHY
May, 1970

Thesis
1970 D
Z39d
cop. 2

OKLAHOMA STATE UNIVERSITY LIBRARY
OCT 15 1970

A DETERMINATION OF THE EFFECT OF

THE DISPERSIVE TERM ON THE

FRESNEL DRAG COEFFICIENT

USING A RING LASER

Thesis Approved:

Hans R. Bilger
Thesis Adviser

Wm. F. Hughes

Arthur M. Breipohl

A. O. Fingelbrech

W. J. Seiwo

D. Durham
Dean of the Graduate College

762881

PREFACE

This dissertation is concerned with experimentally determining the Fresnel drag coefficient of light in a moving medium. Equations are given for the theoretical effect of medium motion on the propogation velocity of light both neglecting and including the effects of dispersion. Experimental determination of the drag coefficient was obtained through the use of a ring laser operating at 6328 Å. The frequency separation of the contracirculating beams was monitored and recorded when a moving medium was introduced into one arm of the ring, and was later used to calculate the magnitude of the drag coefficient. Consideration is also given to the bias which results from the earth's diurnal rotation.

The experimental equipment, prodecure, and results are discussed in detail. A gas flow was utilized during early measurements to avoid the phenomenon of "lock-in". Extensive drag coefficient data was obtained for fused silica. Motion of the fused silica relative to the ring laser was achieved by inserting an optic flat of fused silica into the beams at its Brewster angle and rotating the optic flat in a special rotator assembly. Several problems associated with the extension of these methods to liquid measurements were also studied. Suggestions for improving the system to allow more precise measurement of the drag coefficient for solids and to allow measurement of the drag coefficient of liquids are also presented.

I would like to take this opportunity to express my appreciation to

the members of my committee: Dr. Hans R. Bilger, adviser, who suggested the problem and offered many suggestions toward its solution; and Dr. William L. Hughes, Dr. Dan D. Lingelbach, Dr. Arthur M. Breipohl, and Dr. William J. Leivo for their interest and assistance. I want to acknowledge the advice and craftsmanship of Mr. Heinz Hall, O. S. U. Physics Department Machine Shop, for his contributions to solving mechanical problems encountered in this work. I would also like to express my appreciation to the many people at Continental Oil Company for their support and assistance in this work: Mr. David B. Burrows and Mr. Laymond D. Wann, for their personal efforts in allowing unique work schedules and in the loaning of considerable electronics equipment from Continental Oil Company to this work; Dr. Dale Cooper, for his mathematical and statistical assistance; Mr. Kent Jones, for his supurb equipment fabrication; and to the several employees in the Electronics Laboratory, for their continued encouragement.

Especially, I would like to express appreciation to my wife, Shirley, daughter, Catherine, and son, Kevin, for their understanding, encouragement, and tremendous personal sacrifice which allowed this dissertation to be undertaken and completed. It is in light of the above that this writing is in dedication to my daughter, Catherine, and son, Kevin.

TABLE OF CONTENTS

Chapter		Page
I.	INTRODUCTION	1
	Historical Background	2
	Experimental Method	4
	Results Obtained	5
II.	THEORETICAL TREATMENT	7
	Fresnel's Drag Coefficient	7
	Dispersive Term in the Drag Coefficient	9
	Equations of the Ring Laser	11
	General Description of a Ring Laser	11
	Modes in a Ring Laser	12
	Effects Due to Rotating a Ring Laser	13
	Moving Medium in a Ring Laser	14
	Effects of Direction of Motion Relative to the Ring Laser	18
	Evaluation of the Drag Coefficient	18
	Ultimate Accuracy Attainable With the Ring Laser	20
III.	EXPERIMENTAL APPARATUS	24
	Description of the Equipment	24
	Ring Laser Drag Sensor	24
	Beam Combiner	30
	Optical Detector	37
	Beat Frequency Signal Processing Section	38
	Data Accumulation Equipment	45
	Moving Medium	49
	Velocity Detection Systems	64
	Peripheral Measuring Equipment	65
	Operation of the Equipment	70
IV.	EXPERIMENTAL PROCEDURE	76
	Gases	76
	Solids	78
	Static Measurements	78
	Dynamic Measurements	81
	Data Accumulation	82
	Liquids	83

Chapter Page

V. EXPERIMENTAL RESULTS 85

Introduction 85
Gas Measurements 85
Solid Measurements 90
Static Measurements 91
Dynamic Measurements 98
Liquid Measurements 126

VI. CONCLUSIONS AND SUGGESTIONS FOR IMPROVEMENT 132

Conclusions 132
Suggestions for Improvement 134

BIBLIOGRAPHY 139

GLOSSARY OF SYMBOLS 142

APPENDIX A - AXIAL MODE EQUATIONS FOR A LINEAR LASER 146

APPENDIX B - AXIAL MODE SEPARATION MEASUREMENTS FOR THE RING LASER CONTAINING THE OPTIC FLAT AND COMPENSATOR FLAT 149

APPENDIX C - AXIAL MODE SEPARATION MEASUREMENTS FOR A LINEAR OSCILLATOR CONTAINING A SAMPLE 152

APPENDIX D - A VECTOR EVALUATION OF THE VELOCITY COMPONENT OF A ROTATING CYLINDER ALONG AN INTERSECTING RAY . . . 154

APPENDIX E - EQUIPMENT USED IN THE EXPERIMENTS 162

LIST OF TABLES

Table		Page
I.	Optic Flat Specifications	62
II.	Primary Equipment Utilized in the Experiments	73
III.	Calculated Effect of the Dispersion Term on the Drag Coefficient	77
IV.	Tabular Representation of Figure 24	88
V.	Tabular Representation of Figure 25	88
VI.	Statistical Results of Resetting Radius to 1.72 cm Under Controlled Conditions	92
VII.	Measurement Errors	96
VIII.	Data for Determining X-Axis Vernier Misorientation Angle	98
IX.	Repeatibility Data for Determining the Center of the Fused Silica Optic Flat	99
X.	Raw Data for a Typical Data Point (f_ω, Δf_B)	101
XI.	Distribution of Individual Data Points of a Representative Data Collection	104
XII.	Distribution of DELTA $\Delta f_B/\sigma_{\Delta(\Delta f_B)}$ Data for a Typical Least Squares Fit	104
XIII.	Tabular Representation of Figure 28	107
XIV.	Tabular Representation of Figure 29	109
XV.	Tabular Representation of Figure 30	112
XVI.	Tabular Representation of Figure 31	114
XVII.	Tabular Representation of Figure 32	116
XVIII.	Tabular Representation of Figure 33	118

Table		Page
XIX.	Computed Terms for a Least Squares Fit to a Straight Line y = mx + b	122
XX.	Comparison of Experimental and Theoretical Drag Coefficients	125
XXI.	Index of Refraction and Dispersion of Selected Liquids	128
XXII.	Transmission Loss Through Liquid Cell	129
XXIII.	X-Y Translators	135
XXIV.	First Axial Mode Separation for the Ring Laser Cavity Containing Optics	149
XXV.	Second Axial Mode Separation for the Ring Laser Cavity Containing Optics	150
XXVI.	Third Axial Mode Separation for the Ring Laser Cavity Containing Optics	150
XXVII.	Statistical Data for Axial Mode Separations in the Ring Laser Cavity Containing Optics	151
XXVIII.	Axial Mode Separation for the Linear Laser Without a Sample	152
XXIX.	Axial Mode Separation for the Linear Laser Containing the Oriel Optics Optic Flat	153
XXX.	Statistical Data for Axial Mode Separation in the Linear Laser Both Without and Containing the Oriel Optics Optic Flat	153
XXXI.	A Complete List of the Equipment Utilized in the Experiments	160

LIST OF ILLUSTRATIONS

Figure		Page
1.	Block Diagram of the Equipment for Taking Measurements of Beat Frequency vs. Velocity (or Frequency of Rotation)	25
2.	Ring Laser and Vibration Isolated Table Top	27
3.	Beam Combiner	33
4.	Schematic of the Beam Combiner	34
5.	Schematic of the Photomultiplier Circuit	40
6.	Schematic of the Passive Signal Clipper	41
7.	Schematic of the Model 502 Oscilloscope Modification	43
8.	Trigger and Reset Schematic for Synchronizing the hp 5280A With the hp 5243L	46
9.	Electronic Equipment for Presenting Beat Frequency and Frequency of Rotation Data	48
10.	Flow Tube Used With Gas Flows	50
11.	Axes Orientation for the Moving Medium	52
12.	Beam Path Through the Moving Medium Illustrating the Tangential Velocity Projection	53
13.	Illustration of the Effect of X-Axis Misorientation on Velocity Determination	54
14.	Rotator Platform Used for Rotating the Solid and Liquids	55
15.	Top View of Adjustable Platform for Holding Moving (Rotated) Medium	56
16.	Side View of Adjustable Platform for Holding Moving Medium in Rotator	57
17.	Schematic of Sleeve and Bearing for Rotating the Fused Silica Optic Flat	59

Figure Page

18. Sleeve and Bearing Assembly Used for Rotating the Fused Silica Optic Flat 60

19. Block Diagram of Apparatus Used to Measure $\Delta\nu_{axial}$ 66

20. Diagram of the Equipment Used to Determine n by Measuring θ_B 68

21. Block Diagram of the Scheme Used to Measure Transmission Losses Through Liquids 69

22. Pictorial View of the Equipment Used in the Experiments . . 71

23. Pictorial View of the Vibration Isolated Table and Associated Equipment 72

24. Beat Frequency vs. Velocity for Nitrogen Gas Flow in a 5.0 mm Bore Tube - Trial 1 86

25. Beat Frequency vs. Velocity for Nitrogen Gas Flow in a 5.0 mm Bore Tube - Trial 2 87

26. Distribution of Individual Data Points for R = 2.00 cm in Figure 29 102

27. Distribution of DELTA $\Delta f_B/\sigma_{\Delta(\Delta f_B)}$ Data from Table XVI and Table XVII 103

28. Beat Frequency vs. Frequency of Rotation for Fused Silica for Constant Radius and Variable Frequency of Rotation . . 106

29. Beat Frequency vs. Frequency of Rotation for Fused Silica for Constant Radius and Variable Frequency of Rotation for Frequency of Rotation $\leq$ 1000 RPM 108

30. Beat Frequency vs. Frequency of Rotation for Fused Silica for R = 18.1 mm 111

31. Beat Frequency vs. Velocity for Fused Silica With Data Taken for Variable Frequency of Rotation and Constant Radius 113

32. Beat Frequency vs. Frequency of Rotation for Fused Silica With Data Taken for Variable Radius and Constant Frequency of Rotation 115

33. Beat Frequency vs. Velocity for Fused Silica With Data Taken for Constant Frequency of Rotation and Variable Radius 117

Figure Page

34. Beat Frequency vs. Frequency of Rotation for Fused Silica With Data Taken for Constant Frequency of Rotation 119

35. Diagram of Side View of Liquid Cell Illustrating Scattering Observed During Transmission Loss Measurements 130

36. Schematic of a Linear Laser Cavity 147

37. Right Cylinder With Coordinate System Illustrating Beam Penetration 155

38. Relationships for $\overrightarrow{L_r}$ Parallel to the X-Y Plane 161

39. Illustrating $\overrightarrow{L_{xy}}$ Generation From $\overrightarrow{L_r}$ 161

CHAPTER I

INTRODUCTION

The problem of interest in this dissertation was to experimentally determine the Fresnel coefficient of drag of light which was first derived by Fresnel (1818), and to thereby show the necessity of including a dispersive term in the coefficient as predicted theoretically by Lorentz (1895). It was desirable that the drag coefficient be measured in a gas, solid, and various liquids. Theoretically, the contribution of the dispersive term to the drag coefficient for typical gases was shown to be less than 0.2%. Since the drag coefficient itself is less than 10^{-3} in typical gases, the dispersion term was indistinguishable in the proposed experiments. The problem was, therefore, reduced to determining accurately the coefficient of drag in a solid, and, hopefully, in various liquids and to compare the experimental coefficient with the coefficient arrived at theoretically. A further goal of this study was to show that the necessary measurements can be made with sufficient accuracy by utilizing a ring laser and to check the value so obtained as it could differ from the value obtained in a linear arrangement (Post, 1967).

This problem is of interest because the drag coefficient has never been determined to great accuracy and such a determination would lend strong support to relativity theories as well as to better define the total nature of the light dragging phenomenon (Post, 1967).

I.1. Historical Background

Experimenters in the early 19th century found that the velocity of electromagnetic propagation in a medium which was in motion relative to the observer was not the velocity expected from a direct algebraic addition of the velocities of electromagnetic propagation and of the medium. However, it was found that the electromagnetic radiation was "dragged" along with a co-moving medium. The change in velocity due to this dragging effect is proportional to the velocity of the moving medium, and the coefficient of proportionality is the drag coefficient α (i.e. α = true drag coefficient). Subsequently, Fresnel (1818) proposed that this dragging effect could be described using a drag coefficient (hereinafter referred to as α_1, i.e. α_1 = the Fresnel drag coefficient) which was dependent only upon the index of refraction of the medium n and the relative velocity of the medium v_a. Fizeau (1851), beginning in 1851, performed a classic experiment to substantiate Fresnel's equation by measuring the fringe shift of light in an interferometer when the light was propogated both with and against a moving column of water. The results obtained by Fizeau (1859) substantiated the basic form of Fresnel's equation, but were not enough to verify the drag coefficient precisely. Michelson and Morley (1886) repeated Fizeau's experiment in 1886 using a more accurate experimental arrangement. However, their errors precluded any close verification of Fresnel's drag coefficient.

In the 1890's, Lorentz (1895) derived an equation for the velocity of propagation of electromagnetic radiation through a moving medium. This derivation took into account the necessity of referring the index

of refraction back to a stationary reference frame and predicted that another term needed to be added to Fresnel's drag coefficient α_1. This term depended upon the wavelength of the radiation and the dispersion $\frac{dn}{d\lambda}$ as well as the index of refraction and velocity of the medium and resulted in a modification of α_1. Hence, the Lorentz modified drag coefficient will be referred to as α_2, i.e. α_2 = the Lorentz drag coefficient. From 1914 to 1925, Zeeman (1914) conducted a number of experiments to verify Lorentz's drag coefficient. Using a flow of water in one arm of an interferometer, and by using several different wavelengths of light, Zeeman was able to verify the necessity of the dispersive term (dispersive term = $\alpha_2 - \alpha_1 = -\frac{\lambda}{n}\frac{dn}{d\lambda}$) in Lorentz's drag coefficient and to verify its magnitude to within about 10% at short wavelengths. The percentage error in his experiments increased with wavelength and was about 20% at 6000 Å. No further attempts to verify Fresnel's drag coefficient or Lorentz's modification to it appear in the literature since Zeeman's work.

All of the aforementioned experiments relied upon interference fringe patterns produced in conventional interferometers. With the advent of the laser (Maiman, 1960), a new approach to verifying Fresnel's drag coefficient became possible. Insertion of the moving medium directly into a ring laser (Rosenthal, 1962) could yield a direct measurement of the magnitude of the dragging effect. The application of this method was first reported by Macek et al (1964) who showed that gases, liquids, and solids could be used in a ring laser to produce a beat frequency between the contracirculating beams due to the light dragging phenomenon. The method has also been used more recently by Fenster et al (1968) to measure gas flow profiles.

I.2. Experimental Method

To improve the precision with which the drag coefficient could be determined over previous measurements, a scheme was devised for utilizing a laser following a crude experiment by Macek et al (1964). The moving medium is inserted into the oscillating path of a (closed-loop) ring laser in such a manner that there is a precisely measurable component of velocity of the medium parallel with and intercepted by the laser beam. The "dragging" of the light by the moving medium then produced a difference in the absolute frequencies of the two contracirculating beams of the ring laser. This difference frequency can be determined quite precisely by optically mixing the contracirculating beams on a photodetecting device and then electronically processing the resultant difference frequency.

For initial alignment of the optical and electronic components associated with determining the difference frequency, a flow of dry nitrogen gas was introduced into the optical path of the ring laser in a specially designed flow tube with sufficient velocity to provide a separation of frequencies between the contracirculating beams. The nitrogen gas flow also provided both a gross check on the coefficient of drag for gases and verification of system capabilities of measuring the small difference frequencies due to the effect of the earth's diurnal rotation.

The drag coefficient in a solid was determined by mounting an optical quality thick disc of fused silica in a rotatable device and inserting the assembly in the optic path of the ring laser in such a manner as to be able to obtain a precisely measurable component of

velocity of the fused silica parallel with the laser beam. To reduce surface losses to a minimum, the disc was inserted at its Brewster angle.

Experiments were then undertaken to determine the stability and repeatability of velocity measurements on the medium and to determine the quality and limitations of the difference frequency monitoring system. Data was obtained relating the difference frequency to the velocity of the medium by first utilizing constant radius and variable rotation rates to determine the velocity of the medium and then, secondly, utilizing constant rotation rates and variable radii to describe the velocity.

The liquids were studied by fabricating a cell to contain the liquid. The cell was inserted in the ring laser by substituting it in place of the fused silica disc. Liquids were then chosen for analysis on the basis of their being optically transparent (clear) and having an index of refraction very nearly matching that of the fused silica windows used on the cell. No data was obtained with the liquids, however, because the ring laser would not oscillate due to scattering and depolarization losses in the liquids. A gross check of the magnitude of the scattering losses was determined experimentally.

I.3. Results Obtained

The data obtained for the nitrogen gas flow and the rotating fused silica disc were analyzed statistically. The magnitude of the bias beat frequency b due to the earth's diurnal rotation was determined for each data curve, as was the standard error Δb. In nearly every case, the limits of the experimental bias determination of $(b \pm \Delta b)_{exp}$

included the true value of b = 43 Hz. A typical value of Δb was 25 Hz. The best data was obtained with nitrogen gas flows, where b_{exp} was typically 50 Hz ± 10 Hz. A statistical determination of the magnitude of the bias resulting from the earth's rotation as seen in the fused silica data gave b_{exp} = 33 Hz ± 21 Hz which includes the true value as well.

Of more importance in this study was the determination of the drag coefficient α and its comparison with the theoretical drag coefficient including dispersion α_2. In all cases, the data was closer to the theoretical model that contained the dispersive term. The data obtained was such that α_1 was not included in $(\alpha \pm \Delta\alpha)_{exp}$, but α_2 was contained within $(\alpha \pm \Delta\alpha)_{exp}$. For the seven separate data curves obtained, the data gave

$$- 0.012 < \frac{\alpha_{exp} - \alpha_2}{\alpha_2} < + 0.002 \qquad (1\text{-}1)$$

and for the average of the seven data curves

$$\overline{\frac{\alpha_{exp} - \alpha_2}{\alpha_2}} = - 0.003 \pm 0.005. \qquad (1\text{-}2)$$

The error in α expressed as a percentage of the dispersive term alone was 13% for the average value of α. Suggestions are also given which are anticipated to lead to an improvement in the accuracy of the measurements performed here by a factor of ten or more.

CHAPTER II

THEORETICAL TREATMENT

II.1. Fresnel's Drag Coefficient

Early in the 19th century, observers noted that the velocity of light c traveling through a moving transparent medium was neither undisturbed (i.e. did not remain c) nor was it the algebraic sum of the two velocities (Galilean velocity). Fresnel (1818) showed that light, while traversing a moving medium, should have a velocity change Δv of

$$\Delta v = (1 - \frac{1}{n^2})\ v_a = \alpha_1\ v_a \qquad (2\text{-}1)$$

where v_a = velocity of the moving medium

n = index of refraction of the medium

$\alpha_1 = 1 - \frac{1}{n^2}$ = Fresnel's drag coefficient.

Thus, the velocity of light is increased if the two velocities are in the same direction, and decreased if the velocities are in opposite directions. The Fresnel representation of this phenomenon then gives the velocity of light in the medium as being

$$v = \frac{c}{n} \pm (1 - \frac{1}{n^2})\ v_a \qquad (2\text{-}2)$$

where c is the free space velocity of light and v_a is positive or negative depending upon whether it is in the same direction as c or

opposed to c (Rosser, 1964). The classic velocity of light in a medium with index of refraction n is defined by (for the medium at rest)

$$w = \frac{c}{n} \tag{2-3}$$

where w is the phase velocity of light.

Eq. (2-2) may be derived in the following way utilizing the one-dimensional Lorentz transformation equations

$$x^* = \frac{x - v\,t}{\sqrt{1 - \frac{v^2}{c^2}}} \tag{2-4a}$$

$$t^* = \frac{t - \frac{v\,x}{c^2}}{\sqrt{1 - \frac{v^2}{c^2}}} \tag{2-4b}$$

where the unstarred coordinates are for a stationary observer (reference frame) and the starred coordinates are for the moving frame. Displacement in a substance with the velocity of light being $\frac{c}{n}$ in the moving frame is given by

$$x^* = \frac{c}{n} \left(t^* - t_o^* \right) \tag{2-5}$$

relative to the moving frame. Applying Eqs. (2-4) to Eq. (2-5) gives

$$x - v_a\,t = \frac{c}{n} \left[\left(t - \frac{v_a\,x}{c^2}\right) - t_o^* \sqrt{1 - \frac{v_a^2}{c^2}} \right]. \tag{2-6}$$

If Eq. (2-6) is put in the form $x = v\,t$ + constant, then v is given by

$$v = \frac{c}{n} + \frac{\left[1 - \frac{1}{n^2}\right]}{\left[1 + \frac{v_a}{n\,c}\right]}\, v_a. \tag{2-7}$$

Let the second term in the right hand side of Eq. (2-7) be referred to as $f(v_a + h)$. Then expanding the second term in the right hand side of Eq. (2-7) in a series expansion with v_a as variable and retaining only terms up to $f^1(v_a)$ (i.e. assuming $v_a << c$), results in Eq. (2-7) being written as

$$v = \frac{c}{n} + (1 - \frac{1}{n^2})\, v_a. \tag{2-8}$$

This is the velocity of propogation when c and v_a are in the same direction. Eq. (2-8) is the same as the result obtained by Fresnel (1818) as given in Eq. (2-2) even though Fresnel based his derivation on an incorrect model (Rosser, 1964).

It is also interesting to note that if the substitution $w = \frac{c}{n}$ is made in Eq. (2-7), then the equation can be rearranged to give Einstein's velocity addition equation

$$v = \frac{w + v_a}{1 + \frac{w\, v_a}{c^2}}. \tag{2-9}$$

In fact, Laue (1907) was the first to note that Eq. (2-9) could be used to explain Eq. (2-2) purely phenomenologically without making any special assumption regarding the nature of the propogation of light in the moving medium (Sommerfeld, 1954).

II.2. Dispersive Term in the Drag Coefficient

In the preceeding equations, the value of the index of refraction has been assumed to be identical in all non-accelerated reference frames. However, the index of refraction is dependent on the wavelength of light, i.e. $n = n(\lambda)$. In particular, the wavelength of a spectral line emitted

from a reference frame is seen in the moving frame as being modified to $\lambda' = \lambda + \Delta\lambda$ (Sommerfeld, 1954). One obtains, therefore,

$$n(\lambda') = n(\lambda + \Delta\lambda) = n + \frac{dn}{d\lambda}\,\Delta\lambda \ . \tag{2-10}$$

The change in wavelength $\Delta\lambda$ is found from the first order approximation to the exact Doppler effect equation for free space which is the well-known elementary expression

$$\frac{\Delta\lambda}{\lambda} = \frac{v}{c} \tag{2-11}$$

for a light source of velocity v whose propogation velocity is c. The change in wavelength $\Delta\lambda$ is found from Eq. (2-11) by replacing c by the velocity of propogation $\frac{c}{n}$ in a medium whose index of refraction is n. Hence, Eq. (2-10) can be written

$$n(\lambda') = n + \lambda \frac{dn}{d\lambda} \frac{n\ v}{c} \ . \tag{2-12}$$

If one now rewrites Eq. (2-7) for $n(\lambda')$, the result is

$$v = \frac{c}{n(\lambda')} + \frac{\left[1 - \dfrac{1}{n(\lambda')^2}\right]}{\left[1 + \dfrac{v_a}{cn(\lambda')}\right]}\ v_a \tag{2-13}$$

which by Eq. (2-12) becomes

$$v = \frac{c}{\left(n + \lambda \dfrac{dn}{d\lambda} \dfrac{nv_a}{c}\right)} + \frac{\left[1 - \dfrac{1}{\left(n + \lambda \dfrac{dn}{d\lambda} \dfrac{n\ v_a}{c}\right.}\right]}{\left[1 + \dfrac{v_a}{nc + \lambda \dfrac{dn}{d\lambda}\, n\ v_a}\right]} v_a . \tag{2-14}$$

Expanding the right hand side of Eq. (2-14) in a series expansion with v_a as variable and again retaining terms only up to v_a^1 (i.e. assuming

$v_a << c$) results in

$$v = \frac{c}{n} + \left(1 - \frac{1}{n^2} - \frac{\lambda}{n}\frac{dn}{d\lambda} \right) v_a \ . \qquad (2\text{-}15)$$

Eq. (2-15) is the expression derived by Lorentz (1895) that includes the effects of dispersion. The drag coefficient included in Eq. (2-15) is the Lorentz modified drag coefficient which is referred to as α_2, i.e.

$$\alpha_2 = 1 - \frac{1}{n^2} - \frac{\lambda}{n}\frac{dn}{d\lambda} \ . \qquad (2\text{-}16)$$

The difference $\alpha_2 - \alpha_1$ is the dispersive term $- \frac{\lambda}{n}\frac{dn}{d\lambda}$. Since the dispersion $\frac{dn}{d\lambda}$ typically obeys $\frac{dn}{d\lambda} < 0$ and λ and n are always positive, it follows that typically $\alpha_2 > \alpha_1$.

II.3. Equations of the Ring Laser

II.3.1. General Description of a Ring Laser

A ring laser is simply a light oscillator arranged so that the oscillating beam (or beams) encloses an area. The ring laser was first proposed by Rosenthal (1962). In the simplest case, a ring laser is achieved by arranging three mirrors in any arbitrary triangular geometry such that they serve to produce a positive feedback path for the light amplifying medium which is contained in the internal laser path. One unique property of the ring laser is that the closed-loop path allows for the generation and propogation of two separate oscillating beams. The energy of one beam is propogated clockwise, while the energy of the other is propogated counterclockwise. Under most conditions the frequencies of the beams are independent of each other and are determined by the condition that the wavelength of each must be an

exact integer fraction of its optical path around the ring (Killpatrick, 1967).

II.3.2. Modes in a Ring Laser

The necessary criterion for oscillation in a ring laser is that a wave must change its phase by an integral multiple of 2π in traversing the closed loop (Macek et al, 1963). This necessitates the cavity path length L being an integral number N of wavelengths, i.e.

$$L = N \lambda \, . \tag{2-17}$$

Using the relation $\lambda \nu = c/n$ allows one to write Eq. (2-17) as

$$L = \frac{N c}{n \nu} \tag{2-18}$$

which is easily arranged to

$$\nu = \frac{N c}{n L} \, . \tag{2-19}$$

Noting that for air $n \approx 1.00$ allows one to write for $\Delta N = 1$

$$\Delta\nu = \frac{(N + 1) c}{L} - \frac{N c}{L} \tag{2-20}$$

so that

$$\Delta\nu_{axial} = \frac{c}{L} \tag{2-21}$$

for $\Delta N = 1$. The term $\Delta\nu_{axial}$ defined by Eq. (2-21) is the frequency separation of axial modes in a ring laser whose absolute frequency is determined by the appropriate value of N ($\approx 10^6$ per meter) in Eq. (2-19) such that ν lies within a sufficiently high gain region of the Doppler broadened line profile of the lasing medium so that oscillation

of the laser occurs (Bagaev et al, 1966).

A cavity path length change ΔL (real or effective) will cause a wavelength change of (assuming a given axial mode with N nodes)

$$\Delta\lambda = \frac{\Delta L}{N} . \tag{2-22}$$

The corresponding frequency change is found by differentiating Eq. (2-19) with respect to ν and L, whence

$$\frac{\Delta\nu}{\nu} = -\frac{\Delta L}{L} . \tag{2-23}$$

Two phenomena of interest which cause an effective ΔL are rotation of the ring laser relative to inertial space and introduction of a moving medium into the oscillating cavity.

II.3.3. Effects Due to Rotating a Ring Laser

Rotation of the ring laser in inertial space results in a ΔL that is predicted by general relativity theory. Two observers (say photons), traveling around a closed path that is rotating in inertial space, will observe a time difference when they return to the starting point after traveling around the same path but in opposite directions. The observer traveling in the direction of rotation will experience a small increase in clock time, and the observer traveling in the opposite direction will experience a corresponding small decrease. Killpatrick (1967) gives the time difference Δt as depending upon the inertial rotation rate Ω, the area A enclosed by the path, and the speed of light c as

$$\Delta t = \frac{\Omega}{c^2} 2A + \frac{\Omega}{c^2} 2A = \frac{4 A \Omega}{c^2} . \tag{2-24}$$

For photons traveling around the rotating path, the time difference

Δt appears as an apparent length change ΔL of the cavity as

$$\Delta L = c\,\Delta t \tag{2-25}$$

so that

$$\Delta L = \frac{4\,A\,\Omega}{c}\,. \tag{2-26}$$

Combining Eq. (2-23) and Eq. (2-26) and recalling $\lambda\nu = c$ for $n \approx 1.00$, one obtains

$$\Delta\nu = \frac{4\,A\,\Omega}{\lambda\,L}\,. \tag{2-27}$$

II.3.4. Moving Medium in a Ring Laser

The ideas presented in the following discussion were first discussed by Rosenthal (1962) and subsequently refined by Macek et al (1964). For the ring laser, the velocity of light traveling through a moving medium within the laser cavity is given by Eq. (2-15). As mentioned in Section II.3.2., a consequence of satisfying the conditions for oscillation in a ring laser is that the cavity path length must equal an integral number of wavelengths; namely,

$$N\,\lambda = [\,L - L_r\,]\,n(\text{eff}) + L_r\,n(\lambda') \tag{2-28}$$

where L = optic path length of the oscillator cavity

L_r = optic path length through a moving sample

$n(\text{eff})$ = effective index of refraction of the cavity path which does not contain the sample

$n(\lambda')$ = apparent index of refraction of the moving sample as measured in a stationary frame.

The apparent index of refraction $n(\lambda')$ can be written as

$$n(\lambda') = n(\lambda) \pm \Delta n \tag{2-29}$$

where $n(\lambda')$ is due to the motion of the medium and can be found conveniently by using Eq. (2-3), Eq. (2-15), and Eq. (2-16) to write equations for the indices of refraction as seen in both the direction of motion and the direction opposite to the motion of the medium, whence

$$n(\text{same}) = \frac{c}{\frac{c}{n} + \alpha_2 v_a} \approx n\left(1 - \frac{n v_a \alpha_2}{c}\right) \tag{2-30}$$

$$n(\text{opposed}) = \frac{c}{\frac{c}{n} - \alpha_2 v_a} \approx n\left(1 + \frac{n v_a \alpha_2}{c}\right) \tag{2-31}$$

so that for $v_a << c$ one obtains $2\,\Delta n = n(\text{opposed}) - n(\text{same})$ as

$$2\,\Delta n = \frac{2\,\alpha_2 v_a n^2}{c}\,. \tag{2-32}$$

Then Eq. (2-29) can be written

$$n(\lambda') = n \pm \frac{\alpha_2 v_a n^2}{c} \tag{2-33}$$

so that Eq. (2-28) becomes

$$N\lambda = L\,n(\text{eff}) + L_r[n - n(\text{eff})] \pm L_r\frac{\alpha_2 v_a n^2}{c}. \tag{2-34}$$

The first and second terms on the right hand side of Eq. (2-34) are seen to account for the length of the optic path around the cavity for the stationary ring, and the third term describes the path length changes $\pm\,\Delta L/2$ due to motion of the medium, so that the total length change due to motion is

$$\Delta L = \frac{2 L_r \alpha_2 n^2 v_a}{C}\,. \tag{2-35}$$

The frequency separation of the contracirculating beams in the ring laser is found by substituting for ΔL from Eq. (2-35) into Eq. (2-23) and utilizing the relation $\lambda \nu = c/n(air)$ where $n(air) \approx 1.00$, whence

$$\Delta\nu = - \frac{2 L_r \alpha_2 n^2 v_a}{L \lambda} . \qquad (2\text{-}36)$$

It is now desirable to write Eq. (2-36) in terms of the parameters which were measured in the experimental case of the solid medium which was inclined to the beam at its Brewster angle and then rotated (see Figure 11 and Figure 12). Hence, the length of sample L_r becomes (see Figure 12) [for Brewster's angle, $\theta_t + \theta_B = 90°$ (Born and Wolf, 1965)]

$$L_r = \frac{d}{\cos \theta_t} = \frac{d}{\sin \theta_B} . \qquad (2\text{-}37)$$

The velocity v_a of the medium in the direction of the beam is obtained by taking the projection of the tangential velocity v_t along the beam. Since the tangential velocity is given by

$$v_t = \omega R \qquad (2\text{-}38)$$

and the projection of v_t along the beam is $v_t \cos(90-\theta_t)$ (see Figure 12), the velocity v_a of the medium which is projected along the beam is given by

$$v_a = \omega R \cos (90-\theta_t) \qquad (2\text{-}39)$$

which, by virtue of the relationship between θ_B and θ_t for incidence at the Brewster angle, becomes

$$v_a = \omega R \cos \theta_B . \qquad (2\text{-}40)$$

The use of Eq. (2-21), Eq. (2-37), and Eq. (2-40) allows Eq. (2-36) to

be written for the ideal case of $\tan \theta_B = n$ as

$$\Delta\nu = \frac{2\, d\, n\, \omega\, R\, \alpha_2\, \Delta\nu_{axial}}{c\, \lambda} \quad . \tag{2-41}$$

The negative sign from Eq. (2-36) does not appear in Eq. (2-41) because the relationship between $\Delta\nu$ and ω allows an arbitrary choice of signs (see Section II.3.5.). In terms of the units actually measured and recorded for each parameter (see Table VII), Eq. (2-41) becomes (note that $\omega = 2\, \pi\, f_\omega$)

$$\Delta\nu = 5.320 \times 10^{10}\ \frac{d\, n\, f_\omega\, R\, \alpha_2\, \Delta\nu_{axial}}{c\, \lambda} \tag{2-41a}$$

where the following units were used:

$\Delta\nu$ - kHz

d - inch

f_ω - RPM

R - cm

$\Delta\nu_{axial}$ - MHz

c - cm/sec

λ - Å

α_2 - dimensionless.

The total beat frequency observed Δf_B will be the algebraic sum of the effects predicted by Eq. (2-27) and Eq. (2-41), i.e.

$$\Delta f_B = \frac{2\, d\, n\, \omega\, R\, \alpha_2\, \Delta\nu_{axial}}{c\ \ \lambda} \pm \frac{4\, A\, \Omega}{\lambda\, L} \tag{2-42}$$

where the sign of the second term must be taken to agree with the arbitrarily determined sign of the first term (see Section II.3.5.).

II.3.5. Effects of Direction of Motion Relative to the Ring Laser

At this point, it is very important to note the effects of the direction (sense) of inertial rotation and medium motion on the frequency shift of each of the contracirculating beams. For rotation in inertial space in a counterclockwise (ccw) direction, the frequency of the ccw beam is decreased and the frequency of the clockwise (cw) beam is increased. These conditions apply to any ring laser operated in the Northern Hemisphere when the propogation directions are determined by looking into the ring along a line from north to south which is parallel to the polar axis. The effect of a medium moving in a cw direction in the ring is to increase the cw beam frequency and to decrease the ccw beam frequency. Therefore, when the medium is in motion in a cw direction, the two effects will add directly. In displaying the results of this work, Δf_B was arbitrarily chosen to be

$$\Delta f_B = \nu_{cw} - \nu_{ccw} \tag{2-43}$$

so that the positive sign in Eq. (2-42) is specified. One then expects an increased value for Δf_B for cw motions of the medium and a decreased value for Δf_B for ccw motions.

II.3.6. Evaluation of the Drag Coefficient

To determine α, it is necessary to employ a statistical analysis of the data. A meaningful representation is obtained if one notes that $\Delta\nu$ in Eq. (2-27) is a constant for the earth's rotation and one then differentiates Eq. (2-42) implicitly with respect to f_ω (recall that $\omega = 2\ \pi f_\omega$) to obtain

$$\frac{d(\Delta f_B)}{df_\omega} = \frac{4\ \pi\ d\ n\ R\ \alpha_2\ \Delta\nu_{axial}}{c\ \lambda} \tag{2-44}$$

which can easily be rearranged to

$$\alpha_2 = \frac{c\ \lambda}{4\ \pi\ d\ n\ R\ \Delta\nu_{axial}}\ \frac{d(\Delta f_B)}{df_\omega}\ . \tag{2-45}$$

The slope of the linear least squares fit to the data obtained for the rotated solid disc which was inclined to the beam will be

$$m = \frac{d(\Delta f_B)}{dv_a}\ . \tag{2-46}$$

To write Eq. (2-46) as a function of df_ω rather than as a function of dv_a it is necessary to differentiate Eq. (2-40) implicitly, again recalling that $\omega = 2\ \pi\ f_\omega$, whence

$$dv_a = 2\ \pi\ R\ \cos\ \theta_B\ df_\omega \tag{2-47}$$

for f_ω in rev/sec. The use of Eq. (2-47) allows one to write Eq. (2-46) as

$$m = \frac{1}{2\ \pi\ R\ \cos\ \theta_B}\ \frac{d(\Delta f_B)}{df_\omega} \tag{2-48}$$

so that Eq. (2-45) becomes

$$\alpha_2 = \frac{c\ \lambda\ m\ \cos\ \theta_B}{2\ d\ n\ \Delta\nu_{axial}}\ . \tag{2-49}$$

For the units in which the parameters were measured and utilizing from $\tan\ \theta_B = n = 1.4571$ (see Table VII), Eq. (2-49) was used for direct calculations in the form

$$\alpha_2 = \frac{1.969 \times 10^{-15}\ c\ \lambda\ \cos\ \theta_B\ m}{d\ n\ \Delta\nu_{axial}} \tag{2-49a}$$

where c - cm sec^{-1}

d - inch

m - cm^{-1}

λ - Å

α_2, n - dimensionless

$\Delta\nu_{axial}$ - MHz.

Using the values of the parameters n, λ, and c as listed in Table VII and the values for d and $\Delta\nu_{axial}$ as determined and listed in Chapter V (note that θ_B is determined from n as $\tan\theta_B = n$) allows Eq. (2-49a) to be written, for the system used to obtain the data presented here, as

$$\alpha_2 = 3.133 \times 10^{-3}\, m \qquad (2\text{-}49b)$$

where m is defined by Eq. (2-46) in units of Hz sec cm^{-1}, or, substituting Eq. (2-48) into Eq. (2-49a), as

$$\alpha_2 = \frac{5.287 \times 10^{-2}}{R} \frac{d(\Delta f_B)}{df_\omega} \qquad (2\text{-}49c)$$

where the appropriate units are:

Δf_B - Hz

f_ω - rev/min (RPM)

R - cm.

II.3.7. Ultimate Accuracy Attainable With the Ring Laser

To properly evaluate the possible improvements which can be made to the system, it is necessary to have a reasonable idea of the ultimate accuracy attainable utilizing the ring laser in the manner presented here. If α_2 is determined from Eq. (2-49a), then the accuracy with which α_2 can be determined will depend upon the accuracy with

which d, n, θ_B, $\Delta\nu_{axial}$, and m can be measured since c and λ are readily known to sufficient accuracy so as to not limit the determination (see Table VII). Measurement of d to $\lambda/4$ is quite readily possible and n can be determined to an accuracy of better than one part per million, so these two parameters can, if necessary, be measured with very good precision. The angle θ_B, the angle at which the normal to the surface of the medium is inclined to the beam, can also be determined to a high degree of accuracy by employing triangulation of reflected circularly polarized light. Experience suggests a practical angular determination to be 15 arc seconds (0.004 degree). The axial frequency separation $\Delta\nu_{axial}$ can certainly be determined to an accuracy of one part per hundred thousand (see Appendix B).

The term m is the slope of a plot of Δf_B vs. v_a, and hence, its accuracy depends directly on the precision with which Δf_B and v_a are specified. It is reasonable to conclude that the bandwidth of the two contracirculating oscillators, when operated in the single-valued q TEM_{ooq} mode, is less than 1 Hz (Javan et al, 1962), so that the beat frequency Δf_B between the two oscillators should be detectable to at least 1 Hz precision.

The limiting factor in the system used here is the spread in the velocity component of the medium along the beam. By an elementary exercise with vectors, it is easy to show that the velocity component v_a of the medium along the beam is constant everywhere through the medium in the case of a ray which intersects a rotating cylinder at an angle to the axis of rotation (see Appendix D). The velocity v_a in this case is specified by Eq. (2-40). However, since the beam has a finite cross-section, the radius R in Eq. (2-40) is not constant at a single

value, but varies from R by as much as one-half the beam diameter. Now it is necessary to specify a radius R for each photon, or stated another way, the distribution of radii used must be the same as the energy distribution in the beam cross-section. The energy distribution in the beam cross-section is Gaussian (Boyd et al, 1961). The net result is a broadening of the range of frequencies Δf_B detected. The spread of Δf_B can easily be approximated by the ratio

$$\frac{\Delta(\Delta f_B)}{\Delta f_B} \approx \frac{\Delta R}{R} \qquad (2\text{-}50)$$

where $\Delta(\Delta f_B)$ is the total frequency variation in beat frequencies for a variation in R of ΔR. Of course, ΔR is determined by the diameter of the beam cross-section. For a beam diameter of 0.1 mm and a radius of 1 cm, the ratio $\Delta R/R$ would be 1/100, so that $\Delta(\Delta f_B)$ would be a 1% spread of frequencies about Δf_B.

However, this frequency spread, which occurs due to velocity variations across the beam cross-section, can be greatly reduced if an optic mixer is used such that the frequencies corresponding to the lower velocity (i.e. smallest R) in one beam are mixed with the frequencies corresponding to the higher velocity (i.e. largest R) in the other beam. Since the actual frequency shifts in ν (recall that ν is proportional to v_a) vary linearly with the radius R, this procedure theoretically would produce an identical beat frequency Δf_B from all portions of the beam cross-section. Such a mixer is conveniently realized in the fashion described subsequently in Chapter III. In practice, a small frequency spread is to be expected (of less than a few Hz) due to imperfect alignment of the optic mixer and incomplete frequency compensation due to imperfect energy distributions in the beam across its

cross-section.

Using the optical mixing technique mentioned above, one should be able to develop this system to have beat frequency detection capabilities of 1 Hz or better through the use of sophisticated techniques to overcome both normal problems (vibration, air motion, etc.) and the special problems mentioned above. Hence, it would be desirable to be able to measure each parameter to at least one part in 10^5 or even 10^6. Ultimately, for a limiting parameter measurement of Δf_B with a value of 1 Hz, the accuracy of the system described here could determine α with an accuracy of one part in 10^5.

CHAPTER III

EXPERIMENTAL APPARATUS

III.1. Description of the Equipment

The performance of the experiments that were necessary for this work required considerable electronic and mechanical equipment. The design, construction details, operation, and characteristics of this equipment will be given in this chapter. A block diagram of the measuring system which utilized the ring laser is shown in Figure 1. The triangular sketch represents the beam path (oscillator feedback) in the ring laser. The description of this equipment will be given by sub-systems. These are the ring laser drag sensor, the beam combiner, the optical detector, the beat frequency signal processing section, the moving medium, data accumulation equipment, and peripheral equipment.

III.1.1. Ring Laser Drag Sensor

The purpose of the ring laser in these experiments was to provide a measure of the effect of the "dragging" of light in moving media, so the ring laser was designed to achieve this goal by utilizing the parts that were available and parts which could be obtained economically. Factors which were considered in the design of the ring laser were wavelength, ring geometry, minimum system losses, small beam waist at the moving medium, adequate power coupled out for signal detection, funda-

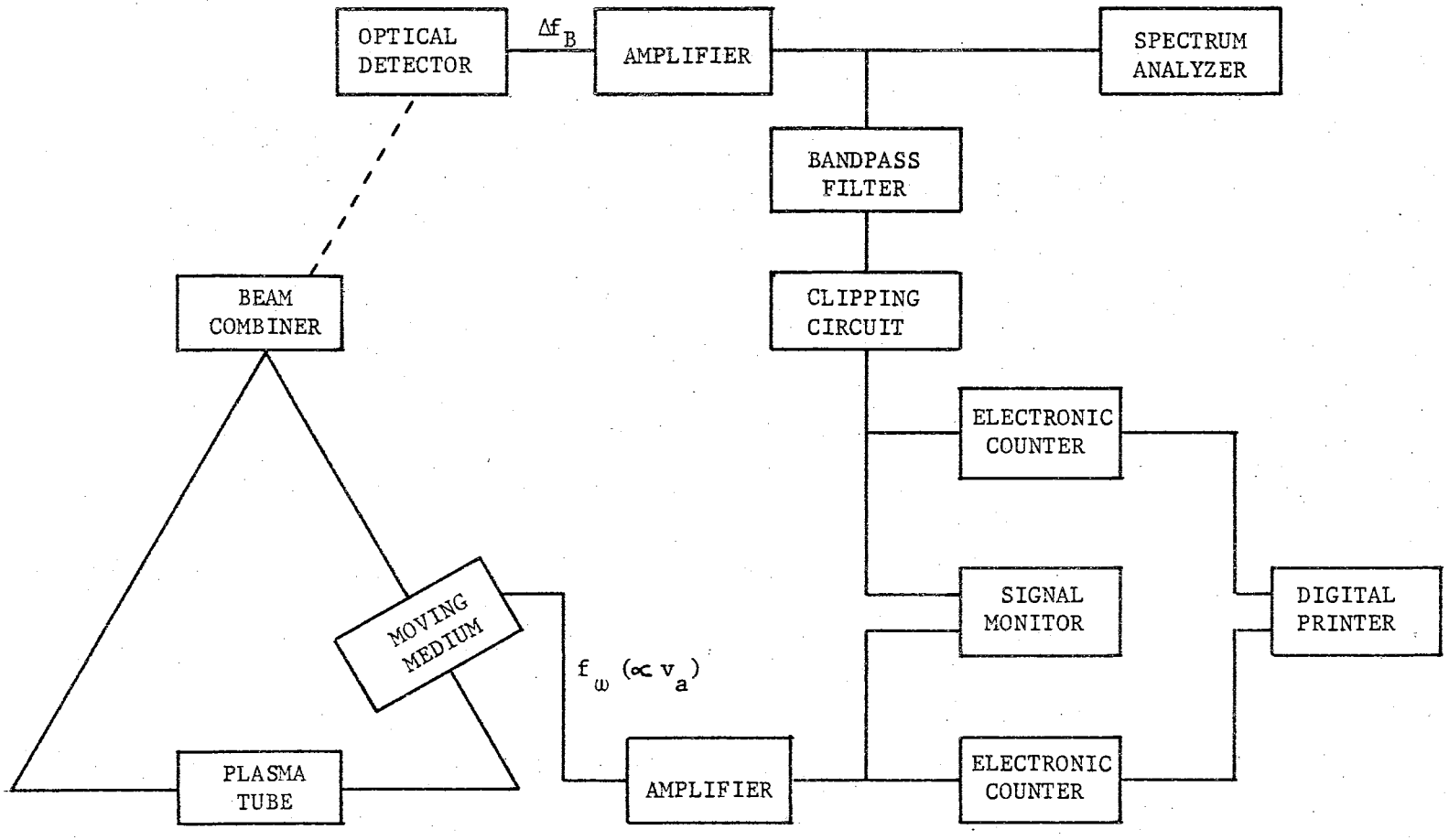

Figure 1. Block Diagram of the Equipment for Taking Measurements of Beat Frequency vs. Velocity (or Frequency of Rotation)

mental transverse mode operation, vibration free environment, and a clean atmosphere.

The wavelength of operation, chosen to be the visible transition of the He-Ne laser at 6328 Å, was selected primarily because of the availability of mirror reflectors at 6328 Å and due to the ease of alignment by using visual techniques. The ring laser used is shown in Figure 2. The "ring" geometry was chosen to be an equilateral triangle with sides of approximately one meter. Mirror alignment in a triangle is simplified over that of a rectangle as the alignment in the plane of the ring is self-compensating for an odd number of mirrors, and only the alignment in a plane perpendicular to the plane of the ring introduces any difficulties. An equilateral triangle was chosen to provide beam symmetries in each arm. The size of the ring was a tradeoff between increased sensitivity with increased area or decreased fluctuations with decreased path length (Killpatrick, 1967). The axial mode separation frequency also increases with decreasing path length. The shorter path length was seen to be the more important parameter, and, hence, the length of each side was chosen to be slightly greater than the one meter plasma tube length.

The plasma tube used in the ring laser was a one meter, 4 mm bore tube with Brewster angle windows. It was filled with a He-Ne gas mixture and supplied by PEK Labs. This plasma tube was about four years old and prior to this work was found to be inoperative. Rejuvenation by putting the tube in a (natural occurrence) helium atmosphere for about one hour gave the tube new life and yielded an optimum power output of three milliwatts. The tube has no internal electrodes and, hence, is RF excited by a series of seven copper strips wrapped about the bore of the

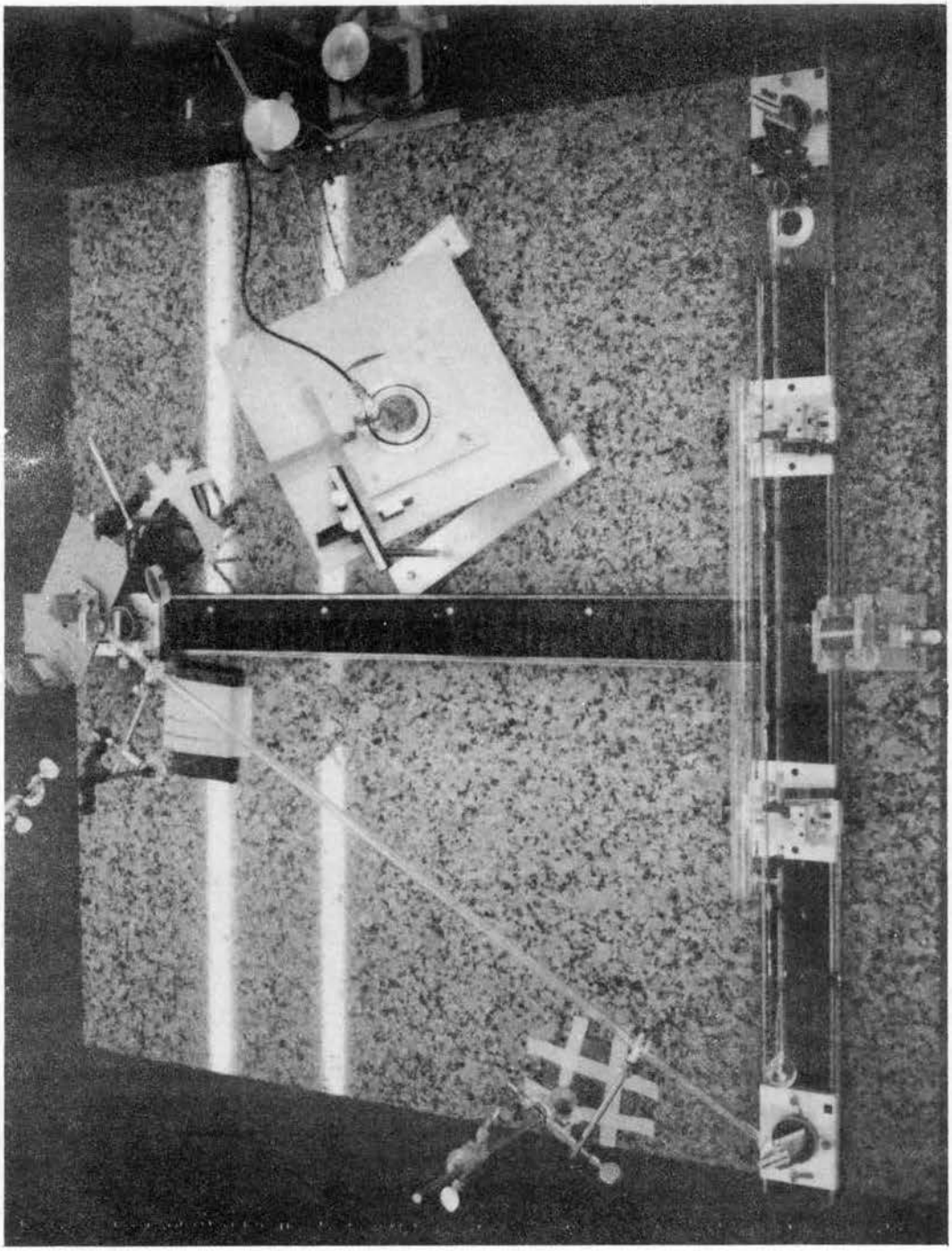

Figure 2. Ring Laser and Vibration Isolated Table Top

tube. The strips are evenly spaced so that the plasma will not contribute to any ring bias frequency (Killpatrick, 1967). RF power of approximately 50 watts is supplied by a Viking Challenger amateur radio transmitter. The RF frequency is not critical and the use of any frequency in the amateur band from 28 MHz to 29.7 MHz works satisfactorily. Correct alignment of the plasma tube in the ring laser is found while operating the ring laser as an oscillator. If the normals to the Brewster windows do not lie in either a plane normal to the plane of the ring or in a plane parallel to the plane of the ring, a significant reflection of the internal beam occurs from the Brewster windows. This reflection can be visually monitored and will be found to disappear (assuming that the windows truly are at their Brewster angle) when the plasma tube Brewster window normals are either parallel or normal to the plane of the ring. The above alignment is necessary in a ring laser due to the unique polarization states allowed in a triangular ring resonator as pointed out by Bagaev et al (1966).

Initial alignment of the ring is achieved by using two additional mirrors in the arm of the ring that contains the plasma tube, and aligning them with the plasma tube to form a linear laser. The output of this laser is reflected in both directions around the ring. Near correct alignment is obtained when the two beam cross-sections are everywhere concentric. The two additional mirrors are then removed. Fine adjustments of at least one corner mirror may be necessary to obtain oscillation of the ring.

The mirrors employed at each corner of the triangular ring were dielectric coated mirrors whose narrow-band reflectance was peaked at 6328 Å. They are made for normal incidence, but can be used at angles

of incidence up to about 40 degrees with only slight additional losses. These losses depend not only on the angle of incidence, but also on the plane of polarization of the incident light. To minimize the losses due to the mirrors, reflectances as near unity as possible were used. Nominal reflectance on all three mirrors was 99.9^{+} %. The mirror used for output coupling had a transmission of less than 0.1%, but this was quite adequate. The radius of curvature of each mirror was chosen to provide a narrow beam waist in the moving medium as well as to provide a large mode volume in the plasma tube. This was best accomplished by using identical mirrors at the corners near either end of the plasma tube and a mirror with a non-identical radius of curvature for the output corner. The mode volume in the plasma tube as well as the beam waist and its position can be calculated from the theory given by Rigrod (1965). From the high reflectance mirrors which were available, two choices were possible. These were a 3 m, 6 m, 6 m radius of curvature combination and a 1 m, 1 m, 2 m radius of curvature combination. The 3-6-6 combination had very good reflectance characteristics, was easily aligned, and offered a large mode volume, but the minimum fundamental transverse mode beam waist was quite large. On the other hand, the 1-1-2 combination had good reflectance characteristics, was also easily aligned, had only a slightly smaller mode volume in the plasma tube, and in addition, had a very narrow beam waist located symmetrically in the two arms between the 1 m and 2 m radius of curvature mirrors. Also, the output beam in fundamental mode operation is smaller through the non-identical mirror in a triangular ring laser if the output mirror's radius of curvature is larger than that of the identical mirrors. The mirrors were held in custom holders which were fabricated to allow adjustment of the mirror

independently about both the x-axis and the y-axis and which could be moved linearly along the base plates. As mentioned, operation in the fundamental transverse mode was required to reduce suprious signals. Since the unperturbed ring laser operated in a high order mode, e.g. TEM_{55q}, it was necessary to use an adjustable iris to introduce diffraction losses sufficient to obtain TEM_{ooq} mode operation. The iris was located near a position of maximum beam waist between one end of the plasma tube and the adjacent mirror as shown in Figure 2. Using an iris to introduce beam losses in the feedback path has two distinct advantages over RF power reduction to the plasma tube amplifier for obtaining TEM_{ooq} mode operation. First, the use of an iris allows the light amplifier to operate at maximum gain while the oscillation level is reduced by reducing the positive feedback. The stability of the oscillation amplitude is much better for the case of high gain and reduced feedback than it is for the case of large feedback and reduced gain because in the former case the amplitude fluctuations in the plasma tube introduce much more significant variations. Secondly, the alignment of the beam combiner is very critically dependent on the position at which the clockwise and counterclockwise beams strike the output mirror. Reduction in amplifier gain can cause random movements of the beam position as the gain is varied. Iris adjustment, on the other hand, necessarily requires the beam center to remain in one exact position. The second advantage listed above also makes the use of an iris vastly superior to mirror misalignment in reducing the amount of light feedback.

The simultaneous reduction of both the iris opening and input power to the plasma tube allows one to reduce the TEM_{ooq} mode structure from one containing several axial modes (i.e. several values of q) to one

which is restricted to a single value of q. The above constraints reduce the gain of the axial (longitudinal) modes in the Doppler broadened profile until only one mode oscillates. If the path length of the ring is reduced, then the frequency separation of the axial modes increases. This allows more power and stability to be obtained at a single frequency from a given system when operating in the single-valued q TEM_{ooq} mode because the adjacent axial modes (corresponding to $\pm \Delta q = 1$) lie in regions of reduced gain.

The ring laser and beam combiner were mounted on a vibration isolation table to reduce the effect of environmental vibrations. A 48 inch square block of granite about three inches thick and weighing 550 pounds was used as a table top for the ring laser and beam combiner. The upper surface was smoothed and polished by the supplier, Texas Granite Corp., to provide a convenient working surface. The granite slab was supported by four vibration isolation feet manufactured by Korfund Dynamics. These feet were located near the center of each quadrant of the slab, and they rested on the top of a large wooden table which was also vibration isolated. The RF transmitter was mounted on the wooden table and, together with the table, gave an additional suspended weight of 200 pounds to the isolation system. The wooden table was held off the floor by four additional vibration feet placed near each corner. The only paths for vibration transmission to the ring laser were the vibration isolation feet, the air, the RF power cable from the transmitter (which was partially vibration isolated), the belt drive for the moving medium (#50 thread), two #22 insulated wires, and a coaxial cable from the velocity detector. Each of the latter three items was suspended by rubber bands to reduce vibration transmission. The optical detector was pur-

posely located off the vibration-free table due to the vibrations that would be transmitted through its interconnecting cables. In practice, most of the table vibrations were produced by an unbalance of the moving medium at high velocities. The rotator for the moving medium was directly connected to the vibration-isolated mass. Hence, it was desirable that the rotator be very well balanced. The stability of the table top was determined by observing the fringe pattern in an unequal arm interferometer whose mirrors and beam splitter were individually set on the table top. Even in a fairly "quiet" environment, gross fringe fluctuations are present, but on the table top a stable pattern was generally apparent. The fringe pattern was upset by such things as blowing on the ring laser, tapping the table top, or by a slammed door in the building. A stable pattern usually reappeared within 10 seconds of a large vibration.

III.1.2. Beam Combiner

The clockwise and counterclockwise beams are combined external to the ring laser in the beam combiner shown in Figure 3. The operation of the beam combiner is illustrated in Figure 4. The clockwise beam emerges from the output mirror parallel to, but displaced from, the internal clockwise beam and proceeds to the beam splitter where the beam is divided. The beam splitter is manufactured from two right angle prisms whose wide faces are lightly aluminized and then joined together so the pieces form a right-angled parallelepiped. About 30% of the power goes directly through the beam splitter, 30% is diverted at right angles by the partially reflecting interface, and about 40% of the power is absorbed in the beam splitter. The counterclockwise beam emerges from the

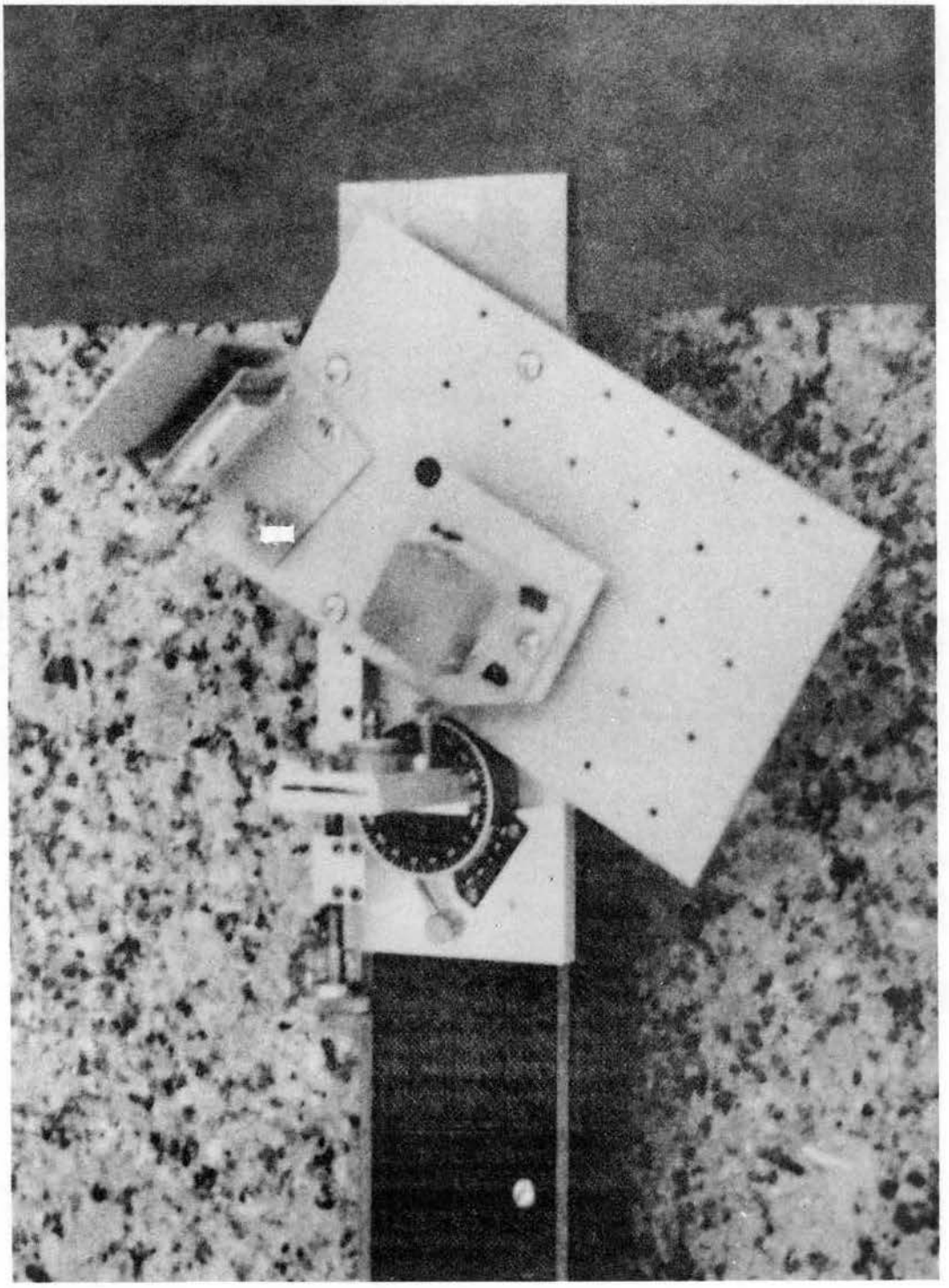

Figure 3. Beam Combiner

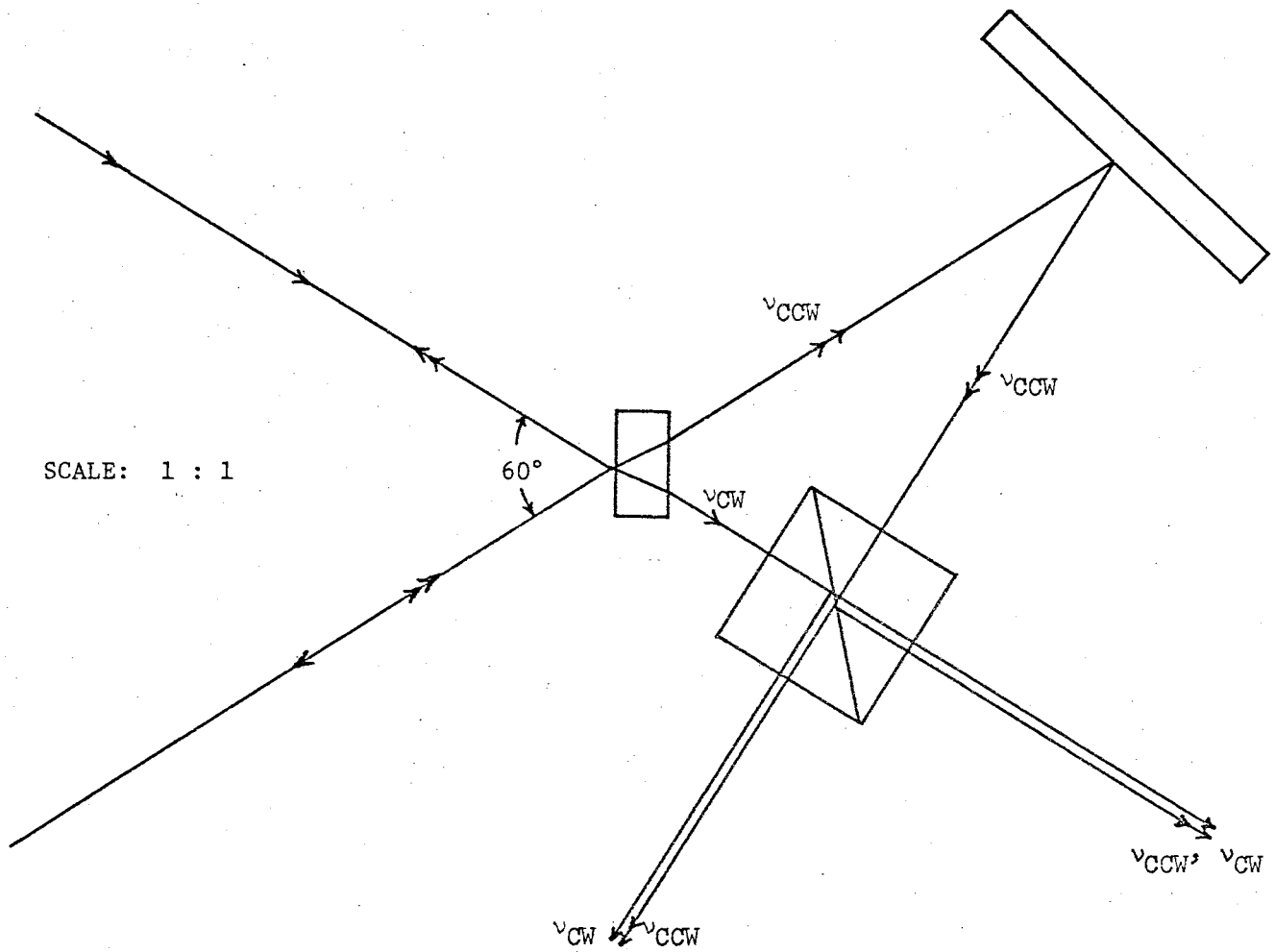

Figure 4. Schematic of the Beam Combiner

output mirror similar to the clockwise beam, but is reflected by an adjustable front surface mirror so as to enter the beam splitter at a right angle to the clockwise beam where it is divided such that it leaves the beam splitter along the same paths as the clockwise beam. In the illustration in Figure 4 the beams are shown offset and misaligned for clarity. The beat frequency detector is located in either path. Since the two beams of slightly differing frequencies are to be mixed in the detector, it is necessary for then to be both exactly overlaid and parallel at the detector for mixing to take place. In order that the counterclockwise beam can be properly directed, the front surface mirror is held in a mount which can be adjusted to independently move the reflected beam horizontally and vertically. In addition, the mount can be moved in a direction perpendicular to the reflecting surface to allow proper positioning of the counterclockwise beam on the beam splitter. In addition to the front surface mirror being adjustable, the beam splitter is mounted so that it can be aligned to be perpendicular to the clockwise beam and so it can be tilted to allow the two beams to be exactly coincident and parallel.

Proper alignment of the mirror and beam splitter can be determined by either of two methods. When the ring laser is operating in the "lock-in" region such that the frequencies of both beams are identical, coarse alignment of the beam combiner results in a stable fringe pattern in the region of the coincident beams. This fringe pattern is readily observed by diverging the coincident beams with a negative lens and viewing the pattern on a white background. Proper alignment is achieved when the fringes are reduced in number until a single fringe is observed across the pattern. The single fringe pattern implies a phase difference

exists between the two beams across the beam cross-section of less than π radians and, hence, optical mixing will take place at the detector.

If a frequency difference exists between the contracirculating beams then a stable interference pattern will not exist. In this case it is necessary to obtain coarse alignment by aligning the beam combiner so that the two beams are visually coincident over a one meter or longer path. Fine alignment is done while observing the beat frequency output of the detector (preferably on a spectrum analyzer), and proper alignment is achieved when the amplitude of the beat frequency signal is maximized.

Proper operation of the optic mixer can be determined by visually observing a beat frequency signal on the spectrum analyzer. If either beam is blocked in the beam combiner, then the beat frequency amplitude should be decreased by roughly two orders of magnitude. This response indicates that the displayed signal is truly a beat between the two combined optic signals. A low level beat frequency signal is observed above when one beam is blocked because each of the individual signals is amplitude modulated at the beat frequency. Hence, the beat frequency can be monitored directly from either beam (Hutchings et al, 1966). If ultra-high reflectance mirrors are used in the ring, a convenient single beam output can be obtained by slightly rotating the plasma tube and utilizing the resulting reflection from one of the Brewster angle windows. The use of the beam combiner was preferred in these experiments because it was a true indication of the frequency difference between the beams and any amplitude modulation of the beams was at least two orders of magnitude below the beat frequency signal level. This greatly reduced any noise from this source.

III.1.3. Optical Detector

In order to measure the frequency difference between the contra-circulating beams, an optical detector was placed in the path of the overlaid beams after they emerge from the optical combiner. Two types of detectors were used in these experiments: vacuum photomultipliers and semiconductor photodiodes. By the proper selection of a cathode coating, the photomultiplier can be made more selective to a particular wavelength of incident light (i.e. selective to a particular photon energy). One commercial tube which is especially sensitized for the red portion of the spectrum is the RCA 4472. It is identical to the quite common 931A photomultiplier, except for the cathode coating. The 4472 was found to be about two times more sensitive at 6328 Å than was the 931A. Hence, the 4472 was used for all photomultiplier measurements.

The photodiodes used in this work were primarily from the Philco L4500 series, and they were operated in the photovoltaic mode well below their breakdown voltage. The L4501 and L4502 diodes have very high frequency capabilities (typically 15 to 25 GHz), but are of somewhat limited use due to their surface areas of 0.003 mm^2 and 0.01 mm^2, respectively. For incorporation into this system, these diodes would have to be located at the focal point of a positive lens which would be placed in the combined beam. This is simply not practical due to the critical alignment tolerances necessary. The L4504 diode has a surface area of 3.5 mm^2 and a correspondingly lower high frequency cutoff of 600 kHz. However, for detection of the beat frequency signal this bandwidth is quite sufficient. Again, the small surface area restricts the utility of this diode. An EG&G SGD-100A diode was also used with reasonable

success. This diode is designed for use with the EG&G HA-100 operational amplifier. When used in tandem, these devices offer a sensitive detector with a gain of 2000 from dc to 200 kHz. To achieve desirable signal-to-noise ratios, the incident illumination level on a semiconductor photodiode must typically be greater than 1 μwatt. This is necessary because the photodiode has an internal noise generator (shot noise) whose amplitude is fairly constant under varying illumination levels for a given temperature. At room temperature this noise level corresponds approximately to the signal level achieved from 1 μwatt of incident illumination. For incident power levels less than 1 μwatt the temperature of the photodiode must be greatly decreased to maintain a useful signal-to-noise ratio. In practice, a vacuum photomultiplier tube is found to have a better signal-to-noise ratio for incident powers less than 1 μwatt than does an amplified semiconductor photodiode, e.g. it was found that the signal-to-noise ratio of the 4472 photomultiplier was about an order of magnitude better than that of the L4504 photodiode for a typical output of the ring laser.

In practice, the optical detector was always located off the stable platform on a lab bench to eliminate the possibility of vibrations being transferred to the stable platform via the detector output and voltage leads. Usual beam combiner to detector separation was one to two meters. This practice also allowed the detector to be located very close to the amplifier-filter equipment used and, therefore, reduced stray pickup, especially from the RF transmitter.

III.1.4. Beat Frequency Signal Processing Section

The light amplitude incident on the photomultiplier was converted

to a voltage signal by detecting the voltage produced by the photomultiplier current when it passed through a 100 kilohm resistor which was inserted in series with the photomultiplier cathode (see Figure 5). The ac component of this signal was then capacitor coupled to the amplifier. The general scheme for processing the beat frequency signal is shown in Figure 1, where f_ω is not used for gas flow measurements. For the measurements on fused silica, all of the equipment illustrated in Figure 1 was used since it was necessary to detect, measure, and record both Δf_B and f_ω.

The beat frequency signal detected by the photomultiplier during gas flow measurements was amplified in an audio amplifier and then passed through an active bandpass filter to reduce noise and eliminate spurious pickup. The output of the bandpass filter was observed on the Panoramic spectrum analyzer and also clipped in a special clipping circuit. The spectrum analyzer allowed a visual indication for setting the center frequency and bandpass of the filter as well as indicated the amplitude of the amplified signal.

The amplitude of the beat frequency signal had frequent large variations which precluded direct frequency measurements. To allow precise measurement of the beat frequency on an electronic counter, it was necessary to level the amplitude of the beat frequency. This was conveniently done by using two germanium base-emitter semiconductor junctions in a passive back-to-back configuration along with a series dropping resistor as shown in Figure 6. The base-emitter junction of the General Electric GE-2 transistor becomes forward biased at approximately 250 mv and even when the device is driven with a 30 volt signal the forward bias holds the signal to less than 300 mv. Hence, any input

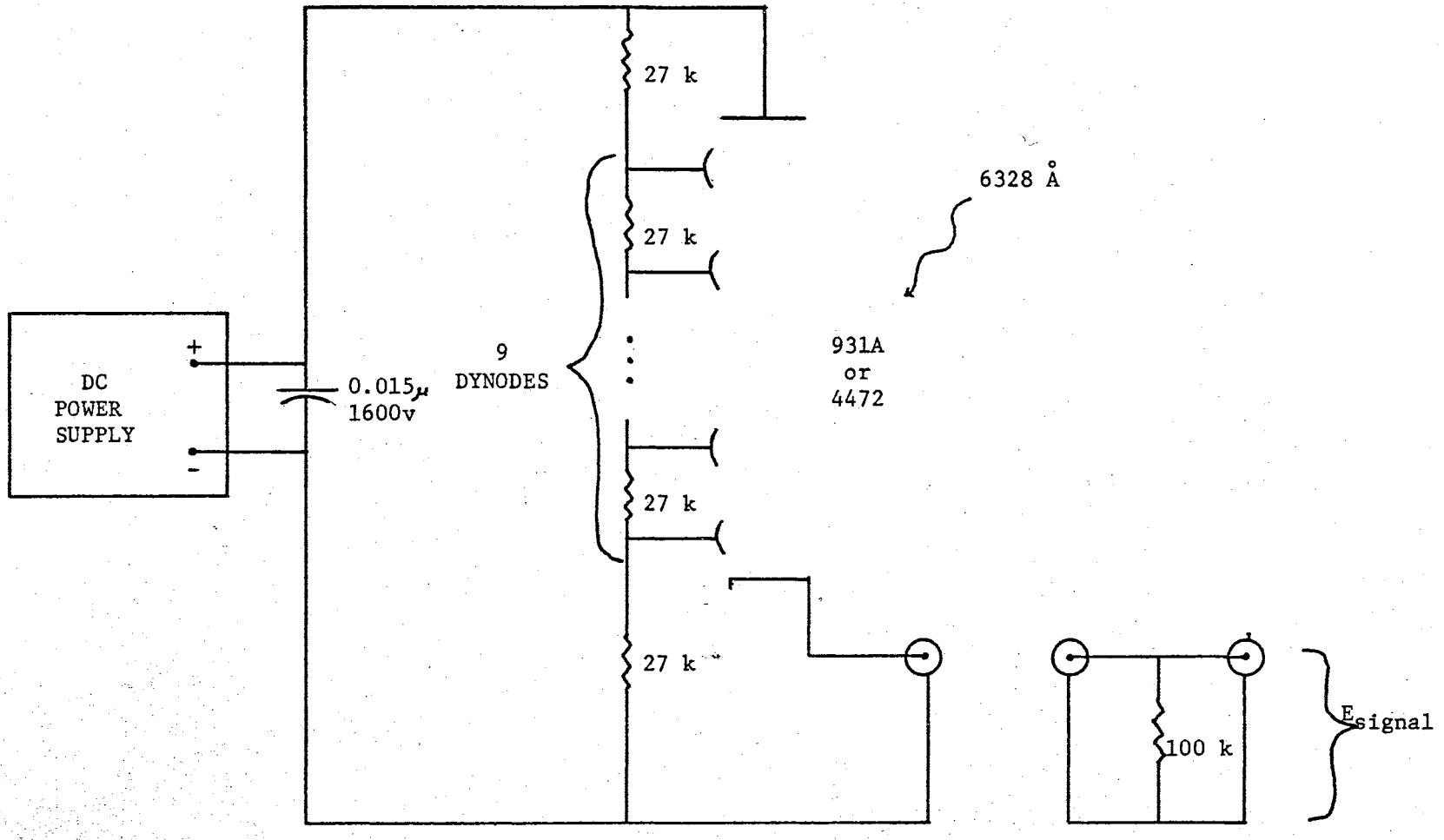

Figure 5. Schematic of the Photomultiplier Circuit

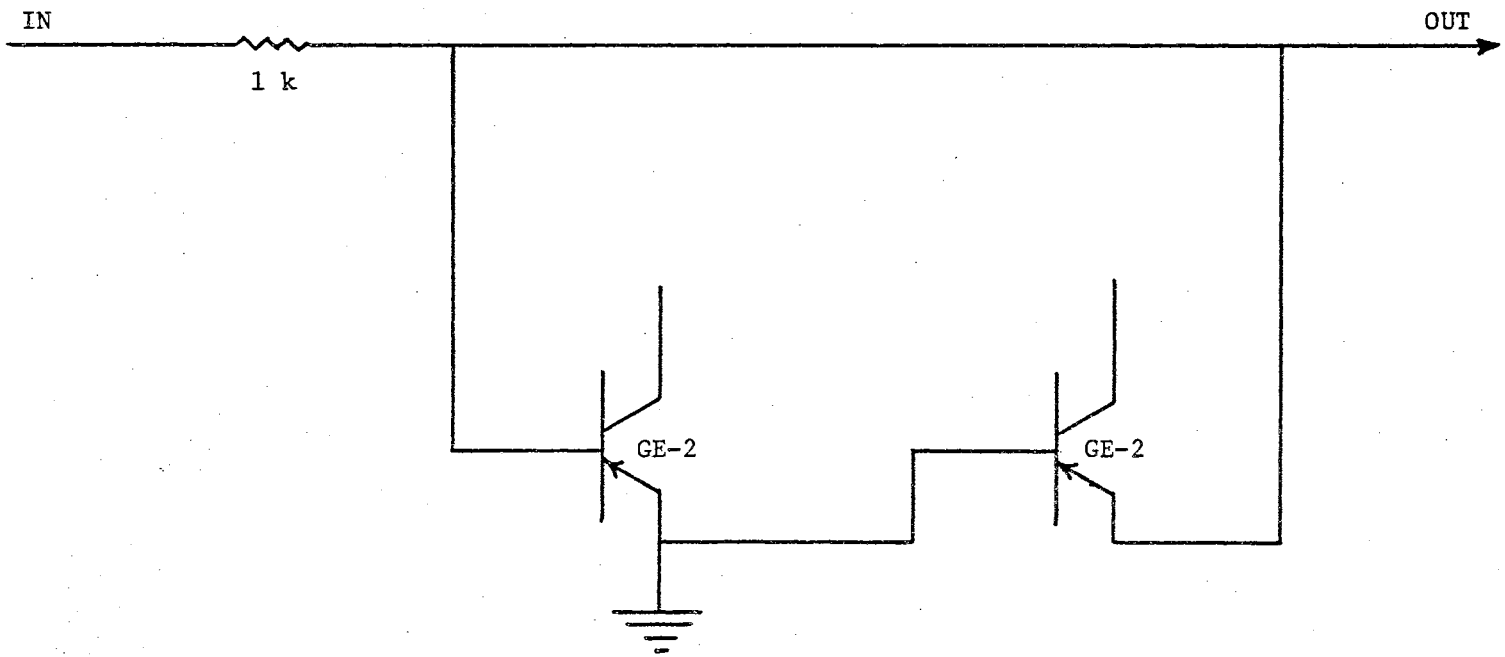

Figure 6. Schematic of the Passive Signal Clipper

signal greater than the forward bias is leveled to about 250 mv. This is an adequate voltage level for driving an electronic counter.

To assure that an adequate beat frequency signal was always present at the input to the electronic counter, the signal level at that point was monitored continuously by visual display on an oscilloscope. This signal monitor was maintained in addition to the spectrum analyzer monitor.

The beat frequency signal processing equipment used for taking measurements on fused silica is diagrammed in Figure 1. The beat frequency Δf_B detected on the photomultiplier was coupled into the ac input of a modified Tektronix Model 502 oscilloscope. The vertical amplifiers of the dual beam Model 502 oscilloscope were modified as shown in Figure 7 where the "B" input jacks to the vertical amplifiers were disconnected and the voltage from the vertical deflection plates was capacitor coupled to these jacks. In the case of the lower beam vertical amplifier, a high input impedance amplifier stage utilizing a 2N2844 field effect transistor was built into the oscilloscope to prevent loading of the vertical deflection plates if a lower impedance amplifier was connected to the "B" connection. The Model 502 oscilloscope as modified yielded an adjustable, very high gain amplifier which also had very low noise characteristics. The dual vertical amplifiers could be operated either separately or in series, with the lower beam amplifier always being used to feed the signal from the Model 502 to the next amplifier section. Typical vertical amplifier settings for appropriate gain were 50 mv/cm and 100 mv/cm for the upper and lower beam vertical amplifiers, respectively.

The output of the oscilloscope amplifier was both fed to a Hewlett-

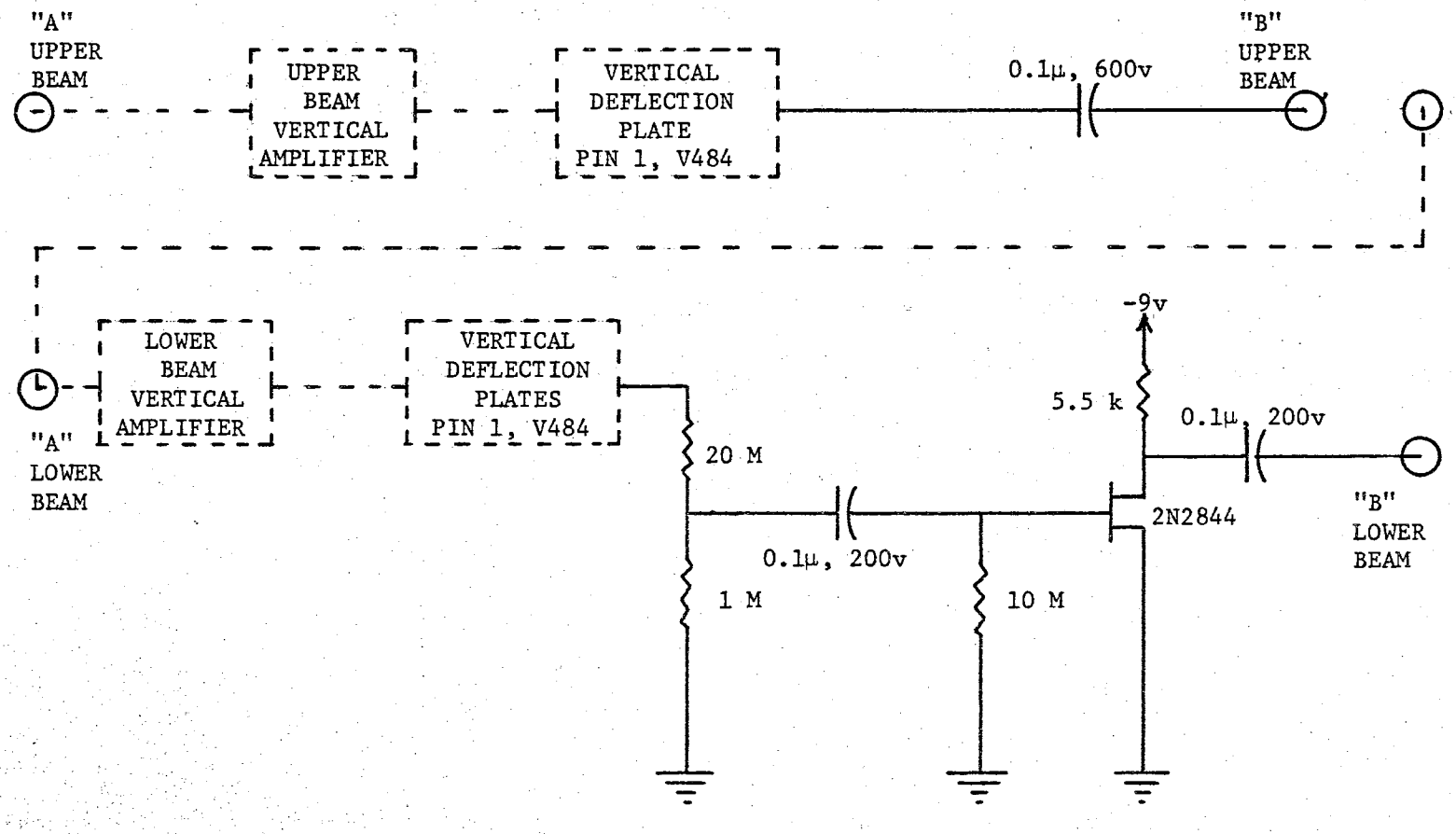

Figure 7. Schematic of the Model 502 Oscilloscope Modification

Packard (hp) Model 310A wave analyzer and monitored on the Panoramic spectrum analyzer. The center frequency indicated on the spectrum analyzer was used to find the correct response frequency on the wave analyzer. The Model 310A is an adjustable gain, adjustable bandpass amplifier-filter which can ordinarily be used to monitor any continuous sinusoidal signal whose frequency is between 1 kHz and 1.5 MHz. However, the unit available had a noise level of greater than 200 mv RMS, and the maximum sinusoidal output was less than 1 volt RMS. In addition, the unit tended to periodically have large amplitude fluctuations in the output signal. Hence, the Model 310A was used primarily as a narrow band filter whose rejection characteristics outside a 200 Hz bandpass were excellent. Bandpass widths of 1 kHz and 3 kHz were also available.

Since large amplitude fluctuations were again present in the beat frequency signal, the passive clipper of Figure 6 was used on the output of the wave analyzer. The clipped signal was then fed to an electronic counter and monitored on a second Tektronix Model 502 dual beam oscilloscope.

When beat frequency measurements were being taken on fused silica, its velocity was determined by monitoring the amplitude modulation of a light beam that was chopped by the rotator which held the fused silica. The exact scheme used will be described later in the section on the velocity detection system for solids. The resulting demodulated signal was amplified in the amplifier section of a Hewlett-Packard Model 400C vacuum tube voltmeter to a level sufficient to drive an electronic counter. Typically, the amplified signal level was greater than 500 mv RMS.

III.1.5. Data Accumulation Equipment

The signals used to measure both the magnitude of the dragging effect and the velocity of the fused silica were sinusoidal ac signals whose frequencies were proportional to the measured parameters. Hence, amplitude fluctuations did not affect the accuracy of the data and an exact count of these frequencies yielded the required information. Two separate electronic counters were used to simultaneously count these frequencies as indicated in Figure 1. The beat frequency was counted on a Hewlett-Packard Model 5280A/5285A reversible counter/universal plug-in combination and the velocity signal was counted on a Hewlett-Packard Model 5243L electronic counter. To insure that the beat frequency and velocity were determined over identical time periods, the time base of one counter was used to gate both counters. The gate trigger sync signal from the Model 5243L gate circuit was used to simultaneously trigger both the Model 5243L and the Model 5280A. The necessary circuitry is diagrammed in Figure 8. The Model 5280A was operated in the EXTERNAL SINGLE gate mode. To obtain proper triggering of the Model 5280A a rear panel TRIGGER LEVEL control must be properly adjusted. This setting was extremely critical for proper operation, but once set properly it never needed further attention. Since the Model 5280A does not have automatic reset capabilities, it was necessary to provide a reset signal at the beginning of each gated period. The reset signal was coupled off the trigger sync signal as shown in Figure 8 and used to momentarily saturate a 2N697 NPN transistor. The saturated transistor essentially shorts the reset signal to ground, thereby resetting the readout to zero. Even though the reset occurs at the beginning of the gated period,

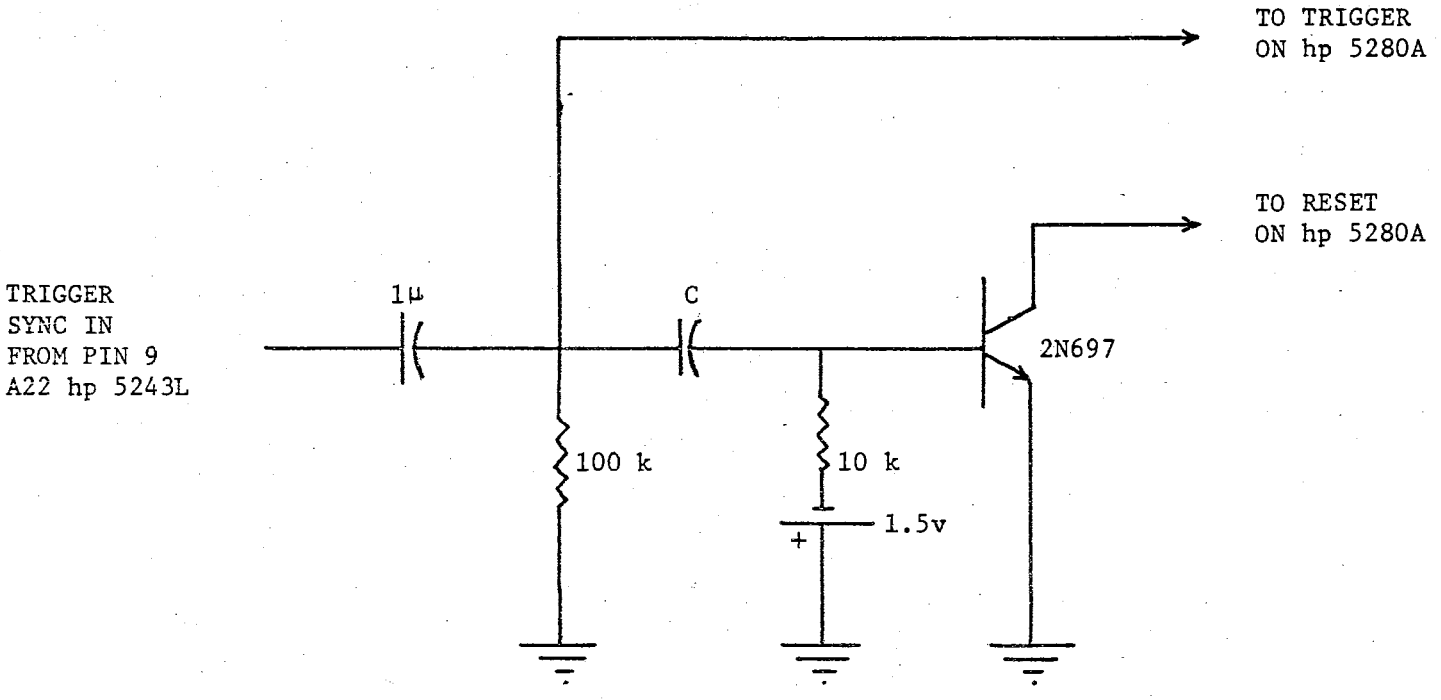

Figure 8. Trigger and Reset Schematic for Synchronizing the hp 5280A With the hp 5243L

its duration of less than 10 μsec is short enough that the resulting count error would only be one part in one hundred thousand for a one second count. Typically, the gated period was ten seconds with a resulting count error from resetting of one part in a million.

To insure that a signal level adequate for driving the counters was always present at their inputs, both counter input signals were monitored on an unmodified Tektronix Model 502 dual beam oscilloscope as indicated in Figure 1 and shown in Figure 9. This signal monitor allowed reliable adjustments to be made in the amplifier-filter system, indicated the minimum acceptable signal levels, and provided a direct indication of data counting irregularities. At the beginning of each data run the trigger level on the Model 5280A/5285A was set so that a zero count was obtained when the ring laser combined output beam was blocked from incidence on the photomultiplier.

Both electronic counters had a BCD-coded readout output available, so the counter outputs were cabled into a Hewlett-Packard Model 562A digital recorder. The eleven channel printout capability of the Model 562A was utilized by using five channels to print out the complete velocity (f_ω) data and five channels to print out the five least significant digits of the beat frequency (Δf_B) data. The sixth and seventh digits for the beat frequency data were manually noted on each data set. These digits corresponded to the 10 kHz and 100 kHz digits. The unused channel was utilized to conveniently separate the two sets of recorded digits. Since both counters were gated over identical time periods, their outputs were always available simultaneously and were printed simultaneously. This digital printout then provided a convenient record of the data for further data processing.

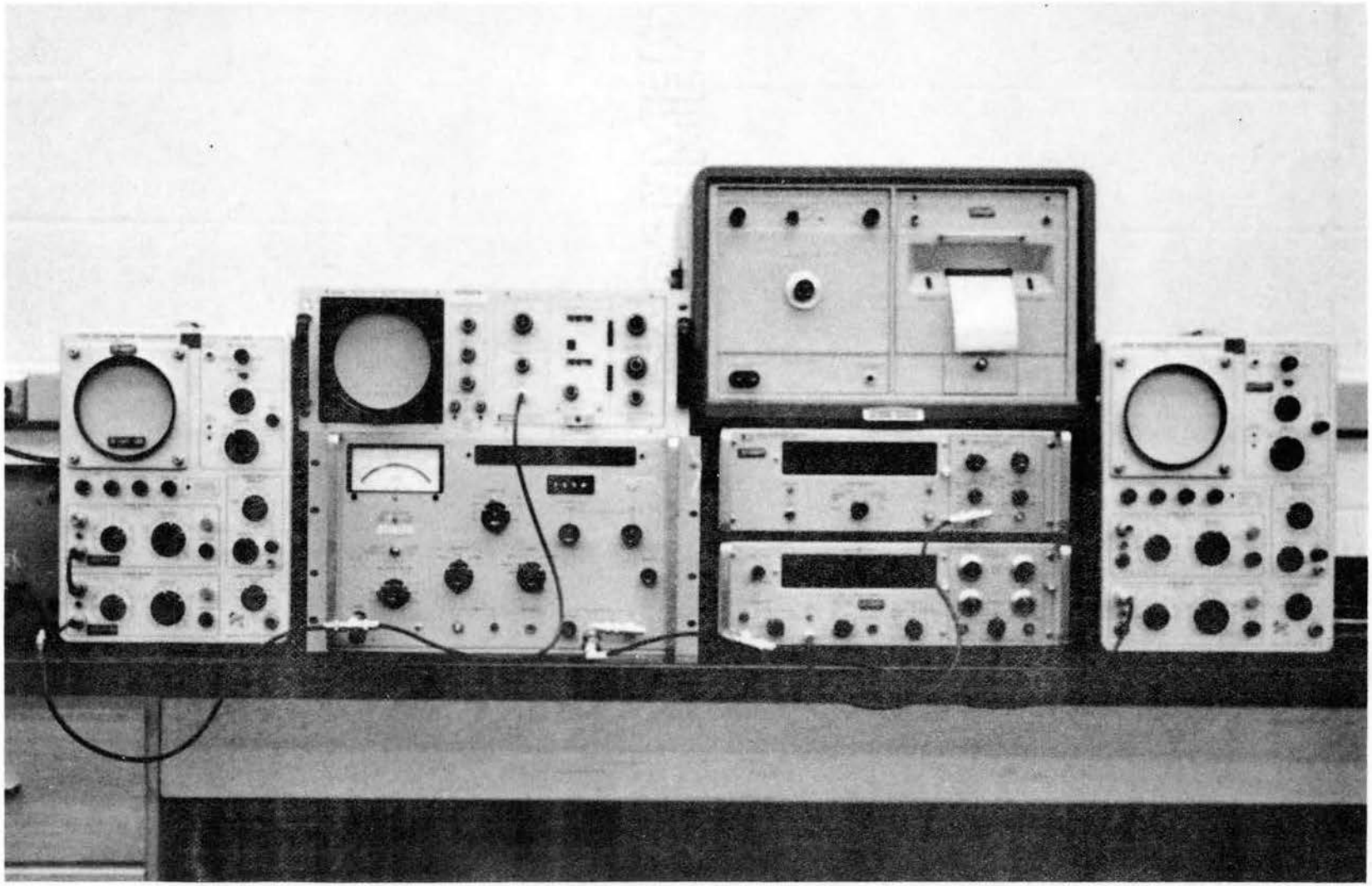

Figure 9. Electronic Equipment for Presenting Beat Frequency and Frequency of Rotation Data

III.1.6. Moving Medium

The use of flowing nitrogen gas for biasing the ring during the early experiments was facilitated by incorporating a long, thin flow tube into one arm of the ring laser. The two flow tubes used, which were designed to obtain as large an effect as was practical by using one arm of the ring, had a length of 90 cm and bores of 5.0 mm and 7.2 mm, respectively. The data presented in this work was taken with the 5.0 mm tube which seemed to have a more uniform and predictable flow pattern. Both tubes were terminated in Brewster angle windows which were held in gasketed holders. A flat stainless steel plate was epoxyed onto each end of the flow tube parallel to the cut Brewster angle ends of the flow tube. Each plate had an elliptic center hole large enough so the flow tube bore was unobstructed and three evenly spaced tapped screw holes for mounting a second similar plate. A thin, soft rubber gasket and the flat BK-7 window were held between the plates, with the gasket providing a seal between the window and the flow tube. The removable provision on the window design was necessary because the gas flow, even when filtered, caused occasional particle contamination of the inner surface of the windows. The gas flow entered and exited through side tubes at either end of the main flow tube. The 7.2 mm bore tube is shown in Figure 10.

The linear velocity component of fused silica was obtained by rotating a thick disc of this material internally in the ring laser such that the linear (tangential) velocity of the disc at some intercepted point would have a velocity component parallel to the beam. This method was originally used by Macek et al (1964). An illustration of the

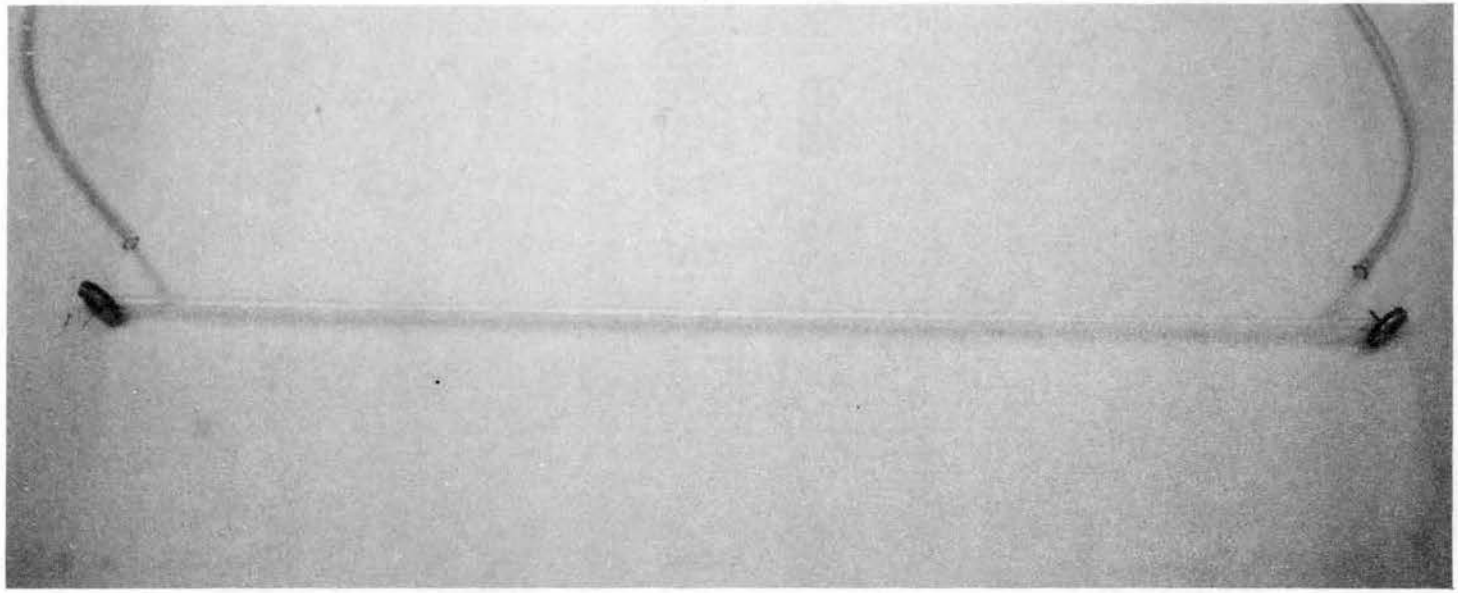

Figure 10. Flow Tube Used With Gas Flows

velocity components and contributions involved is shown in Figure 12. The optic flat (disc) was inserted in the ring with its flat faces set at their Brewster angle relative to the beam. The component of the velocity of the medium parallel to the beam (v_a) is given by Eq. (2-39) and Eq. (2-40) where the radius R is the distance from the center of rotation to the point where the intercepted beam is halfway through the disc as illustrated along with the coordinate system in Figure 11, Figure 12, and Figure 13.

Rotation of both solids and liquids was facilitated by placing the respective medium in a bearing mounted holder which in turn was mounted on an adjustable platform in such a manner that the medium could be optimumly adjusted, moved, and rotated. The platform required for holding the bearing mounts is photographed in Figure 14 and illustrated in Figure 15 and Figure 16. The base of the platform was mounted directly to the granite table top with a clear silicone sealing compound. The height and angle of the platform surface were adjusted by the nuts on the legs so that the surface was at the Brewster angle of fused silica with respect to the beam and also so that the normal to the surface was in a plane which was both normal to the ring and along the beam path in that arm of the ring laser. These adjustments were facilitated by placing the fused silica optic flat in the platform holder and minimizing the beam reflections off the front surfaces of the flat during actual operation of the ring laser.

The main platform, after being properly adjusted, remained in a fixed position throughout the experiments. Translation movement of the medium was provided by having the medium mounted in a second platform which could be moved and positioned precisely with respect to the pri-

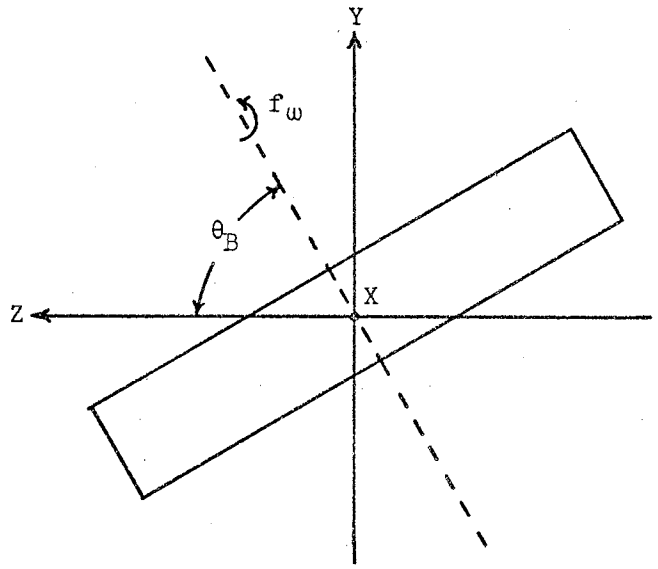

(a) Side View in the Plane of the Ring

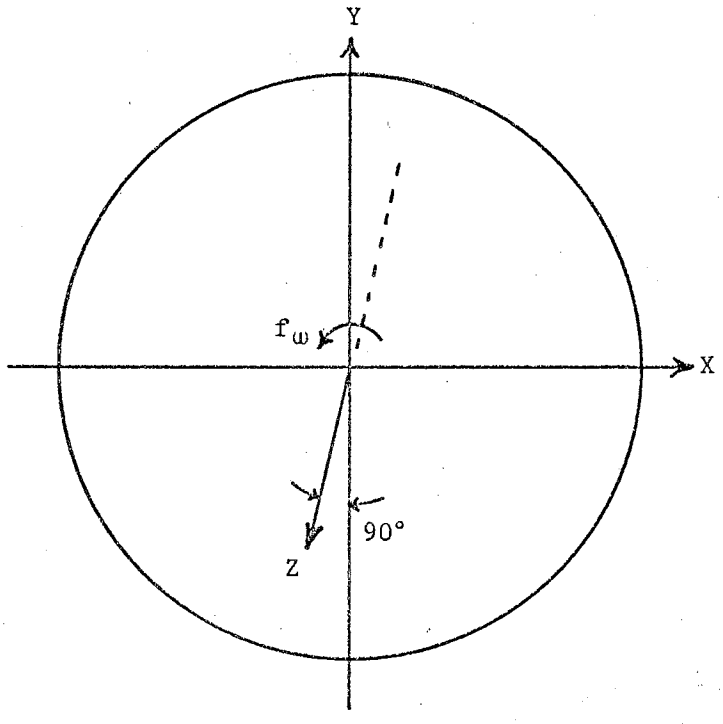

(b) Top View Along the Axis of Rotation in a Plane Which is Both Normal to the Ring and Along One Arm of the Ring

Figure 11. Axes Orientation for the Moving Medium

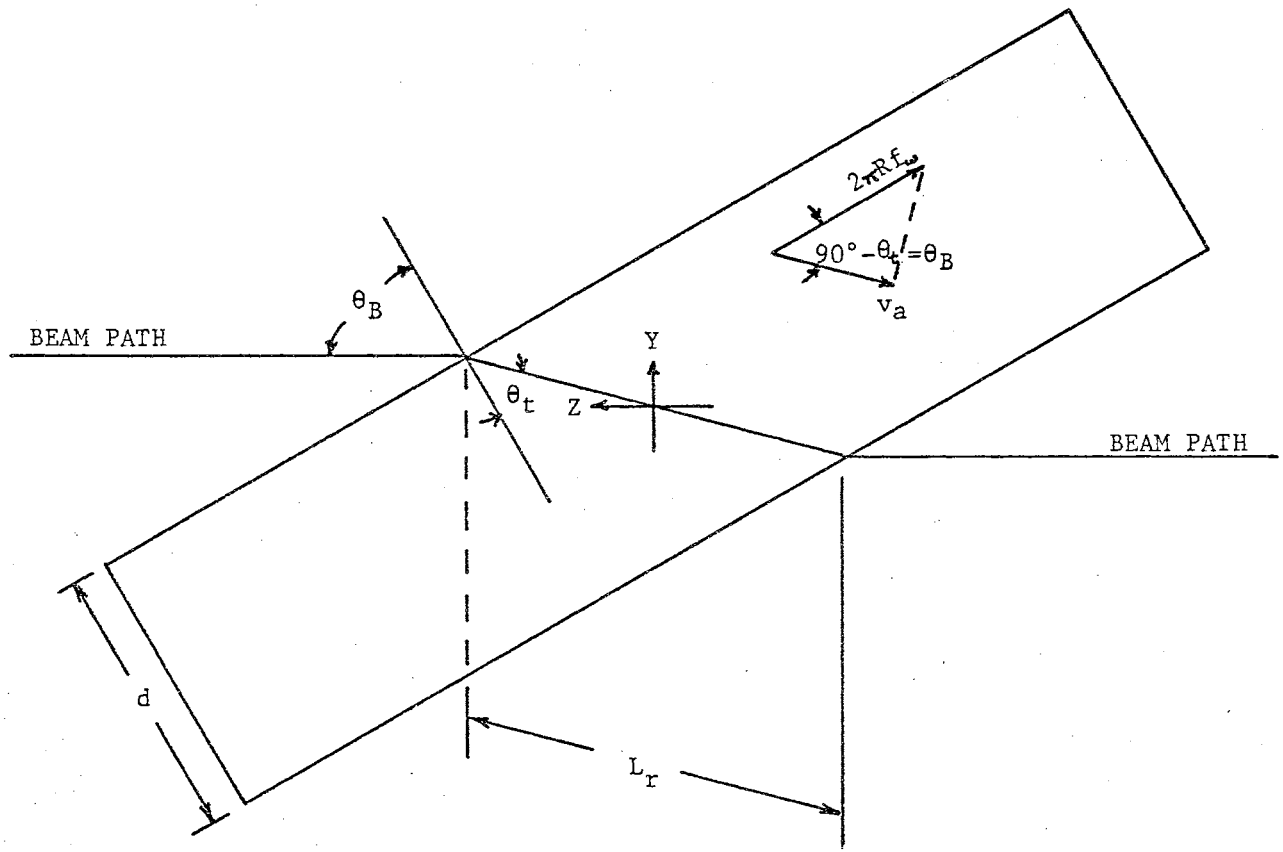

Figure 12. Beam Path Through the Moving Medium Illustrating the Tangential Velocity Projection

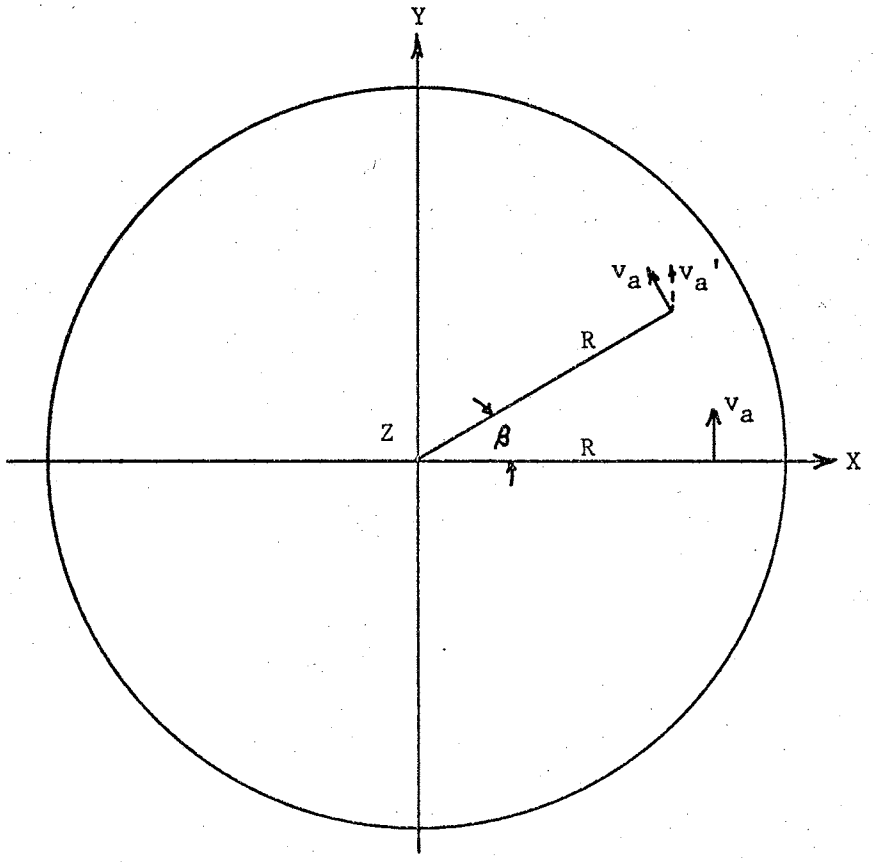

Figure 13. Illustration of the Effect of X-Axis Misorientation on Velocity Determination

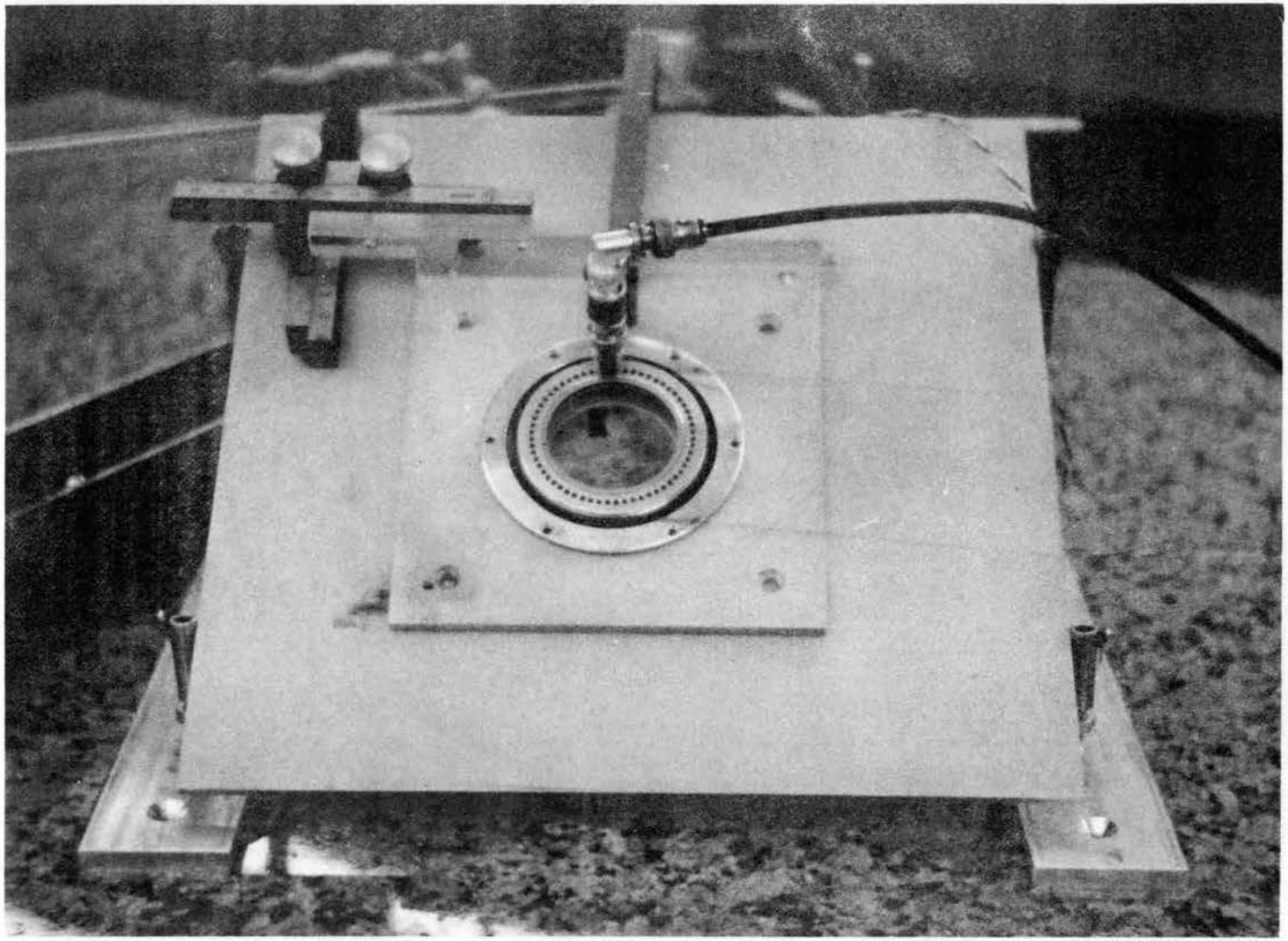

Figure 14. Rotator Platform Used for Rotating the Solid and Liquids

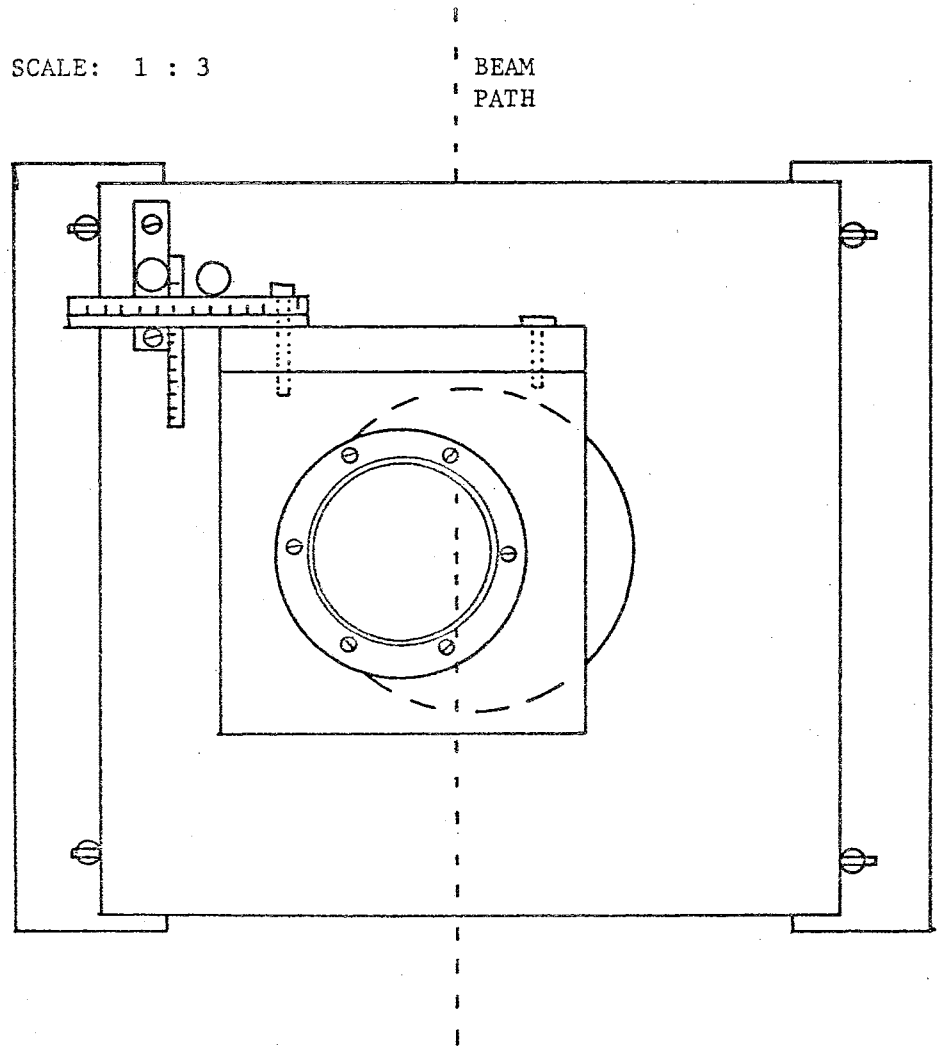

Figure 15. Top View of Adjustable Platform for Holding Moving (Rotated) Medium

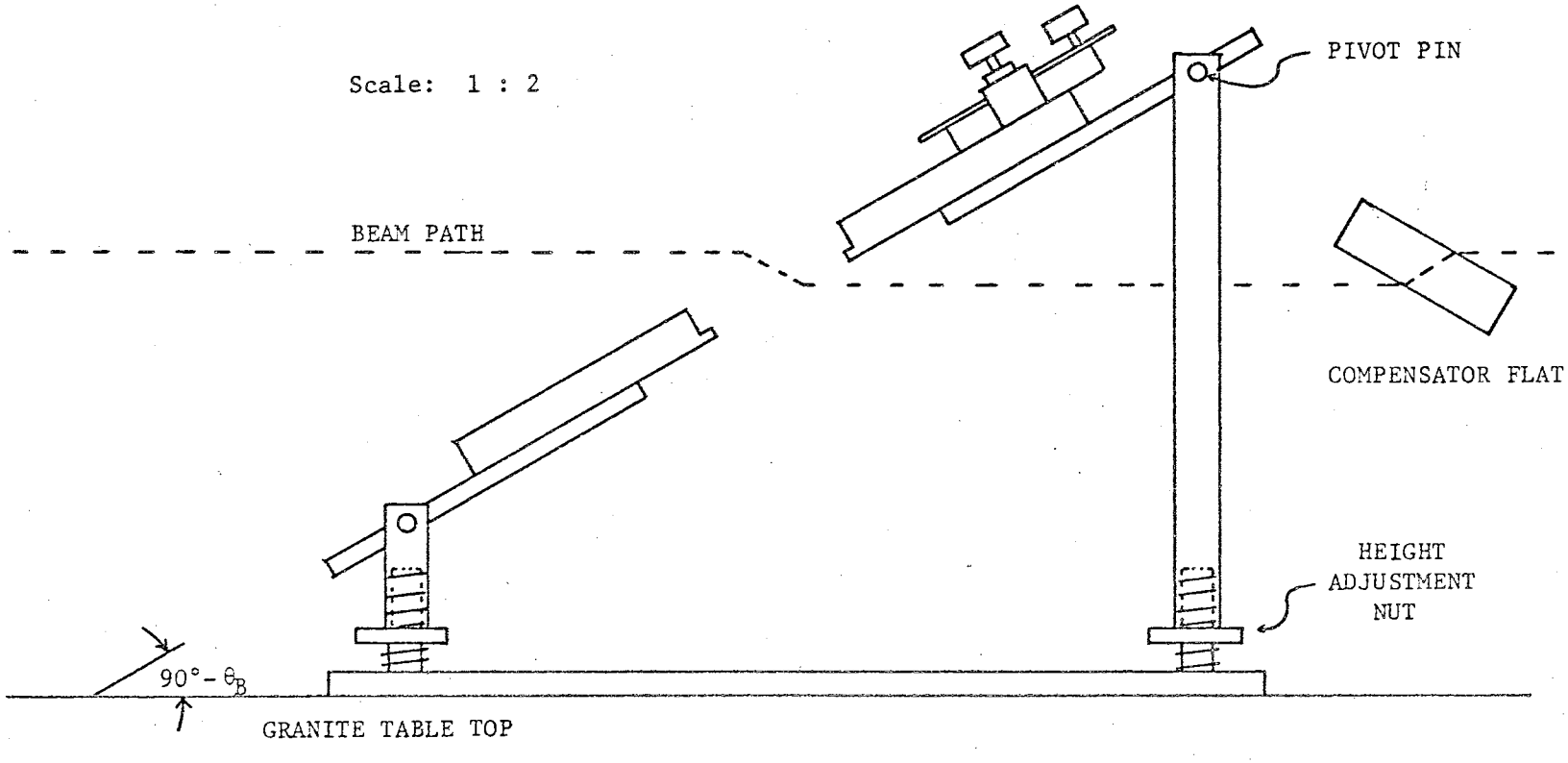

Figure 16. Side View of Adjustable Platform for Holding Moving Medium in Rotator

mary fixed platform. Adjustment and positioning were provided by a 0.1 mm resolution x-y vernier which held the moving platform. In order that the medium could be translated at least 2 cm in any direction from the center position, a 5 inch cutout was provided in the center of the stationary platform surface. The dashed line in Figure 15 and Figure 16 indicates the path of the laser beam during normal operation with the fused silica optic flat positioned in the platform. Figure 16 also shows the placement of the compensator flat which is necessary to compensate for the beam offset in the rotated medium.

The fused silica optic flat was rotated by mounting it in an especially designed sleeve with a high speed bearing as diagrammed in Figure 17 and photographed in Figure 18. The entire assembly rested against a lip in a presized cutout in the movable part of the platform. The assembly was secured in the platform by an annular disc cover as shown in Figure 15. The special sleeve was made of aluminum with brass retaining rings as shown in Figure 17. The use of the retaining rings made quick and easy assembly and disassembly possible and decreased the probability of strain damage to the fused silica optic flat. The 2.000 inch diameter optic flat was positioned in the sleeve by resting against a 0.05 inch lip at the bottom of a 2.005 inch diameter cutout which was precision machined in the center of the sleeve. The inner surfaces of the cutout and the lip were spray coated with a teflon aerosol to provide a slick, protective film to aid in inserting and withdrawing the optic flat as well as to protect the optic flat from chipping.

The body of the sleeve had 60 small holes drilled completely through it. These holes were evenly spaced at 6 degree intervals along a contour of constant radius, and were used to chop a light beam to in-

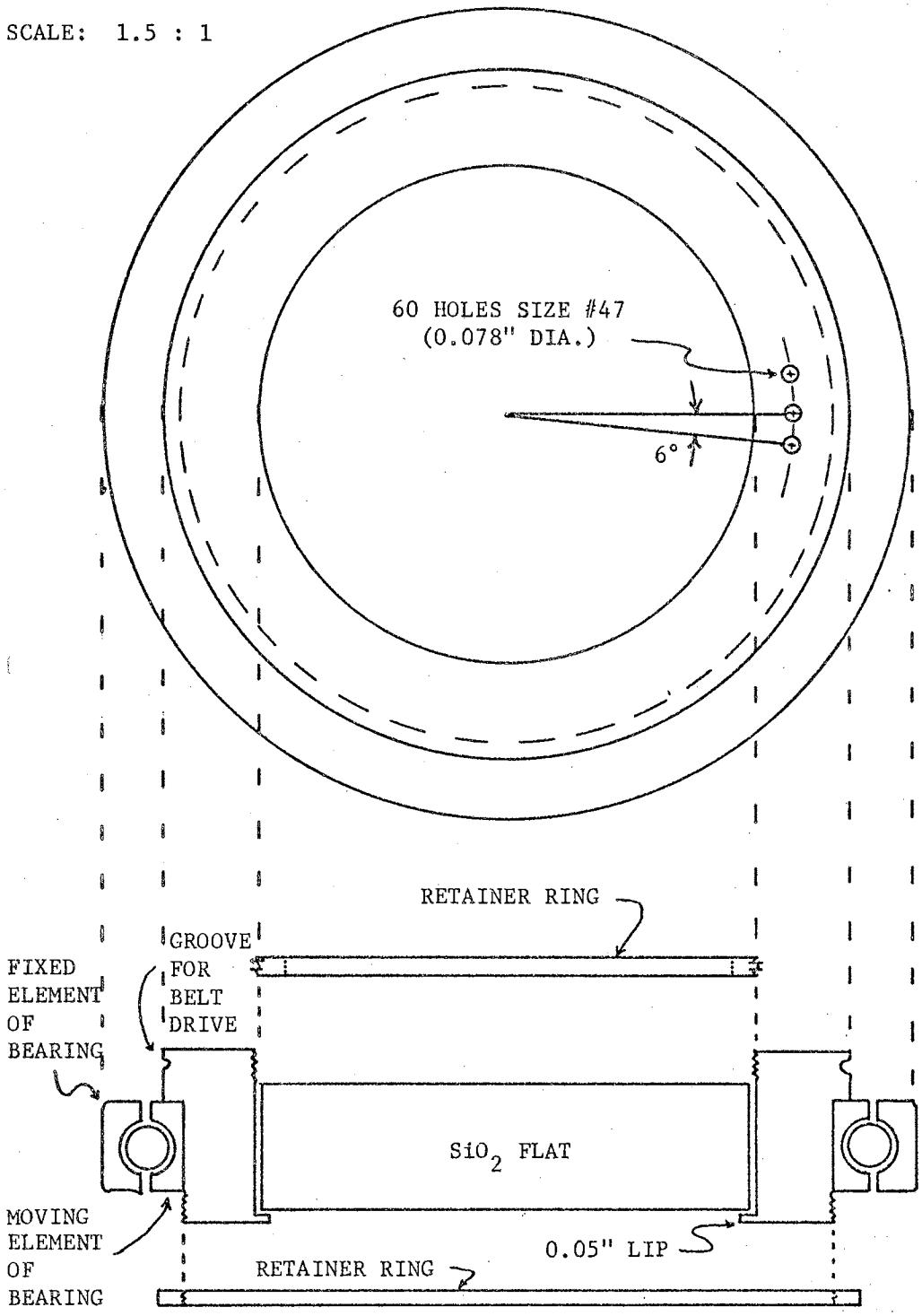

Figure 17. Schematic of Sleeve and Bearing for Rotating the Fused Silica Optic Flat

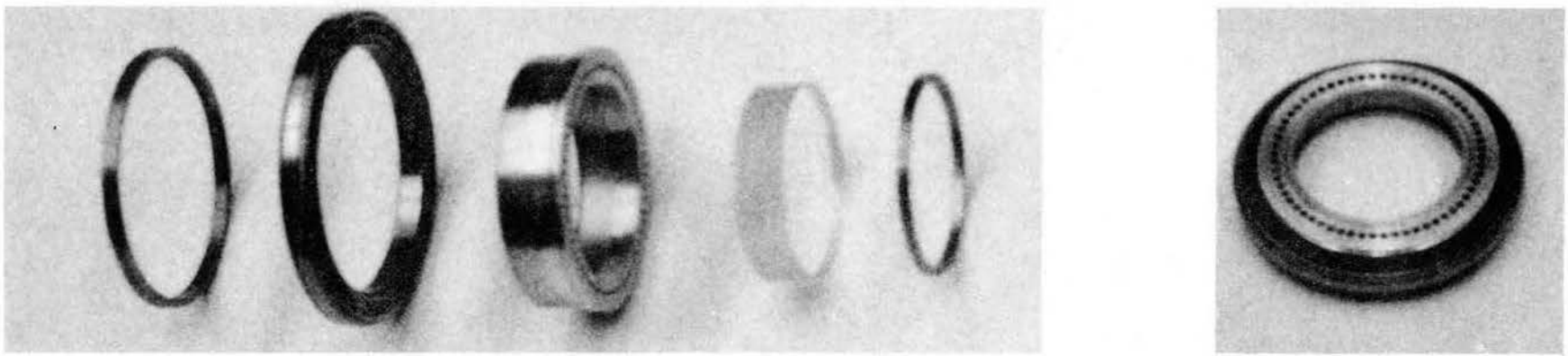

(a). Unassembled (b). Assembled

Figure 18. Sleeve and Bearing Assembly Used for Rotating the Fused Silica Optic Flat

dicate the angular velocity of the sleeve. Provision was made for driving the sleeve with a belt connection by channeling a small groove in the outer sleeve wall.

The bearing used in conjunction with the sleeve was a high speed, precision ball bearing manufactured by Split Ball Bearing Company as Model 3 TKR 41-52-U. Since very low bearing friction was essential and because the bearing was specified to have only 0.0005 inch radial play, a special lubricant was required. Several newly developed solid, dry lubricants were tried. The best performance was obtained using tungsten diselenide of 1 μ to 2 μ particle size obtained from Cerac, Inc., as lubricant #1433. To apply this lubricant, it is necessary to very thoroughly clean the bearing in a solvent, such as naptha, and then very lightly, but thoroughly, burnish all moving surfaces of the bearing with the lubricant. Proper application of the lubricant will provide more than 100 hours of operation without loss of the lubricating coating.

The four optic flats used in these experiments were all high quality fused silica optic flats. Specifications for these optic flats are given in Table I. Optic flat number 1 was used as the rotated fused silica medium, while flat number 2 was used as the beam compensator. Optic flats number 3 and 4 were used as the windows on the liquid cell. Optic flat number 1 was of exceptional quality. The material used in it is supplied by Amersyl Corporation under the tradename HOMOSIL. This material was chosen for use as the moving solid medium because it has a quite noticeable dispersion ($dn/d\lambda$), has very low optic losses, and is very homogeneous. In addition, HOMOSIL is very stable, inert, and can be supplied with a very smooth optic finish. The index of re-

TABLE I

OPTIC FLAT SPECIFICATIONS

Optic Flat Number	Supplier	Surface Flatness	Parallelism (arc sec)	Diameter (inches)	Thickness (inches)
1	Oriel Optics	$\lambda/20$	1	2.000	0.5029
2	Special Optics	$\lambda/10$	5	2.000	0.4866
3	Dell Optics	$\lambda/10$	--	2.002	0.2506
4	Dell Optics	$\lambda/10$	--	2.000	0.2497

fraction and the dispersion are also precisely known.

The power necessary for rotating the sleeve used with the solid was supplied through a belt drive from a 1.4 oz-in speed regulated motor. The motor used was a Model E-350 MG obtained from Electro-Craft Corporation. The associated power supply, Model E-350 M (also from Electro-Craft), provided the necessary voltage to the motor so that the speed could be set and automatically controlled at any speed from 10 RPM up to 9,000 RPM. The necessary error signal for controlling the motor speed is obtained from a special tachometer generator built into the motor. Consistent and smooth control at low speeds is obtained through the use of this separate generator winding and silver contacts on the generator. The speed of the Model E-350 MG motor was found to change over 3 RPM for each volt change in the line voltage to the Model E-350 M controller power supply. Therefore, the 40 watts of input power to the Model E-350 M were supplied through a 150 watt capacity Sola constant voltage transformer. This reduced the speed variations of the Model E-350 MG to about 0.2 RPM per volt line change.

To reduce the transmission of vibrations to the vibration isolated table top, the motor was mounted on a second table next to, but separated from, the vibration free table. Hence, a 30 inch, non-vibration transmitting belt was necessary to transmit the power from the motor to the respective sleeve. A single strand of #50 cotton thread proved to be ideal. In order that the sleeve speed be the same as that of the drive motor, a special 2.84 inch diameter pulley was machined and mounted on the motor shaft. This allowed the metered RPM of the motor to be used as a coarse indicator of the sleeve RPM. In addition, the metered RPM served as a check of f_ω.

III.1.7. Velocity Detection Systems

The velocity of the nitrogen gas flow was obtained by precisely timing the interval of time it took for a measured volume of gas to pass through the flow tube. Timing was done with a stopwatch which was readable to 0.1 second accuracy. The volume of gas was measured by connecting a precision wet test meter to the output of the gas flow tube. The wet test meter is essentially a paddlewheel submerged in water, and the gas flow rotates the paddlewheel such that its total rotation is proportional to the volume of gas which has passed through it. The accuracy of the wet test meter is 0.5% when properly operated and compensated. The velocity of the gas was then calculated by dividing the volume per unit time by the cross-sectional area of the flow tube. At best, this average velocity is only an approximation to the true velocity along the axis of the flow tube. However, since absolute measurements of the dragging effect of gases were not being made and only relative biasing effects were being utilized, a very accurate velocity definition was not necessary.

The velocity detection system used with the fused silica solid was quite unique and precise. As described in the previous section on moving media in this chapter, the linear velocity of the solid parallel to the laser beam is determined from the angular rotation frequency of the solid. Hence, it was desirable to count the angular rotation frequency in Hz, or preferably, in RPM (revolutions per minute). This angular rotation frequency f_ω was precisely determined for the solid by chopping a light beam with the sleeve which rigidly held the solid. The sleeve had 60 small, evenly spaced holes drilled through it (see Figure

17), and a prefocused light bulb and detector were mounted below and above the sleeve, respectively, as shown in Figure 14. The chopped light beam from a GE 253 bulb was detected by a Philco L4501 photodetector and amplified in the amplifier section of a Hewlett-Packard Model 400C vacuum tube voltmeter to a level greater than 0.1 volt RMS (typically greater than 0.5 volt RMS). This signal was then counted on a Hewlett-Packard Model 5243L electronic counter. The use of 60 holes provides a chopped beam frequency of 60 times the angular rotation frequency f_ω for f_ω in Hz. However, when this frequency is counted by an electronic counter with a one second gating period, the digital readout is exactly f_ω in RPM (revolutions per minute). For a 10 second gating period the digital readout is exactly 10 f_ω (in RPM). The digital readout is accurate to $\pm$ one count so that for a 10 second gating period the error in f_ω is $\pm$ 0.1 RPM.

III.1.8. Peripheral Measuring Equipment

The measurements taken of axial mode separation in both the ring laser and the 35 mw linear laser, as described in the Section IV.2.1., utilized the equipment shown in Figure 19. The output of the RCA 4472 photomultiplier was fed directly into a Tektronix Model 1L20 spectrum analyzer plug-in in a Tektronix Model 535 oscilloscope. Simultaneously, a 100 mv RMS sinusoidal voltage from a Hewlett-Packard Model 608C V.H.F. signal generator was fed to the Model 1L20 spectrum analyzer through a 510 kilohm resistor and to a Hewlett-Packard Model 524D electronic counter with either a Model 525A 10-100 MHz mixer plug-in or a Model 525C 100-510 MHz plug-in. The V.H.F. signal generator output cable was terminated in a 50 ohm resistance to properly match the RG 58/U coaxial

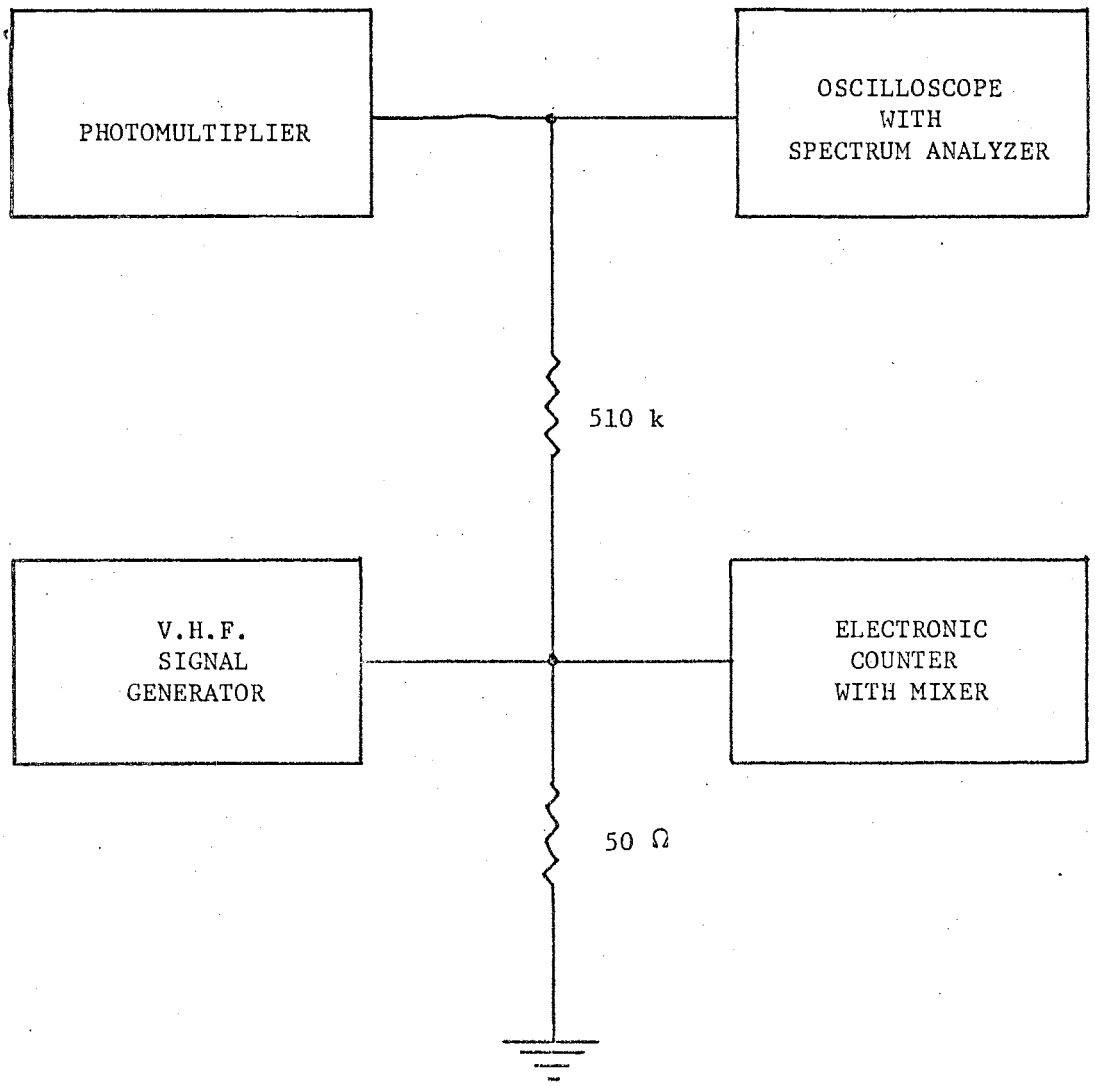

Figure 19. Block Diagram of Apparatus to Measure $\Delta\nu_{axial}$

cable. The 510 kilohm resistor provided a greatly reduced V.H.F. signal for display on the Model 1L20 and isolated the photomultiplier from the signal generator and counter circuits.

The equipment used to measure the index of refraction n by determining the Brewster angle of the material, as illustrated in Figure 20, consisted of a Spectra Physics Model 132 He-Ne laser, a polaroid lens from a pair of sunglasses, a Special Optics Model 100-30 precision angle rotator, and a white cardboard screen. The Model 132 laser features a 1 mw unpolarized output at 6328 Å which can be polarized to better than 95% by the use of the single polaroid sunglass lens. The Model 100-30 precision angle rotator can be read to 0.1 degree accuracy and has a full 360 degree rotation capability.

The Model 132 laser with the polaroid polarizer was also used in the scheme to measure transmission losses through the liquids as shown in Figure 21. The mirror used to direct the laser beam into the ring for these measurements was a high quality aluminumized front surface mirror with a surface flatness of $\lambda/4$ obtained from Edmund Scientific as SN 30286. The power meter and detector used for measuring the power level were the Spectra Physics Model 401B and its associated photovoltaic detector cell. The recorder output voltage of the Model 401B was read out digitally through the use of a Hewlett-Packard Model 3440A/3444A digital voltmeter/dc plug-in combination.

The linear laser which utilized the internal sample for the axial mode separation method of determining the index of refraction was a custom version of the Spectra-Physics Model 125 laser. Its plane-polarized output at 6328 Å was nominally 35 mw. The cavity configuration was such that the plasma tube and end reflector on one end were separa-

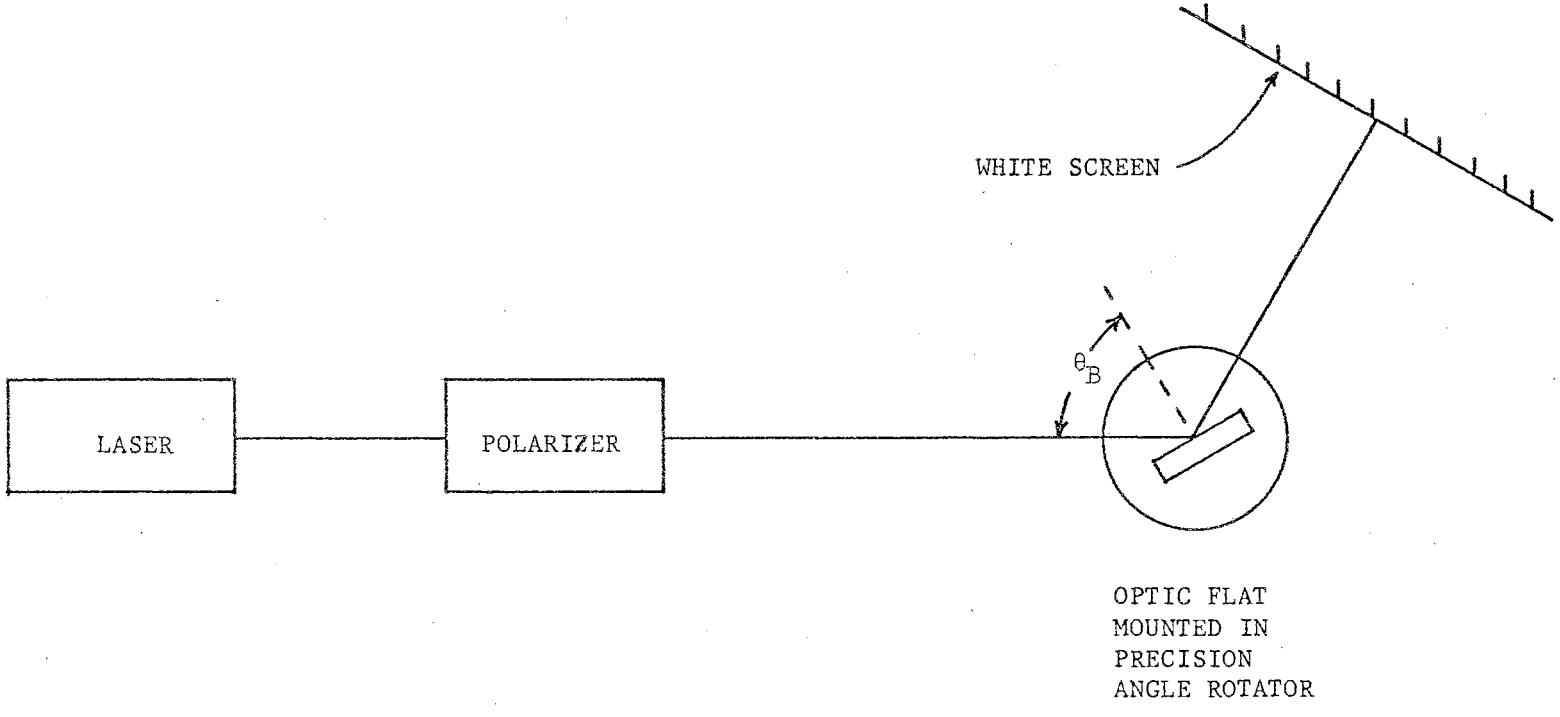

Figure 20. Diagram of Equipment to Determine n by Measuring θ_B

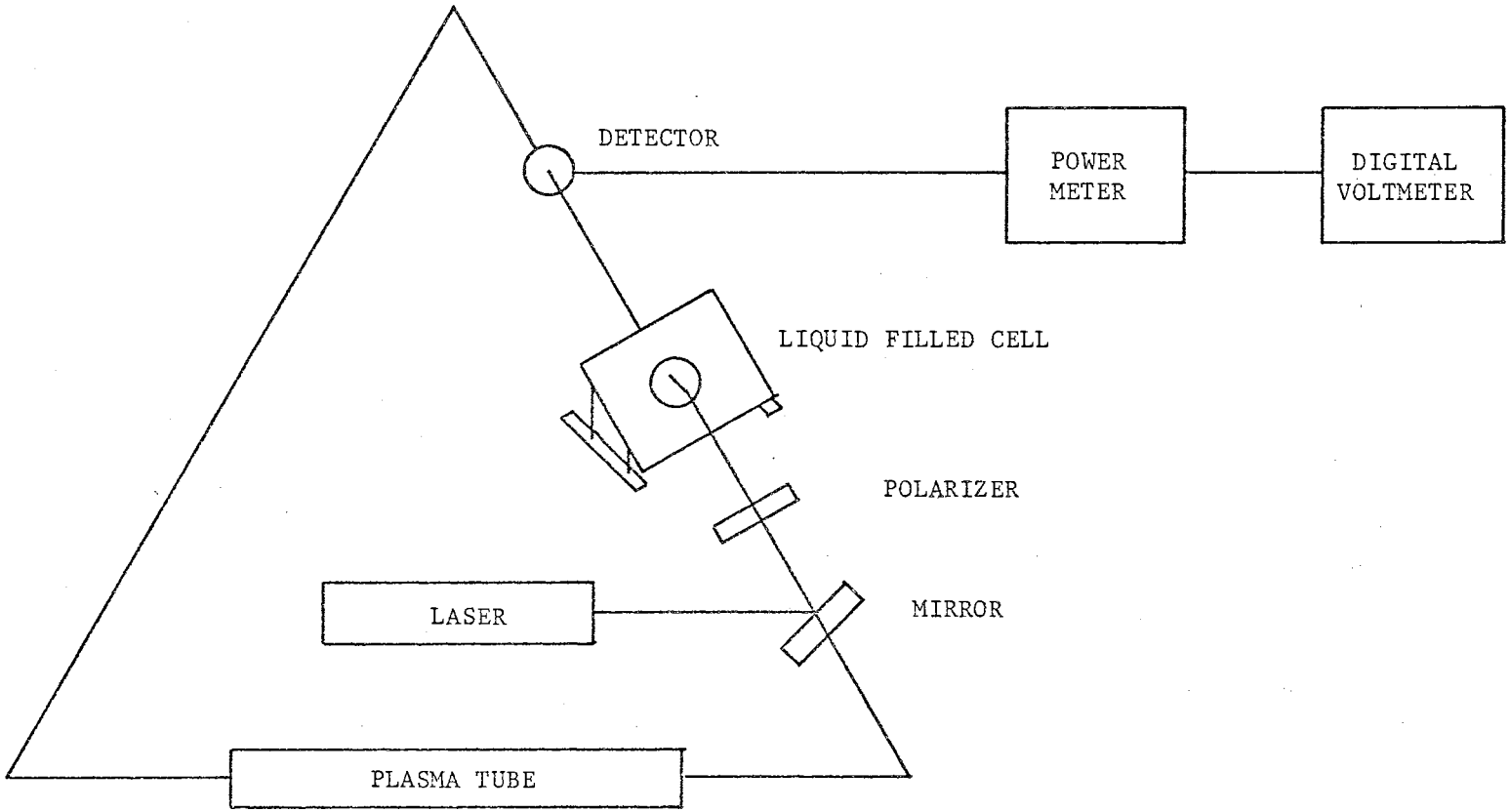

Figure 21. Block Diagram of the Scheme Used to Measure Transmission Losses Through Liquids

ted by about six inches, thereby providing a convenient working space for inserting a sample into the cavity.

Photographs of the major pieces of equipment used in this work appear in the figures. The sleeve used for holding the solid is pictured in Figure 18. Figure 2 is a view of the ring laser containing the platform for rotating the respective medium. The plasma tube amplifier is in the lower horizontal arm of the ring. The rotator drive motor can be seen to the extreme right center of the photo. The optic beam combiner, seen in the top center of the table, is pictured in more detail in Figure 3. The flow through tube pictured in Figure 10 was typically inserted in the open arm of the ring laser for incorporation into the system. The platform assembly for holding and positioning the solid or liquid is shown in a detailed photo in Figure 14. Figure 9 shows the major electronic equipment used in amplifying the beat frequency Δf_B (in Hz) and in displaying and recording both Δf_B and the angular rotation frequency f_ω (in RPM). An overall view of the laboratory and equipment placement is shown from two positions in Figure 22 and Figure 23. A complete list of the equipment used in the experiments is given in Table II.

III.2. Operation of the Equipment

Optimum performance of the equipment requires that certain procedures and techniques be used both in turning on the equipment and in operating it. At this point it will be assumed that sufficient detail exists elsewhere in this report to allow proper hook-up of all the equipment. Several pieces of equipment require a warm-up period to obtain optimum performance, and in some cases a warm-up is essential to

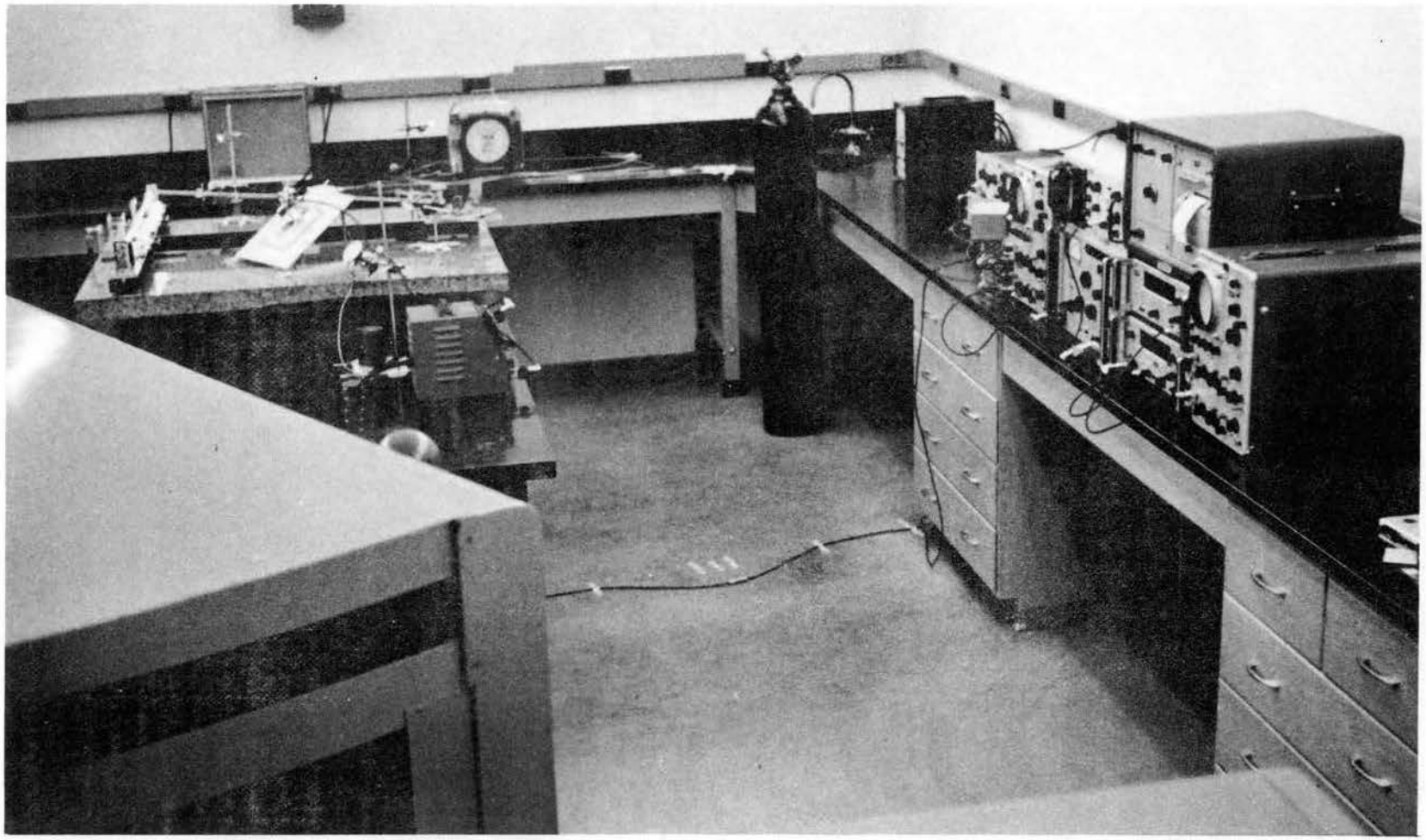

Figure 22. Pictorial View of the Equipment Used in the Experiments

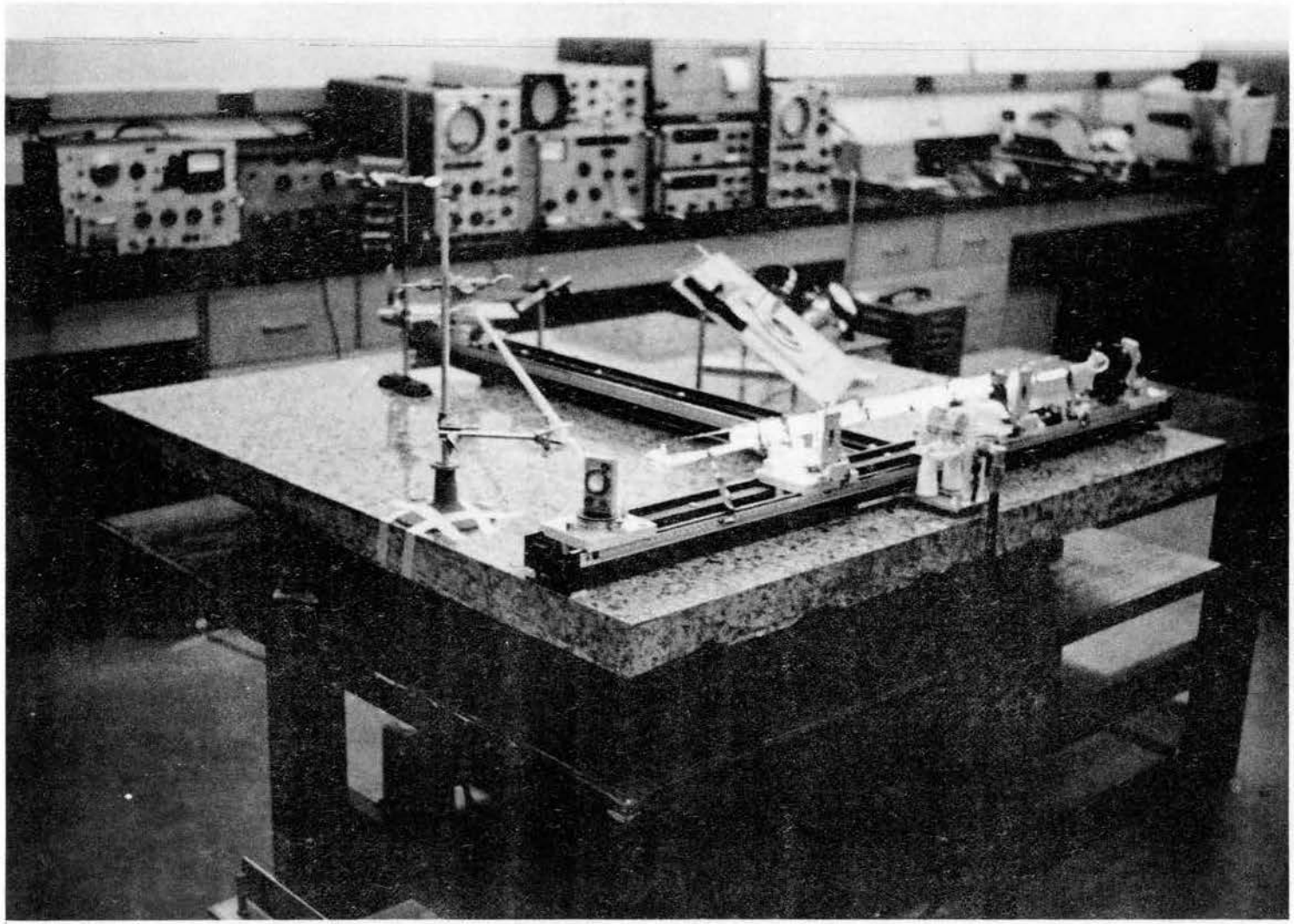

Figure 23. Pictorial View of the Vibration Isolated Table and Associated Equipment

TABLE II

PRIMARY EQUIPMENT UTILIZED IN THE EXPERIMENTS

Equipment Name	Manufacturer	Subsystem
Plasma Tube	PEK Labs	Ring Laser
RF Transmitter	Viking	Ring Laser
Mirrors	Perkin-Elmer	Ring Laser
Granite Block	Texas Granite Corp.	Ring Laser Platform
Photomultiplier	RCA	Beat Frequency Detection
Photodetector	Philco	Rotation Freq. Detection
Motor	Electro-Craft	Moving Medium (Rotated)
Motor Control	Electro-Craft	Moving Medium (Rotated)
$\lambda/20$ Optic Flat - Fused Silica	Oriel Optics	Moving Medium - Solid
$\lambda/10$ Optic Flat - Fused Silica	Dell Optics	Moving Medium - Liquids
$\lambda/10$ Optic Flat - Fused Silica	Special Optics	Compensator
Oscilloscope	Tektronix	Beat Frequency Detection
Wave Analyzer	Hewlett Packard	Beat Frequency Detection
Spectrum Analyzer	Singer	Beat Frequency Detection
Plug-In	Singer	Beat Frequency Detection
Electronic Counter	Hewlett Packard	Beat Frequency Detection
Electronic Counter	Hewlett Packard	Rotation Freq. Detection
Digital Printer	Hewlett Packard	Data Accumulation
Power Meter	Optics Technology	Power Measurements
He-Ne Laser (1 mw)	Spectra Physics	Loss Measurements
He-Ne Laser (35 mw)	Spectra Physics	Axial Mode Measurements
Precision Angle Rotator	Special Optics	n Measurements

proper operation of the equipment involved.

Energizing the laser plasma tube amplifier is the only turn-on procedure which requires a specific, sequential procedure. The RF transmitter must first be turned on to the warm-up or tune mode at least one minute before it can be switched to its cw mode to supply RF power to the plasma tube. When switched to the cw mode, the RF transmitter must be quickly tuned for output impedance matching and power output. The 1 m plasma tube used typically required 50 watts of RF power input. After 10 minutes of operation, the RF transmitter controls should be optimized. During subsequent ON-OFF cycles, the RF transmitter controls should need no adjustment, although occasional "touch-up" of the controls is to be recommended. The laser plasma tube should be allowed to operate continuously at least 30 minutes prior to any measurements to insure that equilibrium conditions have been met in the plasma tube and to insure its stable gain operation.

Just as the laser amplifier requires warm-up, so do all of the amplifier circuits involved in the instrumentation. This requirement essentially applies to all of the electronics with the exception of the digital counters and the digital printer. However, the crystal in the time base for the gated counter must be at its controlled operating temperature. In the counter used, the crystal temperature was automatically controlled as long as the ac cord was connected to a "live" ac outlet. The drive motor and rotator should also be run several minutes at the anticipated f_{ω} to allow steady state conditions to be attained for both the motor and the rotator bearing.

After stable operation of the plasma tube has been reached, the mode structure of the oscillating beam must be reduced from its unob-

structed TEM_{1pq} mode of oscillation to a single-valued q TEM_{00q} mode. The mode structure was conveniently reduced to a multi-valued q TEM_{00q} pattern by reducing the adjustable iris opening, and observing the beam pattern. To verify single-valued q TEM_{00q} mode operation, one must use a spectrum analyzer tuned to the lowest axial mode separation frequency. The absence of this beat signal in the presence of laser oscillation indicates pure single-valued q TEM_{00q} mode operation. In practice, the lowest axial mode separation frequency (92.0 MHz) was observed on the Model 1L20 spectrum analyzer, and the plasma tube gain was reduced by decreasing the RF power until the mode separation frequency signal disappeared.

Other operating procedures necessary to insure proper data accumulation are discussed with the pertinent equipment or experimental procedure in Chapter III and Chapter IV.

CHAPTER IV

EXPERIMENTAL PROCEDURE

IV.1. Gases

Due to the lock-in characteristics of a ring laser when operating at low beat frequencies, it is necessary to bias the ring in order to avoid the lock-in region (Killpatrick, 1967). Of the many methods proposed to accomplish this, the least expensive way to avoid lock-in with any utility appears to be to provide a gas flow along the internal beam path. Therefore, a gas flow tube utilizing Brewster angle windows (see Figure 9) was incorporated into one arm of the ring, and provision was made to be able to reverse the flow direction of the gas. The flow rate was determined by using a stop watch to time the interval necessary to pass a given volume of gas as measured by a wet rate meter. The choice of gas was made on the basis of providing a decent bias coupled with requirements for an ultra-dry, inexpensive gas (see Table III). The gas chosen was compressed nitrogen gas. The nitrogen gas flow was controlled by adjusting the compressed gas bottle regulator valve. A desirable flow rate, as indicated by a desirable Δf_B display on the low frequency spectrum analyzer, was chosen for optimizing the Δf_B detection and electronic processing section (see Figure 1). Observation of the amplitude of Δf_B on the spectrum analyzer provided a convenient method for optimizing the adjustment of the optical beam mixer, as well as the proper alignment of the photodetector and its associated amplifiers.

TABLE III

CALCULATED EFFECT OF THE DISPERSION TERM ON THE DRAG COEFFICIENT

Material	n	$dn/d\lambda$ (μ^{-1})	α_1	α_2	$\frac{\alpha_1 - \alpha_2}{\alpha_2} \times 100$
Gases					
Helium	1.000035	-0.07×10^{-6}	0.6974×10^{-4}	0.6978×10^{-4}	0.06%
Oxygen	1.000270	-1.5×10^{-6}	5.398×10^{-4}	5.408×10^{-4}	0.18%
Nitrogen	1.000298	-1.3×10^{-6}	5.966×10^{-4}	5.974×10^{-4}	0.13%
Carbon Dioxide	1.000448	-2.3×10^{-6}	8.953×10^{-4}	8.968×10^{-4}	0.16%
Solid					
Fused Silica	1.4571	-0.0306	0.5290	0.5423	2.50%
Liquids					
Carbon Tetrachloride	1.4619	-0.085	0.5321	0.5689	6.5%
Toluene	1.4951	-0.0623	0.5526	0.5790	4.6%
Benzene	1.4983	-0.0720	0.5546	0.5850	5.2%

The nitrogen gas flow was used early in the experimental stage to study the characteristics of various vacuum photomultipliers and solid state photodetectors and to get the entire Δf_B readout equipment working properly. The measurement of Δf_B vs. flow rate (which is proportional to v_a) for nitrogen gas flow provided a convenient method of checking the sensitivity of the entire beat frequency detection system by measuring the magnitude of the bias produced by terrestial rotation. This measurement was taken by obtaining from 30 to 50 ten second integrations of Δf_B for several different flow velocities. The actual flow velocity along the axis of the tube was not known due to uncertainties in the flow pattern, turbulence, etc.

IV.2. Solids

All measurements on solids were made on a $\lambda/20$ optic finish Homosil fused silica flat obtained from Oriel Optics. The parameter sought in these measurements was the drag coefficient α. However, α had to be calculated from other measurable parameters. Some of these could be determined under static testing while others had to be determined dynamically.

IV.2.1. Static Measurements

The first parameters measured on the optic flat were its physical dimensions. A precision micrometer was used to very carefully determine the thickness of the fused silica disc, care being taken not to harm the optic finish. A series of readings were taken at locations around the periphery of the end surfaces and near the center to determine its thickness. The diameter was also measured and recorded.

The next parameter to be determined was the index of refraction n. Three different methods were tried. The first method was to mount the optic flat on a precision angle rotator and to measure the Brewster angle by reflecting polarized light from the front surface of the optic flat. The set-up is illustrated in Figure 19 where a circularly polarized laser beam is polarized linearly so that when the optic flat is at its Brewster angle no reflection occurs. The second method used the well known relation that sin θ_i = n for total internal reflection, and it was hoped that this relation might be useful. The equipment illustrated in Figure 19 was again used with the exception of the polarizer. The angle θ_i was determined from the precision angle rotator.

A third method was tried for determining n of the optic disc. If a substance is placed internally in a laser cavity and occupies some portion of the oscillating cavity, then the axial mode separation for that cavity will change due to the presence of a different index of refraction n over some length of that internal cavity. The describing equations are derived in Appendix A. The optic flat was placed in the cavity of a 35 mw He-Ne laser of length 191 cm (see Figure 35). The first order axial beat notes were measured for the cavity with and without the flat, and calculations of n were made from this data.

The remainder of the static and dynamic measurements require the insertion of the optic flat into the low gain ring laser cavity. Hence, it is mandatory that the flat be very clean. The flat was always first gently cleaned of any visible particles by a moderate nitrogen gas flow across the surface. Then the surface was wetted evenly with two drops of isopropyl alcohol. A soft, lint-free optic tissue was then used to gently and evenly wipe the alcohol from the surface in one sweeping

motion. This procedure was repeated until no markings could be seen on either surface.

The clean optic flat was then assembled in the bearing and rotator assembly for the remainder of the measurements. In order to achieve optical alignment of the ring with the flat in position, it was necessary to position a second similar flat in the ring to compensate for the beam offset as shown in Figure 15 and photographed in Figure 2. When both optic flats were aligned, the optic path length of the ring L was determined by measuring $\Delta\nu_{axial}$ of either of the contracirculating beams.

The procedure used to measure $\Delta\nu_{axial}$ was to superimpose exactly the $\Delta\nu_{axial}$ signal and a stable, tunable oscillator signal on a high frequency spectrum analyzer (see Figure 18). When the two frequencies are identical, a "zero beat" or null signal appears on the spectrum analyzer in place of the overlaid frequency response curves or a portion thereof. At very small frequency differences, low frequency (< 100 Hz) beats are visually apparent on the mutual portions of the overlaid frequency response curves on the spectrum analyzer. At null, the oscillator frequency is measured directly with an electronic counter. Since frequency pulling can occur, the second and third order axial beat notes were also measured and averaged to reduce any data fluctuations from pulling. The path length L is then given by Eq. (2-21).

Proper alignment of both the rotating platform and the compensator flat was obtained by observing the intensity of the reflected coherent light from the front surfaces of both the test optic flat and the compensator flat. When either the Brewster angle or the normal angle of the flats is adjusted, the intensity of the reflected light will pass through a minimum. Proper alignment of both minima simultaneously

results in almost zero reflection and allows the angles to be set to a tolerance of $\pm$ 0.1 degrees.

Provision was made to adjust the radius R to 0.01 cm accuracy by means of an X-Y vernier movement calibrated in 0.01 cm divisions. Hence, radius measurements were accurate to 0.01 cm $\pm$ origin uncertainty. The origin is best determined by dynamic measurements.

IV.2.2. Dynamic Measurements

The center of the optic flat can be determined in at least three ways. A direct visual observation of the beam spot when the ring is oscillating as the beam is scattered off the front or rear surface of the flat yields very good results. When the flat is rotating at low angular velocities (angular frequency $\approx$ 50 RPM) the scattering centers on the surface give rise to a circular pattern if the beam is directly over the center of rotation. Very small displacements cause quite noticeable changes (unsymmetry) in the pattern. This method was typically used to determine the center. One could also mount a higher power magnifying device over the center of rotation to make this measurement more precise, but the very low intensity of scattered light demands a light collecting magnifier if the magnified scattering centers are to be seen. In either of the above cases the centers of the front and rear surfaces must be found and averaged to yield the center of the flat. To insure beam penetration through the center of the flat, the x-axis and y-axis settings were set to the averaged values obtained from the front and rear surface readings. In operation, it was typically necessary for the beam to penetrate the flat at some off-center value of x. However, the vertical axis setting was retained at the

averaged value for the y-axis center which was obtained from the front and rear surface centers so that the beam front and rear surface penetrations were still equally spaced vertically about the horizontal centerline of the flat.

A second method which will determine only the x-axis (horizontal or parallel to the plane of the ring) center is to adjust the x-axis to the extremes for which oscillation will occur. This method is repeatable to 0.01 cm, i.e. there are no variations in the vernier readings. And a third method of determining the x-axis center is to rotate the flat at constant f_ω and plot Δf_B vs. x-axis vernier setting. To be absolute, the data must be adjusted for any residual bias, such as that due to the earth's rotation. The disadvantage of this method is the stability requirement on f_ω. Hence, this is the least desirable of the three methods.

IV.2.3. Data Accumulation

The value of α is specified by Eq. (2-45) or Eqs. (2-49) once the above parameters are measured and a data plot is accumulated for Δf_B vs. v_a (or Δf_B vs. f_ω). These data plots were obtained two ways. Recall that $v_a = 2\pi f_\omega R$. In one case, the radius R was set to a predetermined value and v_a was varied by changing f_ω in steps with several readings being taken and averaged for each f_ω. The data plots in Figure 27, Figure 29, and Figure 30 are examples of this case. In the other case, f_ω was set to a constant value and R was varied in steps to change v_a. Again, there were several data accumulations per step in R. However, the data points were connected for constant R so that one obtains a family of curves similar to the first case. Examples of curves taken with

f_ω constant are Figure 31 and Figure 32. The data accumulation using these two methods should allow some reduction in the effect of systematic errors.

IV.3. Liquids

The liquids that were studied had to be contained in a special cell that was fabricated to be substituted in the rotator directly for the solid flat and its holder. Since the cell had to be directly in the internal laser cavity, cleanliness was again of the utmost importance. The fused silica windows were originally cleaned by soaking in dilute nitric acid for six days followed by baths in distilled water, acetone, and isopropyl alcohol. Final surface cleaning was again accomplished by wetting each surface evenly with two drops of isopropyl alcohol and wiping off smoothly. The cell body was then washed with acetone and, finally, the cell was assembled.

When placed in the ring, the empty cell caused no apparent reduction in power of the ring laser over the previous case when the fused silica flat was in the ring. Laser action was quite uniform as the position of the cell was varied. One feature that was quite apparent was the narrow "cat's-eye" visual opening through the empty cell.

Next, a sealed bottle of Analytic Reagent grade carbon tetrachloride was opened and about 20 cc poured into a clean flask. A sterile 20 cc pyrex syringe was then used to transfer the carbon tetrachloride from the flask into the cell via a small threaded 2-56 screw hole in the wall of the cell. This fill of liquid was flushed from the cell and syringe, and the process repeated again. The third fill of liquid was retained for use. An identical procedure was used each time the liquid was

changed in the cell.

The second optic flat had to be positioned in the ring as an additional compensator when the liquid filled cell was placed in the rotator. However, oscillation did not take place with any liquid filled cells in the ring. The liquids tried were carbon tetrachloride, benzene, and toluene. Subsequently, each liquid filled cell was taken to the 35 mw linear laser and inserted thereto, always with negative results. In order that suspended particles might be precipitated, each liquid was centrifuged at 4000 RPM for at least 15 minutes.

Visual observation of the output beam of a cw laser (1.0 mw He-Ne) when shined through the liquid filled cell made it quite apparent that there were noticeable scattering losses in the bulk of the liquid. Centrifuging did not alter the amount or nature of the scattering. Surface scattering at the liquid-fused silica interfaces was completely negligible (not even discernible) for the carbon tetrachloride fill where the indices of refraction were quite closely matched. In order to extimate the losses in the liquids, a polarized beam was directed along the usual beam path in the ring through the liquid to a detector (see Figure 20). The results are tabulated in Table XXII.

CHAPTER V

EXPERIMENTAL RESULTS

V.1. Introduction

The primary objective of the measurements taken was to determine the value of the drag coefficient and to compare this value with theoretical models. A less important, but well demonstrated, objective was to measure the frequency bias introduced due to the earth's diurnal rotation. Measurements taken with gas flows served well to evaluate the magnitude of this bias, and, hence, to demonstrate the capabilities of the equipment. Measurements were taken on fused silica to determine the drag coefficient for this specific solid, but drag measurements attempted on liquids were unsuccessful.

V.2. Gas Measurements

To initially align the frequency measuring equipment, a flow of dry, compressed nitrogen gas was introduced along the oscillating beam as illustrated in Figure 1. Two separate data runs were made using a nitrogen gas flow to demonstrate the overall sensitivity of the equipment, to detect the earth's rotation induced bias, and to show the deviation of data during a trial. The results are plotted in Figure 24 and Figure 25. Both figures are for nitrogen gas flowing through a 5.0 mm I.D. tube that is 90 cm long (nominal) with removable Brewster windows

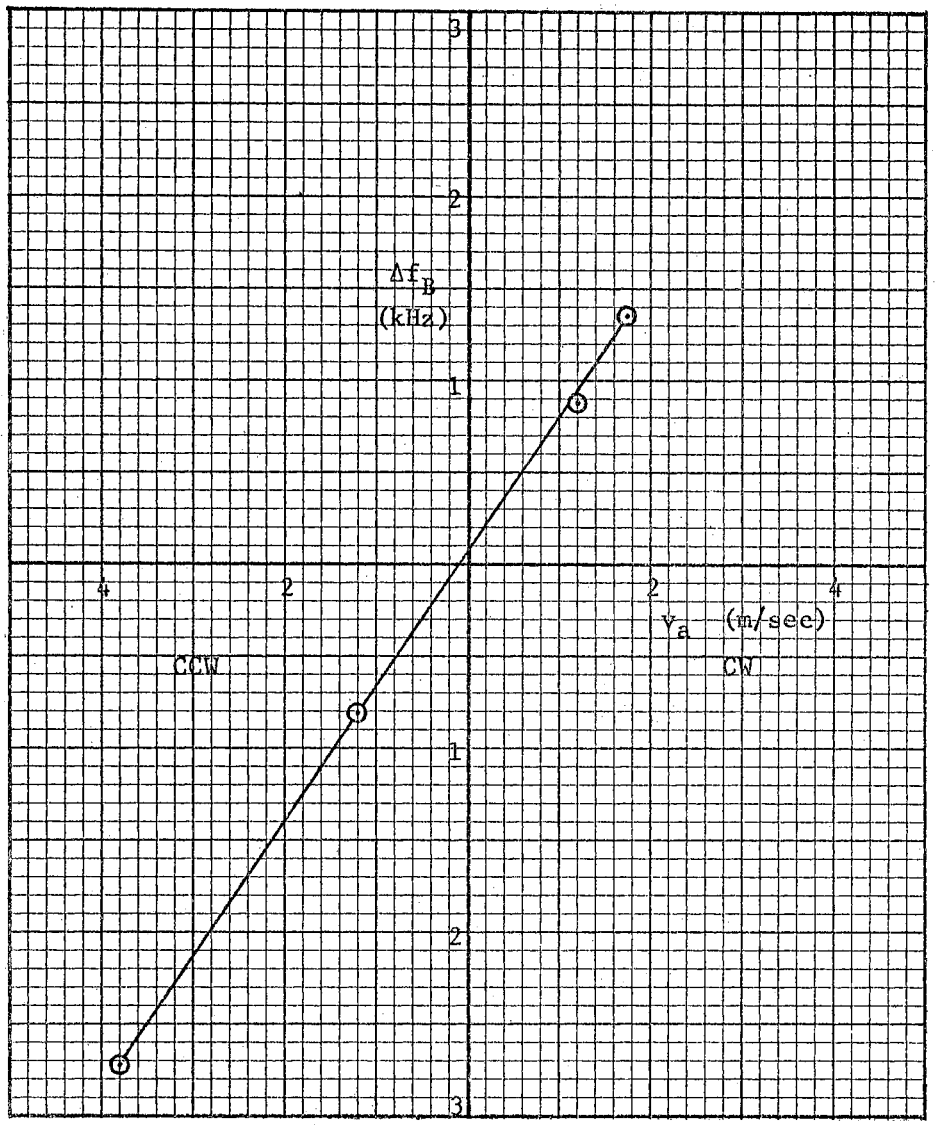

Figure 24. Beat Frequency vs. Velocity for Nitrogen Gas Flow in a 5.0 mm Bore Tube - Trial 1

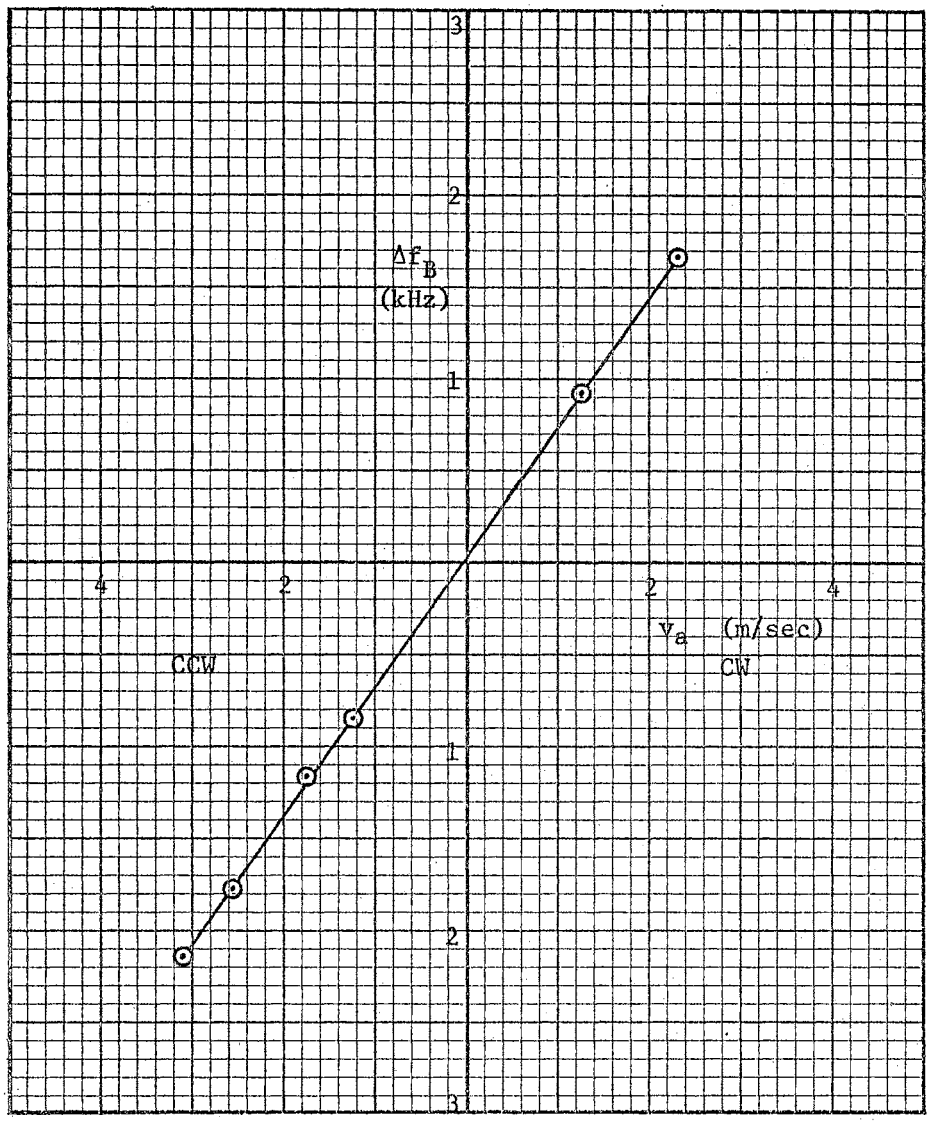

Figure 25. Beat Frequency vs. Velocity for Nitrogen Gas Flow in a 5.0 mm Bore Tube - Trial 2

TABLE IV

TABULAR REPRESENTATION OF FIGURE 24

v_a Observed (cm/sec)	Δf_B Observed (Hz)	Δf_B Calculated (Hz)	DELTA Δf_B (Hz)
- 1.179	- 801.7	- 805.1	3.4
1.207	893.7	922.0	- 28.3
1.768	1352.0	1328.1	23.9
- 3.824	- 2718.6	- 2719.7	10.6

TABLE V

TABULAR REPRESENTATION OF FIGURE 25

v_a Observed (cm/sec)	Δf_B Observed (Hz)	Δf_B Calculated (Hz)	DELTA Δf_B (Hz)
- 3.119	- 2133.3	- 2136.9	3.6
- 2.587	- 1776.4	- 1763.9	- 12.5
2.300	1678.3	1662.7	15.6
1.255	910.3	930.0	- 19.7
- 1.239	- 837.7	- 818.7	- 19.0
- 1.754	- 1147.9	- 1179.8	31.9

fitted against rubber gaskets (see Figure 10). The same type flow measurement was attempted with helium but contamination of the windows occurred very quickly. The exact nature of the contamination is not clear.

Tabulated entries for Figure 24 and Figure 25 are entered in Table IV and Table V, respectively. The data was reduced by computer program as described in Section V.3.2., Dynamic Measurements. The slope of the curve in Figure 24 is m = 724 $\pm$ 6 Hz sec m^{-1} with a y-axis inte rcept due to the earth's rotation of b = 48 $\pm$ 14 Hz. For Figure 25, m = 701 $\pm$ 5 Hz sec m^{-1} and b = 50 $\pm$ 10 Hz. The variation in m between trials indicates that flow conditions were not duplicated closely, while the variation of less than $\pm$ 1% in m during a trial indicates only small deviations within each test situation. No particular effort was made to repeat flow conditions between the two runs. The repeatability of b is quite good between trials, and is also in the range anticipated.

The theoretical value of b can be computed from Eq. (2-27) where $\Omega = 7.3 \times 10^{-5}$ sin(latitude) rad per sec, $A = (\sqrt{3}\, L^2/36)$ for an equilateral triangle, L is obtained from Eq. (2-21) where $\Delta\nu_{axial}$ = 92.021 MHz, and the latitude at which the measurements were taken is 36° 7' N. In terms of the above parameters, Eq. (2-27) then becomes

$$\Delta\nu = \frac{4\sqrt{3}\, c\, \Omega}{36\, \lambda\, \Delta\nu_{axial}} \qquad (5\text{-}1a)$$

which, upon substituting the appropriate values, is

$$\Delta\nu = \frac{4\sqrt{3}\ (2.998\times10^{10}\,\text{cm/sec})\ 4.3\times10^{-5}\,\text{rad/sec}}{36\ \ (6328\ \text{Å})\ \ 92.021\ \text{MHz}} \qquad (5\text{-}1b)$$

or

$$\Delta\nu = 42.6\ \text{Hz}. \qquad (5\text{-}1c)$$

This value should be apparent in all the data presented here. The value of b is not removed from any tabulated or plotted data.

A second gas flow tube with a 7.2 mm I.D. bore was constructed when the 5.0 mm I.D. bore tube was broken. Results with the larger bore tube did not give the straight line results of Figure 24 and Figure 25, but departed symmetrically in a manner that suggested that the velocity along the tube axis was becoming progressively more predominant as the flow rate was reduced, i.e. the beat frequency became progressively larger than expected as the average flow rate was decreased. This could be the result of reduced flow velocities near the bore walls which occur due to surface friction. However, even this data gave a reasonable value for b, i.e. $b = 53 \pm 47$ Hz, and this range of b was maintained for any set of measurements which covered equal values of clockwise and counterclockwise gas flow rates.

V.3. Solid Measurements

All of the measurements taken on solids were obtained from one high quality fused silica optic flat. This optic flat was composed of homogeneous HOMOSIL fused silica and was obtained from Oriel Optics. Measurements taken on the fused silica were used to determine the magnitude of the drag coefficient by computing Eq. (2-45) [ultimately in the form of one of Eqs. (2-49)] using the experimental data. The parameters necessary for computing Eq. (2-45) which can be determined from static measurements are R, d, $\Delta\nu_{axial}$, and n. Other alignment parameters which affect the total precision of the measurements are β (see Figure 13), θ_B (see Figure 12), and θ_n (see Section V.3.1.). Dynamic measurements are necessary to determine the center of rotation of the optic flat and

the value of m [see Eq. (2-46) and Eq. (2-48)] for use in computing Eq. (2-45) [or any of Eqs. (2-49)].

V.3.1. Static Measurements

The velocity of the medium is determined by using the relation expressed in Eq. (2-40). Hence, v_a is directly proportional to R. Using the vernier adjustment on the rotator platform, displacements can be read directly to 0.01 cm. However, at 1000 RPM and R = 2.00 cm, an error of 0.01 cm results in an error in v_a of 0.5% which contributes an error to Δf_B of 100 Hz. The resolution with which R can be reset with the vernier appears to be better than 0.01 cm. Table VI is a tabulation of the results of resetting R to 1.72 cm while f_ω is held constant at 2000 RPM. For each of the ten trials, a set of from ten to twelve 10 second counts of Δf_B were taken from which $\overline{\Delta f_B}$ and $\sigma_{\Delta f_B}$ were determined for each trial. The mean and standard deviation for all the $\overline{\Delta f_B}$ data was then computed and used to calculate DELTA $\overline{\Delta f_B}$, where DELTA $\overline{\Delta f_B}$ = $\overline{\Delta f_B}$(observed) - Δf_B(fitted). A radius change of 0.01 cm under the conditions of this experiment corresponds to a DELTA $\overline{\Delta f_B}$ of 200 Hz, so it can be seen that typically the radius was reset to about ΔR = 0.005 cm or less. Note that in the above discussion Δf_B(fitted) = $\overline{(\overline{\Delta f_B})}$.

The thickness of the optic flat is indicated as d. This value was determined by direct measurement using a 0-1 inch precision micrometer which has a vernier readout to 0.0001 inch accuracy. Thickness measurements were taken at four evenly spaced points around the periphery of the flat and at the center. Five readings were taken at each point. In all twenty-five cases, the reading was repeated to within the reading accuracy of the vernier, i.e. 0.00005 inch. The value of d for the ro-

tated optic flat was thus determined to be 0.50285 inches which can be converted to 1.2772 cm.

TABLE VI

STATISTICAL RESULTS OF RESETTING RADIUS TO 1.72 CM UNDER CONTROLLED CONDITIONS

Trial Number	Number of Data Points	$\overline{\Delta f_B}$ (Hz)	$\sigma_{\overline{\Delta f_B}}$ (Hz)	DELTA $\overline{\Delta f_B}$ (Hz)
1	12	34856	13	89
2	10	34830	22	63
3	11	34830	19	63
4	10	34758	16	- 9
5	10	34780	14	13
6	10	34781	20	14
7	10	34768	23	1
8	10	34689	19	- 78
9	10	34667	22	-100
10	10	34713	26	- 54
	$\overline{(\Delta f_B)}$ = 34767 Hz		$\sigma_{\overline{(\Delta f_B)}}$ = 63 Hz	

The above measurement procedure was repeated on the compensator flat and the two thinner fused silica windows for the liquid cell. The result of the averaged measurements for the compensator flat was a thickness of 0.48656 inches and for the two thinner windows the measurements yielded thicknesses of 0.25064 inches and 0.24967 inches. The diameter of all four optic flats was nominally 2.00 inches.

The axial mode separation $\Delta\nu_{axial}$ was measured directly from the

output laser beam. For the ring laser, this was accomplished by blocking one of the beams in the optic mixer and taking measurements on the other beam. The output beam from a laser operating in the multi-valued q TEM_{ooq} mode consists of frequencies $\nu \pm N\,\Delta\nu$, where N is an integer ranging from zero to as high as ten or fifteen. Hence, on a detector that mixes these frequencies, the $\Delta\nu$ are the axial mode separation frequencies characteristic of any particular laser cavity. The value of N corresponds to one less than the number of discrete frequencies which have a sufficient gain for oscillation in the Doppler broadened profile.

The axial mode separation determined by the above method yielded 92.021 MHz with a standard deviation of less than 1.0 kHz (see Appendix B). The 1.0 kHz standard deviation results from frequency fluctuations of the separate axial modes caused by both vibrations of the ring laser and inconsistent mode pulling. Hence, the resulting beat between axial modes will fluctuate. This data contributes less than a 0.01% error in determining α.

The index of refraction n was not as easily determined as the other static parameters. In order that the contributed error due to uncertainty in n be less than 0.01%, it is necessary that the absolute value of n be known to an accuracy of $\pm$ 0.0001. Three separate schemes were tried to attempt determination of n to sufficient accuracy.

The first method was to employ the phenomenon of zero reflectance of plane polarized light at the Brewster angle θ_B for the material so that n can be determined from the relation

$$n = \tan \theta_B. \qquad (5\text{-}2)$$

In order for this method to determine n with an accuracy of

± 0.0001, it is necessary to be able to determine θ_B to within ± 0.0027 degrees. The experimental setup is depicted in Figure 20 where the circularly polarized light of a He-Ne laser operating at 6328 Å was plane polarized by passing it through a single polaroid material. The optic flat was secured on a precision angle rotator which had an angular readout accurate to 0.1 degree. Initial alignment of the rotator for zero rotation was set by reflecting the beam off the optic flat directly back on itself. The rotator and flat were then rotated to the Brewster angle which was determined by observing a minimum (effectively zero) reflection on the white screen. In practice, this angle could only be determined to ± 0.1 degree accuracy due to the "broad" zero reflection band as the flat was rotated. For this same reason, triangulation would be of no additional benefit in determining the angles involved.

A second method of determining n was to utilize the relation of the critical angle of reflection as a function of the index of refraction, i.e.

$$n = (\sin \theta_i)^{-1}. \tag{5-3}$$

However, the necessary accuracy on n requires an angular accuracy of ± 0.0054 degrees, and in practice, the method was limited to about ± 0.1 degree accuracy.

The third method involved inserting the optic flat internally into a linear laser cavity (see Figure 36) and measuring the change in axial mode separation due to the medium. The pertinent equations are derived in Appendix A. Since the measured values are on the order of 10^8 Hz and their standard deviation is about 10^3 Hz (see Appendix B), it ap-

pears that very precise measurements should be possible. However, as indicated in Eq. (A-10), the value of (n-1) is proportional to the change in axial mode separation. Since this change is on the order of 10^5 Hz, the standard deviation of 10^3 Hz only allows an accuracy of $\pm$ 0.01 in (n-1). Furthermore, if only low order mode separations are used, the effects of line pulling and pushing can cause appreciable errors (McFarlane, 1964). For example, if the average value of the normalized mean of the mode separation is used to calculate n from the data in Appendix C, one obtains n = 1.469 $\pm$ 0.010, while if $\Delta\nu_{ae4}$ is used the calculated value of n is n = 1.460 $\pm$ 0.010. The range of the former value does not even include the manufacturer's specified value (see Table VII), while the latter value substantiates n quite well, i.e. n = 1.460 $\pm$ 0.010 vs. n = 1.4571. The mode separation $\Delta\nu_{ae4}$ should be unaffected by line pulling since it is the beat between axial modes which are far removed from line center where the pulling occurs (McFarlane, 1964).

Since all three methods failed to give satisfactory results, the value of the index of refraction as specified by the original manufacturer of the HOMOSIL fused silica was obtained and recorded in Table VII. All subsequent calculations and results utilize the manufacturer's specified value of the index of refraction.

The alignment parameters which affect the measurements are associated with the angles which determine v_a and θ_B. The component of velocity of the medium parallel with the beam is a function of both the angle β (see Figure 13) and, indirectly, θ_B (see Figure 12) since by Snell's law

$$\sin \theta_B = n \sin \theta_t \, . \qquad (5\text{-}4)$$

TABLE VII

MEASUREMENT ERRORS

Parameter	Measurement Limitation	Typical Std. Deviation	Typical Data Mean	Percent Error ($\frac{\text{Std. Dev.}}{\text{Mean}} \times 100$)
f_ω (RPM)	0.1 RPM	0.1-0.5 RPM	500-2500 RPM	0.02
Δf_B (kHz)	0.1 Hz	10 Hz	1-50 kHz	0.05[1]
R	0.01 cm	0.005 cm	0.5-2.0 cm	0.5[2]
L_r (in.)	0.0001 in.	0.00005 in.	0.5 in.	0.01
$\Delta\nu_{axial}$ (MHz)	1 Hz	3 kHz	92 MHz	0.03
n^3 (mfg. data)	0.00001	< 0.0001	1.4571	< 0.007
λ^4 (Å)	< 0.01 Å	-	6328.15 Å	< 0.0002
c^5 (cm/sec)	< 10^5 cm/sec	-	2.997929 x 10^{10} cm/sec	< 0.003

[1]For f_ω = 1000 RPM and R = 2.0 cm.

[2]For R = 2.0 cm.

[3]Amersyl Corporation.

[4]International Critical Tables, Vol. V, (New York, 1925), p. 306.

[5]E. Condon and H. Odishaw, Handbook of Physics, (New York, 1958), pp. 7-11.

The angle β will cause an error in the velocity component parallel with the beam by a factor $(1 - \cos \beta)$. The angle β was determined experimentally as follows. The x-axis vernier on the rotator platform was adjusted so the oscillating beam passed through the optic flat near a vertical center but was displaced horizontally off-center toward one edge of the optic flat. The y-axis vernier was then moved up and down so the maximum vertical excursions over which oscillation could be maintained were determined. A series of five measurements was taken (see Table VIII). The vernier readings were repeated exactly on each measurement to within the readout capability of 0.1 mm. The x-axis vernier was then adjusted so the beam penetrated the optic flat near the opposite edge and the measurements were repeated. The y-axis vernier mean for one set of data was 122.8 mm while across the flat a value of 122.75 mm was obtained. The x-axis separation was 42.0 mm. Hence, β can be calculated as

$$\tan \beta = \frac{0.05 \text{ mm}}{42.0 \text{ mm}} \tag{5-5}$$

so that $\beta < 5$ minutes. Hence, $\cos \beta > 0.99999$ so that the velocity is in error by less than 0.001%. Thus, the error in β contributes a negligibly small error to the data in these experiments.

As shown in Figure 12, the angle θ_B, through its interrelation with θ_t, also affects the velocity component parallel to the beam. Both θ_B and θ_n are determined by minimizing the front surface reflection off the optic flat onto a white background located above the optic flat. The angle θ_n is the angle between a normal to the face of the optic flat and a line which is both in the plane of the ring and perpendicular to the beam. Ideally, θ_n should be 90 degrees. Both θ_B and θ_n

are adjusted to within ± 0.1 degree by the above method. The velocity error, which is proportional to the cosine of the angle, is less than 0.2% for θ_B and less than 0.001% for θ_n.

TABLE VIII

DATA FOR DETERMINING X-AXIS VERNIER MISORIENTATION ANGLE β

X-Axis Set Point (mm)	Y-Axis Max. (mm)	Y-Axis Min. (mm)	Y-Axis Mean (mm)
5.5	120.4	125.1	122.75
5.5	120.4	125.1	122.75
5.5	120.4	125.1	122.75
5.5	120.4	125.1	122.75
5.5	120.4	125.1	122.75
47.5	119.5	126.1	122.8
47.5	119.5	126.1	122.8
47.5	119.5	126.1	122.8
47.5	119.5	126.1	122.8
47.5	119.5	126.1	122.8

V.3.2. Dynamic Measurements

The center of rotation of the optic flat must be determined quite accurately in order that the radius R be accurate. The most precise method of determining the center of rotation is to visually observe the rotation of small scattering centers on the front and rear surfaces of the optic flat (see Section IV.2.2.). A series of measurements utiliz-

ing this method is tabulated in Table IX. The standard deviation of the settings is from 0.05 mm to 0.08 mm, so the resulting error in R for a 2.00 cm radius is about 0.3%.

TABLE IX

REPEATIBILITY DATA FOR DETERMINING THE CENTER OF THE FUSED SILICA OPTIC FLAT

Front Surface		Rear Surface	
X-Vernier (mm)	Y-Vernier (mm)	X-Vernier (mm)	Y-Vernier (mm)
26.6	121.4	26.5	130.0
26.5	121.4	26.6	130.0
26.5	121.4	26.5	130.1
26.6	121.4	26.5	130.1
26.6	121.2	26.6	130.1
26.4	121.2	26.6	130.1
26.5	121.3	26.5	130.1
26.5	121.3	26.6	130.0
26.5	121.3	26.5	130.2
26.6	121.4	26.6	130.1
$\bar{x}$ = 26.53	$\bar{y}$ = 121.33	$\bar{x}$ = 26.55	$\bar{y}$ = 130.08

The primary dynamic measurements in these experiments involve determining the relationship of the beat frequency and the velocity of a moving medium. These measurements are primarily a determination of Δf_B vs. v_a for dynamic conditions. Each data point plotted in the figures

which follow represents the mean of a set of ten to fifty data points accumulated for the specific conditions represented. For example, the raw data in Table X was used to obtain the coordinates of one data point. The twenty seven points of data acquired were taken consecutively under the same conditions and averaged to give a value for these conditions. The resulting averaged values represent one point on a plotted curve. Specifically, Table X represents the point on Figure 29 with R = 2.00 cm, f_ω = -1002 RPM (minus corresponds to counterclockwise), and Δf_B = -20286 Hz. The random variations of the raw data in Table X are representative of all of the data accumulated. The standard deviation of f_ω amounts to approximately 0.01% of f_ω and the standard deviation of Δf_B is less than 0.03% of Δf_B. Hence, the errors contributed by data randomness are negligible.

In order that the statistics of normal distributions may be freely applied to the data presented in this work, it is necessary to show that the data distribution approaches a normal distribution. Figure 26 illustrates the distribution of the deviation of 394 individual raw data points from the arithmetic mean of the corresponding plotted data points. These 394 individual data points were the raw data used to obtain the eleven point curve for R = 2.00 cm in Figure 29. The number of occurrences of raw data points whose deviations fall within 0.1 standardized deviate limits are plotted against the standardized deviate, and the normal distribution curve is overlaid on the plotted data. The total number and corresponding fraction of the points which fall within integral values of the standardized deviate are tabulated in Table XI. The agreement between the fraction of total points included and the fraction in a normal distribution substantiates the use of the

TABLE X

RAW DATA FOR A TYPICAL[1] DATA POINT (f_ω, Δf_B)

f_ω (RPM)	Δf_B (Hz)
$\overline{f_\omega}$ = 1002.3 ± 0.02 RPM σ = 0.12 RPM	$\overline{\Delta f_B}$ = 20286 ± 1 Hz σ = 6.8 Hz
1002.5	20290.0
1002.2	20287.6
1002.2	20276.9
1002.1	20279.3
1002.1	20291.4
1002.2	20286.0
1002.3	20284.1
1002.4	20277.3
1002.2	20270.9
1002.3	20286.4
1002.3	20275.0
1002.3	20275.6
1002.4	20292.0
1002.3	20283.9
1002.4	20292.6
1002.5	20284.7
1002.6	20285.7
1002.3	20297.0
1002.3	20282.5
1002.2	20292.6
1002.4	20292.4
1002.4	20289.8
1002.4	20280.0
1002.4	20282.7
1002.4	20294.6
1002.3	20288.8
1002.4	20292.4

[1]The data in this table was taken with R = 2.00 cm and f_ω = 1000 RPM for fused silica.

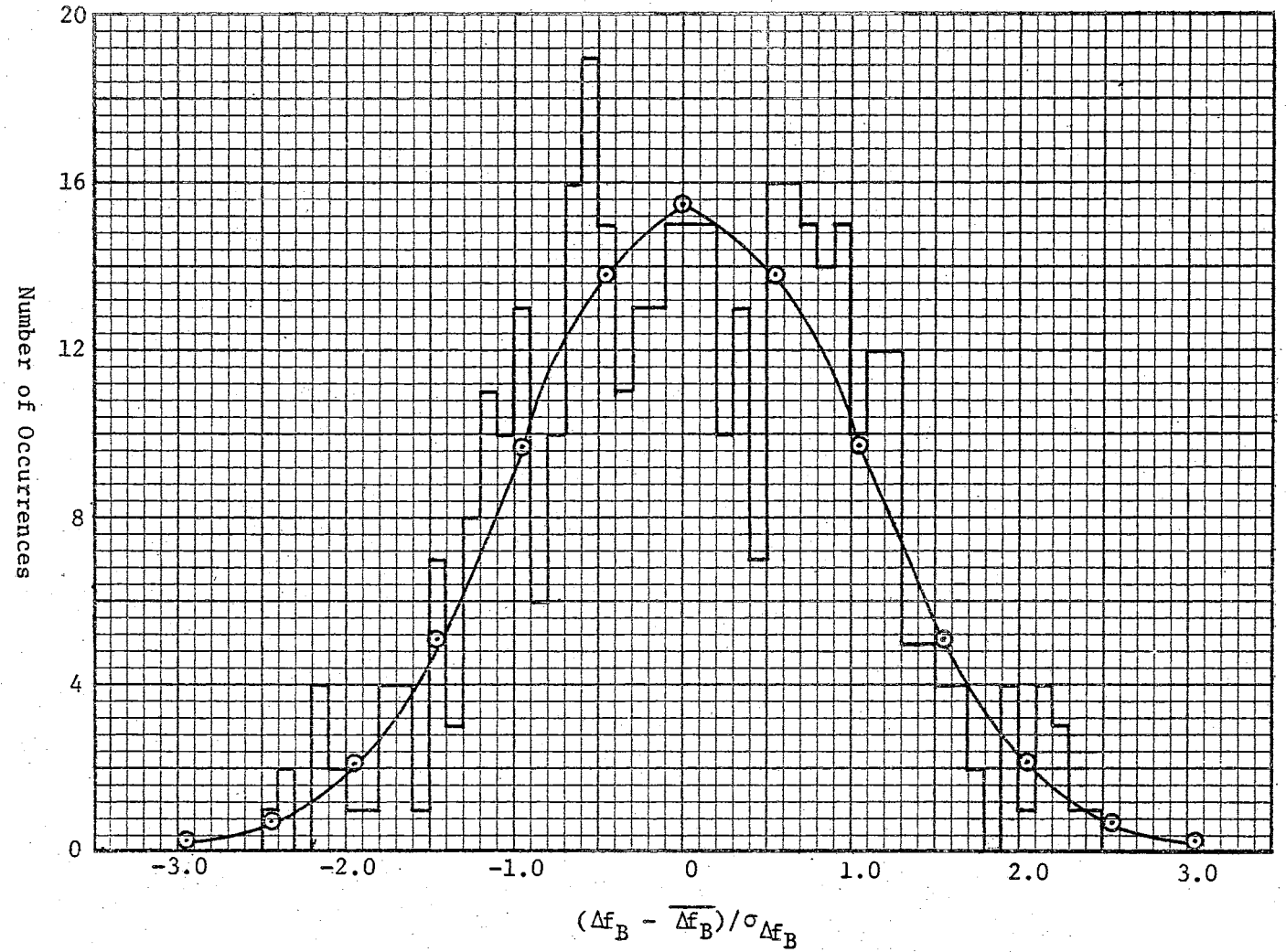

Figure 26. Distribution of Individual Data Points for R = 2.00 cm in Figure 29 - Standardized Deviate

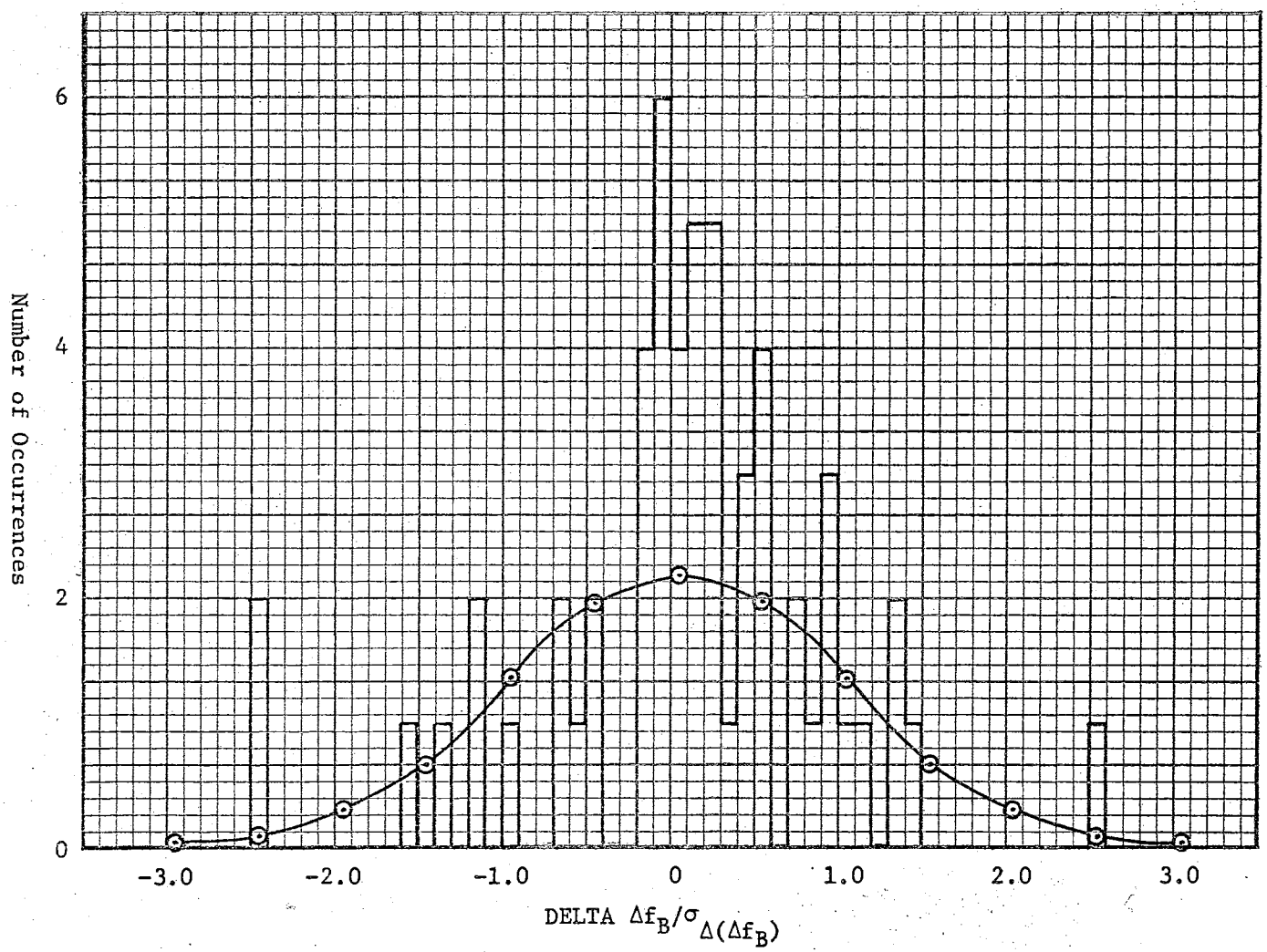

Figure 27. Distribution of DELTA $\Delta f_B/\sigma_{\Delta(\Delta f_B)}$ Data From Table XVI and Table XVII - Standardized Deviate

TABLE XI

DISTRIBUTION OF INDIVIDUAL DATA POINTS
OF A REPRESENTATIVE DATA COLLECTION

Standardized Deviate	Number of Points Included	Fraction of Total Points	Fraction in a Normal Distribution
1	266	0.675	0.683
2	375	0.952	0.955
3	394	1.000	0.993

TABLE XII

DISTRIBUTION OF DELTA $\Delta f_B/\sigma_{\Delta(\Delta f_B)}$ DATA FOR A
TYPICAL LEAST SQUARES FIT

Standardized Deviate	Number of Points Included	Fraction of Total Points	Fraction in a Normal Distribution
1	44	0.79	0.683
2	53	0.95	0.955
3	56	1.00	0.993

statistics for normal distributions on this data. In a similar manner, the distribution of the deviation of fifty six plotted data points from the linear least squares fitted line to the data is plotted against the standardized deviate in Figure 27. The data points used are those listed in Table XVI and Table XVII. Again, the curve of a corresponding normal distribution is overlaid for comparison. A statistical comparison is presented in Table XII where again the agreement of the data to a normal distribution is adequate to allow the use of the statistics of a normal distribution.

As shown in Eq. (2-40) and previously discussed, v_a is a function of both R and f_ω (recall $\omega = 2\pi f_\omega$). To obtain the desired information v_a must be varied. Therefore, to reduce systematic errors, data was obtained for variable v_a by first fixing R and varying f_ω and secondly fixing f_ω and varying R. Data obtained by the former method is plotted in Figure 28, Figure 29, Figure 30, and Figure 31. The plotted data is tabulated in Table XIII, Table XIV, Table XV, and Table XVI, respectively. The latter method was used to obtain the data plotted in Figure 32, Figure 33, and Figure 34. This plotted data is tabulated in Table XVII and Table XVIII, respectively.

To obtain the data in Figure 28 and Figure 29, Δf_B data was taken for R set to 1.00 cm and 2.00 cm. The data in Table XIII shows large variations. These are primarily due to vibrations of the rotator at and above 5000 RPM. The data up to and including 2500 RPM is much better than above 2500 RPM. For that reason, all subsequent data acquisition was limited to values of f_ω not greater than 2500 RPM. Figure 29 is an enlargement of the central portion of Figure 28 and contains additional data points not plotted in Figure 28. This data shows much

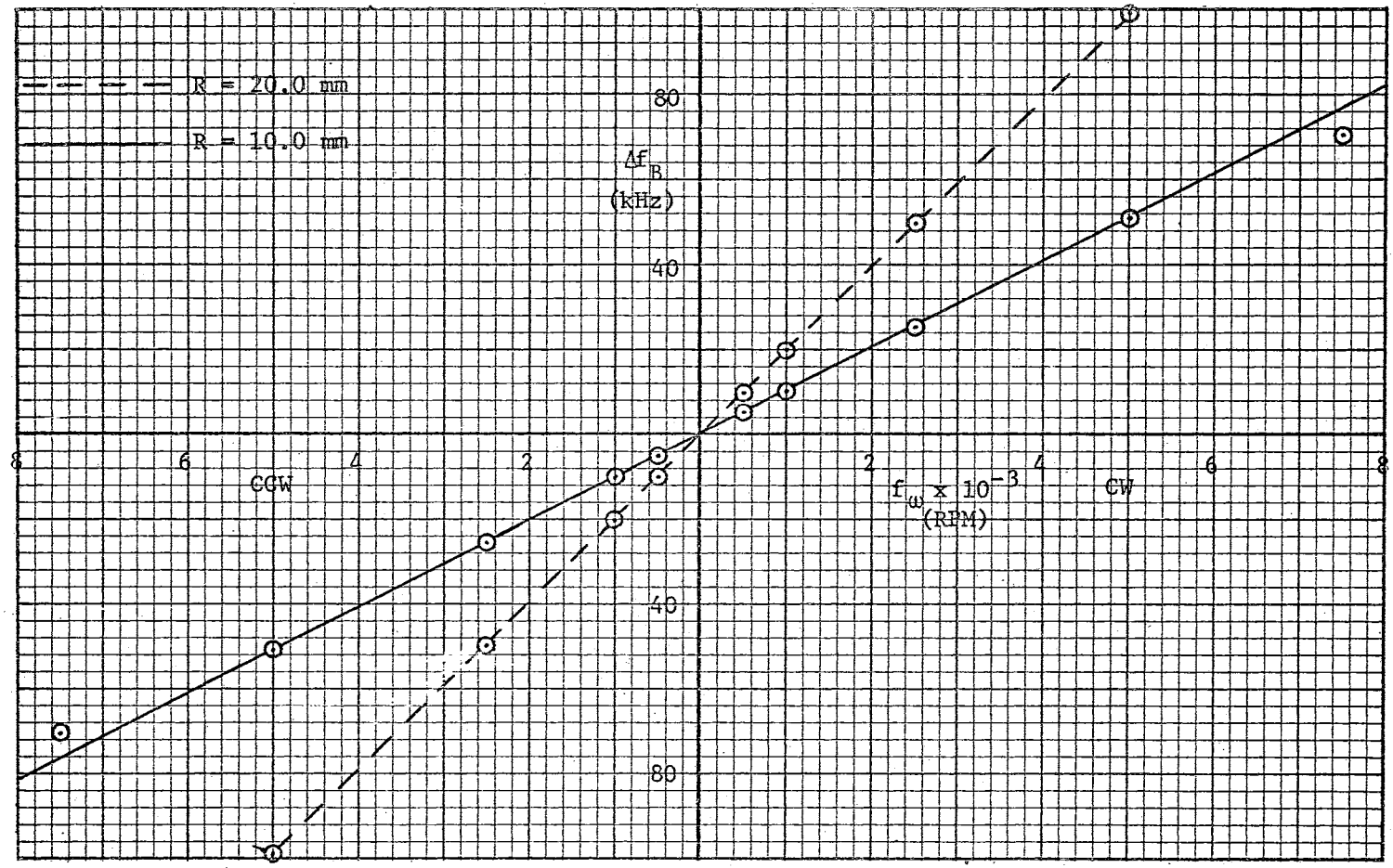

Figure 28. Beat Frequency vs. Frequency of Rotation for Fused Silica for Constant Radius and Variable Frequency of Rotation

TABLE XIII

TABULAR REPRESENTATION OF FIGURE 28

f_ω Observed (RPM)	Δf_B Observed (Hz)	Δf_B Calculated (Hz)	DELTA Δf_B (Hz)
R = 1.00 cm			
-7482	-70666	-72785	2119
-4976	-51316	-48421	-2895
-2502	-25608	-24369	-1239
- 998	-10176	- 9747	- 429
- 500	- 5062	- 4905	- 157
499	5136	4807	329
998	10254	9659	595
2500	25612	24261	1351
4943	51460	48013	3447
7480	69558	72678	-3120
R = 2.00 cm			
-5007	-98469	-99629	1160
-2500	-50215	-49521	- 694
-1000	-20061	-19539	- 522
- 499	-10107	- 9526	- 581
499	10187	10422	- 235
1000	20321	20436	- 115
2502	51035	50457	578
5004	100874	100465	409

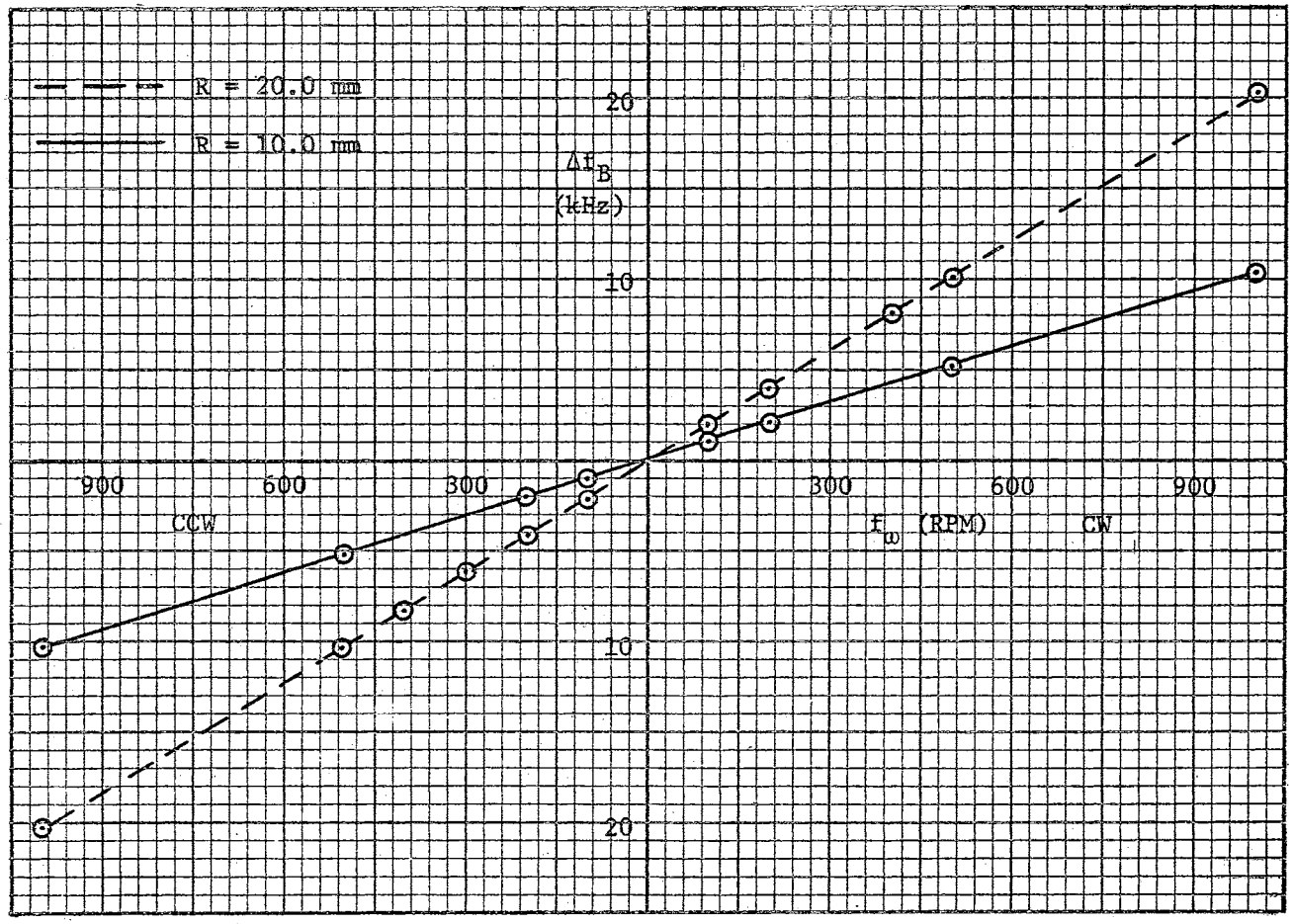

Figure 29. Beat Frequency vs. Frequency of Rotation for Fused Silica for Constant Radius and Variable Frequency of Rotation for Frequency of Rotation ≤ 1000 RPM

TABLE XIV

TABULAR REPRESENTATION OF FIGURE 29

f_ω Observed (RPM)	Δf_B Observed (Hz)	Δf_B Calculated (Hz)	DELTA Δf_B (Hz)
R = 1.00 cm			
- 998	-10176	-10198	22
- 500	- 5062	- 5099	37
- 198	- 1972	- 2006	34
- 101	- 1217	- 1013	-204
102	1149	1066	83
200	2079	2069	10
499	5136	5131	5
998	10254	10241	13
R = 2.00 cm			
-1002	-20286	-20287	1
- 499	-10107	-10080	- 27
- 399	- 8063	- 8051	- 12
- 300	- 6031	- 6042	11
- 201	- 4029	- 4033	4
- 100	- 1941	- 1984	43
100	2045	2075	- 30
200	4113	4104	9
400	8166	8163	3
499	10187	10172	15
1000	20321	20338	- 17

less variation between the observed beat frequency and the beat frequency calculated from a linear least squares fit to the data (see Table XIV).

Figure 30 is a plot of the data obtained as above except with R = 1.81 cm. Data acquisition was restricted to $f_\omega < 2500$ RPM with the result that the greatest DELTA Δf_B is less than 0.7% of the corresponding Δf_B (see Table XV). The abscissas of all of the data points from Figure 28, Figure 29, and Figure 30 for $f_\omega < 2500$ RPM were converted from f_ω to v_a, and the corresponding data points are plotted in Figure 31 and tabulated in Table XVI.

The data obtained by varying R while holding f_ω constant is plotted in Figure 32, Figure 33, and Figure 34 and tabulated in Table XVII and Table XVIII, respectively. The data in Figure 32 was obtained by setting f_ω at some value, and then recording Δf_B for radii of 5.0mm, 10.0 mm, 15.0 mm, and 20.0 mm. This process generates one vertical row of data points. Only clockwise rotations of the medium were used. Hence, all data points lie in one quadrant. After all of the data was plotted, the points were connected in families of constant R for comparison with the other data and to obtain the slope m of Δf_B vs. f_ω. The calculated DELTA Δf_B data (see Table XVII) has a mixiumum value of less than 1% of Δf_B, and is typically much less than 0.5% of Δf_B.

Figure 33 is a plot of the data of Figure 32 where the abscissa is now the component of the velocity of the medium which is parallel to the beam. Again, DELTA Δf_B data shows typical variations of less than 0.5% of Δf_B (see Table XVIII). These variations are quite small considering that the radius, which has the largest percentage variation in repeatability, was reset before the data for each plotted point was ob-

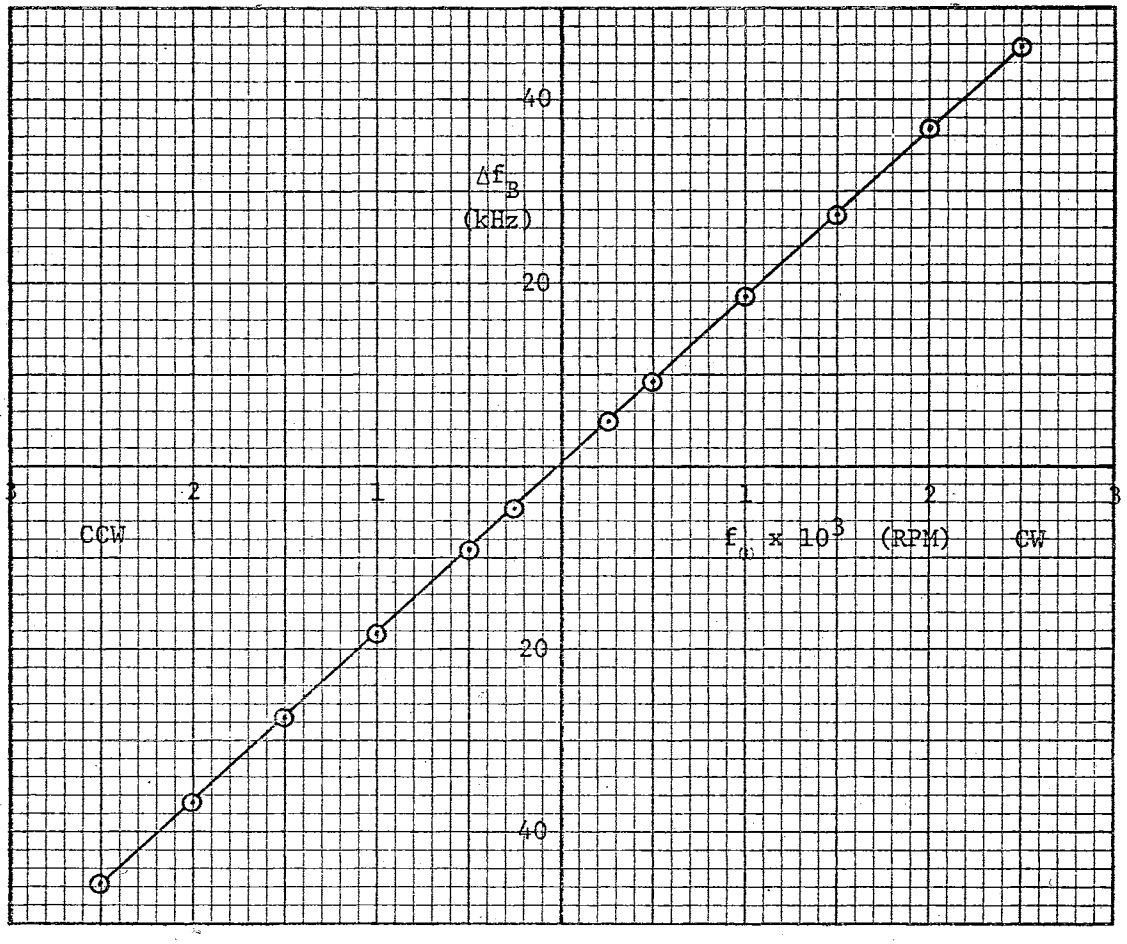

Figure 30. Beat Frequency vs. Frequency of Rotation for Fused Silica for R = 18.1 mm

TABLE XV

TABULAR REPRESENTATION OF FIGURE 30

f_ω Observed (RPM)	Δf_B Observed (Hz)	Δf_B Calculated (Hz)	DELTA Δf_B (Hz)
-2499.1	-45732	-45742	10
-2000.0	-36529	-36595	66
-1498.4	-27591	-27404	-187
- 999.4	-18204	-18260	56
- 498.5	- 9054	- 9081	27
- 249.5	- 4487	- 4518	31
250.4	4607	4643	- 36
499.4	9221	9206	15
996.9	18332	18322	10
1498.7	27618	27518	100
2000.0	36651	36703	- 52
2499.3	45814	45854	- 40

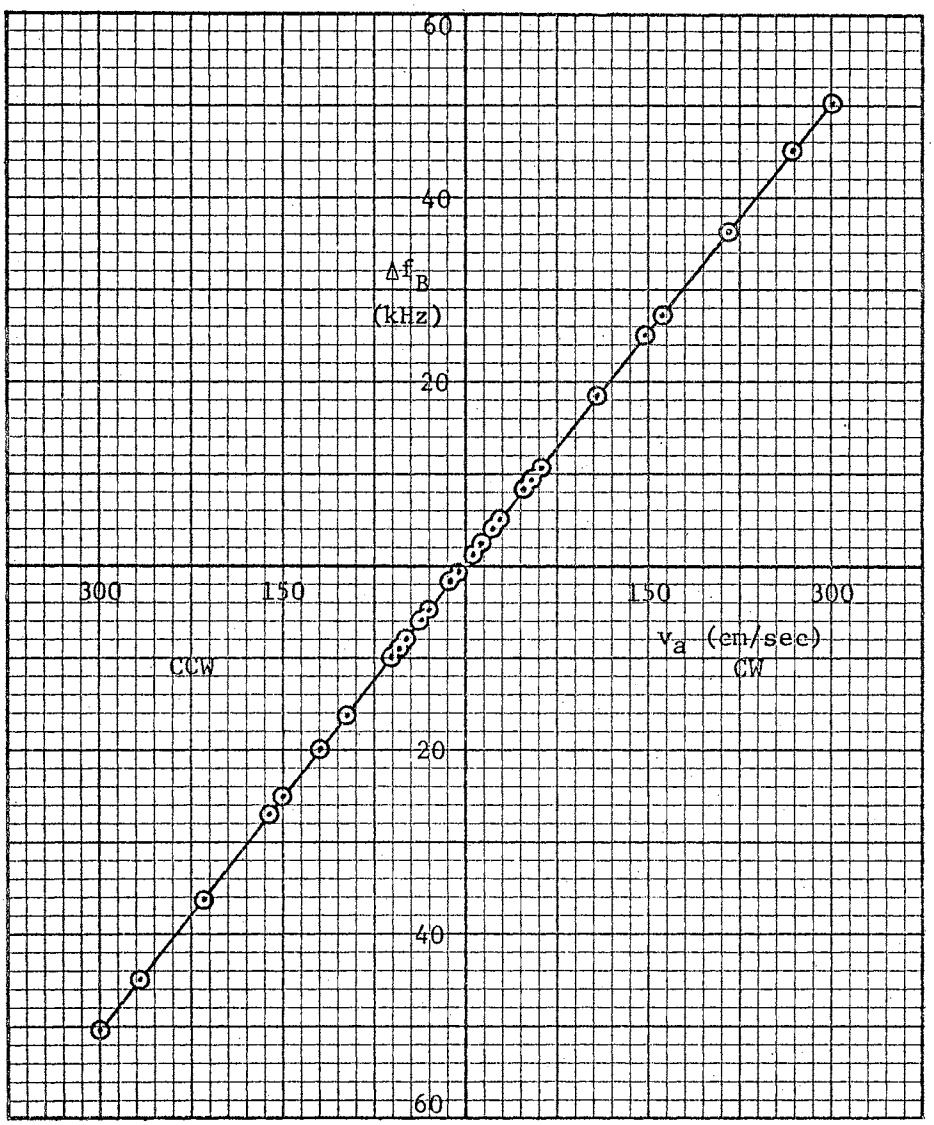

Figure 31. Beat Frequency vs. Velocity for Fused Silica With Data Taken for Variable Frequency of Rotation and Constant Radius

TABLE XVI

TABULAR REPRESENTATION OF FIGURE 31

v_a Observed (cm/sec)	Δf_B Observed (Hz)	Δf_B Calculated (Hz)	DELTA Δf_B (Hz)
-296.3	-50215	-50639	424
-268.0	-45732	-45810	78
-214.5	-36529	-36651	122
-160.7	-27591	-27448	-143
-148.3	-25608	-25319	-289
-118.8	-20286	-20276	- 10
-118.5	-20321	-20234	- 13
-118.5	-20061	-20220	159
-107.2	-18204	-18292	88
- 59.2	-10107	-10081	- 26
- 59.1	-10176	-10068	-108
- 53.5	- 9054	- 9102	48
- 47.3	- 8063	- 8048	- 15
- 35.5	- 6031	- 6028	- 3
- 29.6	- 5062	- 5025	- 37
- 26.8	- 4487	- 4533	46
- 23.8	- 4029	- 4033	4
- 11.8	- 1941	- 1977	36
- 11.7	- 1972	- 1962	- 10
- 6.0	- 1217	- 979	-238
6.0	1149	1077	- 72
11.8	2079	2068	11
11.9	2045	2078	- 33
23.7	4113	4103	10
23.8	4128	4124	4
26.9	4607	4640	- 33
29.6	5136	5106	30
47.4	8166	8151	15
53.6	9221	9208	13
59.1	10254	10164	90
59.2	10187	10168	19
106.9	18332	18336	- 4
148.1	25612	25386	226
160.7	27618	27544	74
214.5	36651	36741	- 90
268.1	45814	45903	- 89
296.5	51035	50678	-357

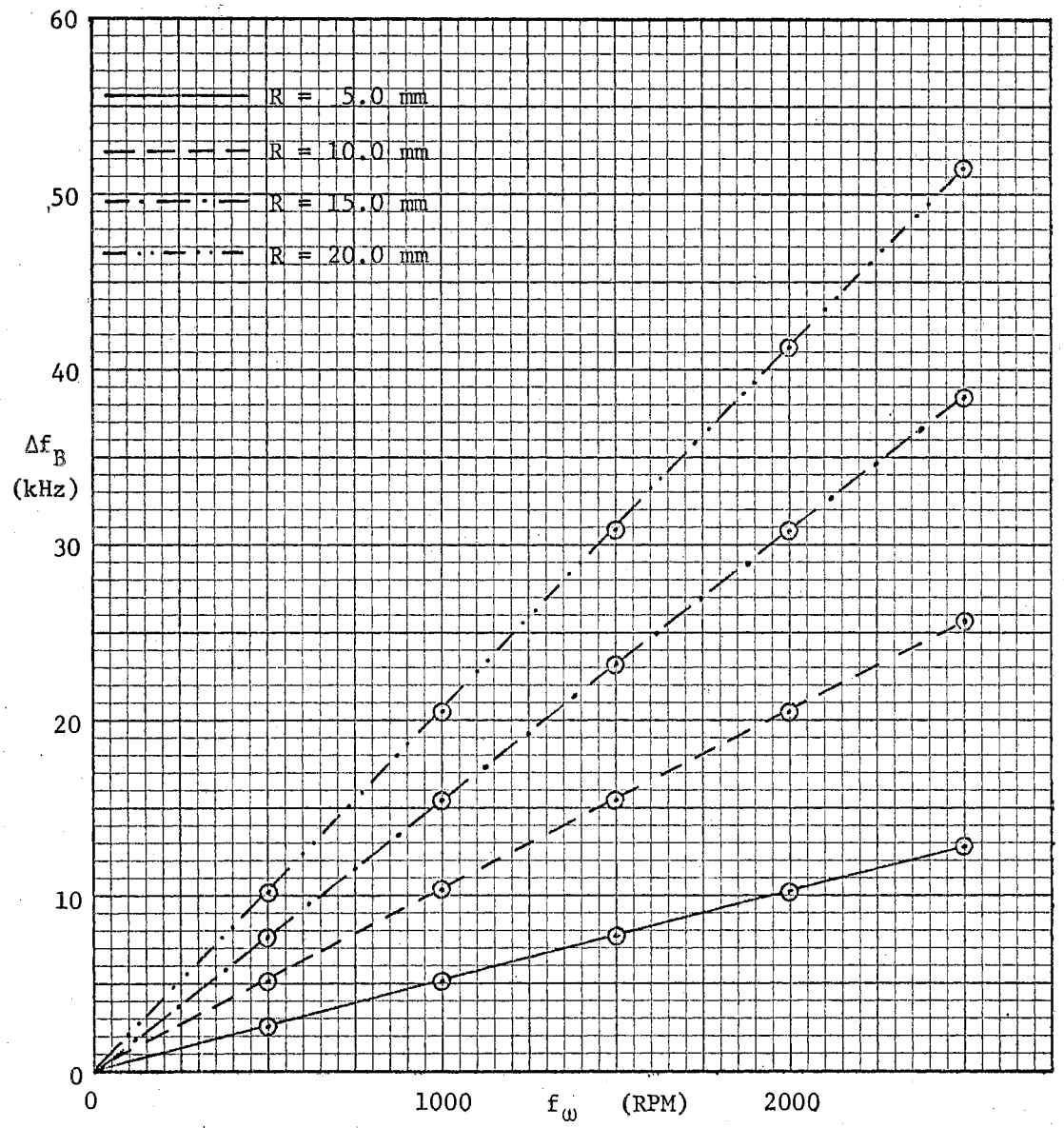

Figure 32. Beat Frequency vs. Frequency of Rotation for Fused Silica With Data Taken for Variable Radius and Constant Frequency of Rotation

TABLE XVII

TABULAR REPRESENTATION OF FIGURE 32

R (cm)	f_ω Observed (RPM)	Δf_B Observed (Hz)	Δf_B Calculated (Hz)	DELTA Δf_B (Hz)
0.50	501.3	2575	2600	- 25
0.50	1000.9	5171	5163	8
0.50	1497.7	7729	7712	17
0.50	1997.0	10318	10276	42
0.50	2499.0	12807	12849	- 42
1.00	501.3	5174	5174	0
1.00	1000.1	10300	10289	11
1.00	1499.7	15389	15412	- 23
1.00	1996.3	20518	20504	14
1.00	2498.9	25657	25659	- 2
1.50	505.2	7706	7756	- 50
1.50	1000.3	15406	15371	35
1.50	1499.1	23066	23044	22
1.50	1996.6	30748	30696	52
1.50	2499.9	38379	38438	- 59
2.00	501.4	10283	10293	- 10
2.00	1000.1	20599	20543	56
2.00	1499.2	30743	30802	- 59
2.00	1997.1	41027	41035	- 8
2.00	2500.5	51402	51381	21

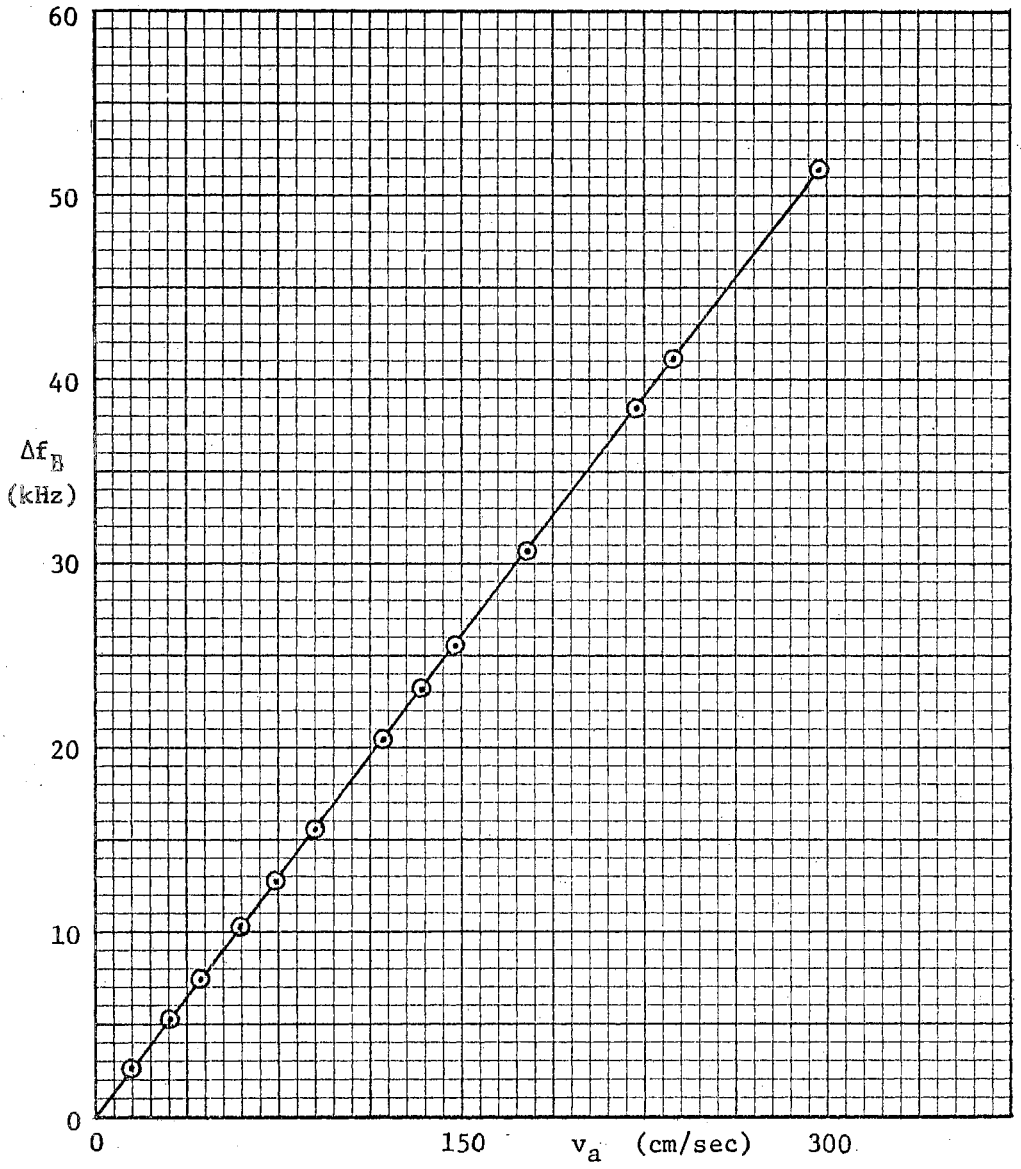

Figure 33. Beat Frequency vs. Velocity for Fused Silica With Data Taken for Constant Frequency of Rotation and Variable Radius

TABLE XVIII

TABULAR REPRESENTATION OF FIGURE 33

v_a Observed (cm/sec)	Δf_B Observed (Hz)	Δf_B Calculated (Hz)	DELTA Δf_B (Hz)
14.9	2575	2584	- 9
29.7	5171	5147	24
29.7	5174	5157	17
44.4	7729	7697	32
44.9	7706	7788	- 82
59.2	10318	10261	57
59.3	10300	10275	25
59.4	10283	10304	- 21
74.0	12807	12835	- 28
88.9	15389	15402	- 13
88.9	15406	15409	- 3
118.3	20518	20498	20
118.5	20599	20538	61
133.2	23065	23088	- 23
148.1	25657	25657	0
177.5	30748	30746	2
177.7	30743	30783	- 40
222.2	38379	38494	-115
236,7	41027	41002	25
296.3	51402	51332	70

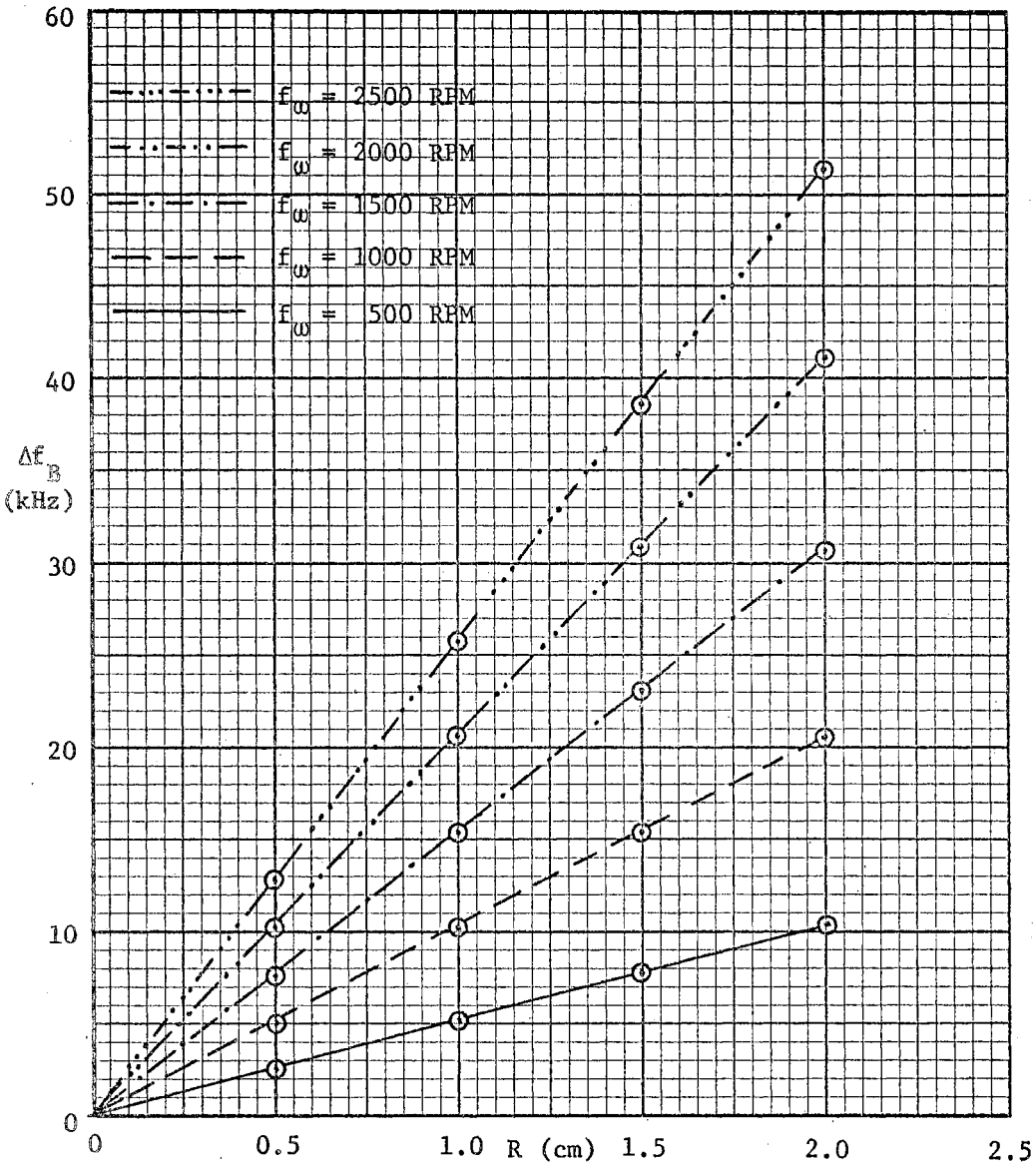

Figure 34. Beat Frequency vs. Frequency of Rotation for Fused Silica With Data Taken for Constant Frequency of Rotation

tained, i.e. R was reset twenty times. The total variations in the computed data were smaller for the data taken with variable R (as opposed to variable f_ω and constant R) as would be expected due to the statistical smoothing of the variations due to randomness in resetting R. These comparisons are presented shortly.

The data which was presented in Figure 32 (where Δf_B was plotted as a function of f_ω) and tabulated in Table XVII is plotted in Figure 34 for Δf_B as a function of R. The data points are those tabulated in Table XVII. The points are connected in families of constant f_ω. The beat frequency Δf_B data varies quite linearly with R for constant f_ω as predicted by Eq. (2-41a).

An exhaustive computer analysis was made of all the data using an IBM 360 computer which employed standard company programs at the Continental Oil Company Computer Center in Ponca City. Since the data was expected to behave linearly, a computer program was used which employed standard least squares linear regression methods. The program fitted a least squares line to the data and printed out the parameters m, Δm, b, Δb, r, and r^2 as well as the calculated value of Δf_B and DELTA Δf_B where DELTA Δf_B is the difference between Δf_B of each data point and the corresponding calculated Δf_B. The terms m and b are the slope and y-axis intercept, respectively, of $y = mx + b$ where x is the coordinate of f_ω or v_a and y is the coordinate of Δf_B. The terms Δm and Δb are the standard deviations of the estimated values of m and b, respectively, from the data. Loosely speaking, these terms are the standard errors in m and b. The term r is the simple correlation coefficient between the data and the least squares fitted line, and r^2, the coefficient of determination, represents the fraction of variation of the mean which is

accounted for by the linear model. The parameters m, b, Δm, Δb, r, and r^2 are tabulated in Table XIX while the calculated values of Δf_B are tabulated in the tables which accompany the respective plotted data.

In general, for data plots where the standard deviation Δb is smallest, the quantity b is closest to the calculated value from Eq. (2-27) (see Table XIX), and except for two extrapolated values, always within $\pm \Delta b$ of the value calculated from Eq. (2-27). This indicates quite strongly that only random errors are involved in b.

The equations which define the standard deviations Δm and Δb are

$$\Delta m = \left[\frac{\sum_{i=1}^{n} (y_i - \tilde{y})^2}{(n-2)} \; \frac{n}{[n \sum_{i=1}^{n} x_i^2 - (\sum_{i=1}^{n} x_i)^2]} \right]^{1/2} \qquad (5\text{-}6)$$

and

$$\Delta b = \left[\frac{\sum_{i=1}^{n} (y_i - \tilde{y})^2}{(n-2)} \; \frac{\sum_{i=1}^{n} x_i^2}{[n \sum_{i=1}^{n} x_i^2 - (\sum_{i=1}^{n} x_i)^2]} \right]^{1/2} \qquad (5\text{-}7)$$

where (x_i, y_i) is the raw data, $\tilde{y}$ is the fitted value of y for x_i, and n is the number of points of raw data.

Each data curve presented was analyzed separately. To obtain one representative set of data for determining α, all of the fused silica data was lumped into one program. Since, as mentioned previously, the gas flow data was useful in determining the bias due to the earth' rotation, values of b and Δb were computed from the data in Figure 24 and Figure 25, respectively. The values of b obtained with the gas flows are in closer agreement with the true value of b than those obtained using fused silica, and the margins Δb are also smaller for the gas flows. The smaller variations for gas flows are primarily due to the

TABLE XIX

COMPUTED TERMS FOR A LEAST SQUARES FIT TO A STRAIGHT LINE $y = mx + b$

Data Identification		m (10^4 m^{-1})	Δm (10^1 m^{-1})	b (Hz)	Δb (Hz)	r	r^2
Figure 24		--	--	48	14	.999932	.999865
Figure 25		--	--	50	10	.999906	.999811
Figure 28	R = 1.00 cm	1.728	3.5	20	26	.999984	.999967
Figure 28	R = 2.00 cm	1.710	3.9	50	49	.999966	.999932
Figure 30	R = 1.81 cm	1.709	1.4	54	22	.999997	.999994
Figure 32	R = 0.50 cm	1.731	8.1	28	41	.999966	.999931
Figure 32	R = 1.00 cm	1.730	2.0	33	17	.999998	.999997
Figure 32	R = 1.50 cm	1.730	4.2	- 14	62	.999991	.999982
Figure 32	R = 2.00 cm	1.734	2.6	- 13	51	.999997	.999993
Figure 33	All Data	1.732	1.4	12	18	.999994	.999989
Figure 21	All Data	1.711	1.8	45	23	.999981	.999962
Figure 33 Figure 21	All Data	1.716	1.6	33	21	.999976	.999952

smooth flowing nature of the gas as opposed to the vibrations produced in the solid fused silica when it is rotated in an imperfect rotator. The gas flow values for b of 48 ± 14 Hz and 50 ± 10 Hz agree very well with the calculated value of b = 43 Hz. Values of b for fixed R and variable f_ω (Figure 29 and Figure 30) gave values of b which are within a few Hertz of the true value of b. The value of b obtained from the composite data (Figure 31) differs from the true value of b by 2 Hz with b = 23 Hz. The b data for f_ω fixed and R variable is not nearly so good, varying from b = -14 Hz to b = 33 Hz with Δb as great as 62 Hz. However, these larger deviations are to be expected since in this case b was determined from an extrapolation of curves which lie entirely to one side of the y-axis, while in the previous case b was determined using data which was symmetrically distributed on either side of y. The final tabulated value of b = 33 ± 21 Hz is the value obtained from a composite of all the data, and, hence, is an indication of system performance.

The slope of each of the plots for fused silica was computed in terms of the beat frequency (Hz) vs. the velocity of the medium (cm/sec) even though several plots are of Δf_B vs. f_ω. The maximum deviation for the m from the average value of all the data is + 1% to - 0.4%. The standard deviation Δm is typically less than 0.4 Hz sec cm^{-1} or 0.2% of m, and for the composite of all the data is less than 0.2 Hz sec cm^{-1} or 0.1% of m. Hence, since α is directly proportional to m, the errors contributed to α determination due to randomness in m should be less than 0.1%

The values of the correlation coefficient r, all being greater than 0.9999, indicate a high degree of fit between the data and a

straight line. This further substantiates the expectation that a linear relationship would hold and that the data could be fitted to a straight line. The coefficient of determination r^2 indicates that the linear model accounted for 99.98^+ % of the data variation for the gas flow measurements and 99.993^+ % of the data variation for fused silica measurements.

The experimental drag coefficient α can be calculated from the m data in Table XIX using Eq. (2-49b). Values of α calculated from Table XIX are listed in Table XX where they are compared to the Fresnel drag coefficient without dispersion α_1 and the Fresnel drag coefficient including dispersion α_2 (i.e. the Lorentz drag coefficient). The values of α_1 and α_2 obtained by using the relations which follow Eq. (2-1) and in Eq. (2-16) are $\alpha_1 = 0.5290$ and $\alpha_2 = 0.5423$. The difference between α_1 and α_2, which is due solely to the dispersion term, is 2.5% of α_1. This difference should be reflected in a comparison of α with α_1 and α_2. The percent deviation of α from α_1 and α_2 is tabulated for each of the curves as well as for the composite data from all of the curves. The variation of α from α_2 is significant only in two of the curves for fixed R and variable f_ω. This is quite probably due to errors in R for these two curves, as an error in R is reflected directly in m and, hence, in α. It is significant that the deviation of α from α_2 for constant f_ω and variable R is both consistent and quite small. This indicates that the statistical averaging of the R settings did, in fact, reduce the total fluctuations in the data. One value of α representing all of the data obtained with fused silica was obtained from the corresponding value of m in Table XIX, and the standard deviation, in loose terms, was obtained using Δm. The value of α obtained ($\alpha = 0.5406$) deviated

TABLE XX

COMPARISON OF EXPERIMENTAL AND THEORETICAL DRAG COEFFICIENTS

Figure Number	R (cm)	α	Percent Deviation From Theoretical Value		Error as a Percentage of the Dispersive Term
			$\frac{\alpha - \alpha_1}{\alpha_1} \times 100$ (%)	$\frac{\alpha - \alpha_2}{\alpha_2} \times 100$ (%)	$\frac{\alpha - \alpha_2}{\alpha_2 - \alpha_1} \times 100$ (%)
28	1.00	0.5416	+ 2.38	- 0.13	5.3
28	2.00	0.5359	+ 1.30	- 1.18	48
30	1.81	0.5356	+ 1.25	- 1.24	54
32	0.50	0.5428	+ 2.61	+ 0.09	3.8
32	1.00	0.5425	+ 2.55	+ 0.04	1.5
32	1.50	0.5422	+ 2.50	- 0.02	0.8
32	2.00	0.5435	+ 2.74	+ 0.22	9.0
All Data		$\bar{\alpha}$ = 0.5406 (σ = 0.003)	+ 2.19	- 0.31 (± 0.5)	13

from α_2 by - 0.3% and from α_1 by 2.2% with a standard error of $\pm$ 0.5%.

Also listed in Table XX is the difference between α and α_2 as a percentage of the dispersive term. The difference values for variable R have a mean of less than 4%, while the percentage difference of α as computed from all the data is 13%. This is be compared with the results that Zeeman obtained over a period of eight years using conventional interferometry where his values agreed with α_2 to within approximately 20% at 6328 Å.

V.4. Liquid Measurements

All attempts to obtain oscillation of the ring with a liquid in the lasing path were unsuccessful. As a result, no determination of the drag coefficient for any liquids could be attempted. However, the reasons for lack of success will be discussed here and suggestions for future improvements to overcome these problems will be presented in Chapter VI.

The primary reason for failure to obtain oscillation is that the losses due to absorption, scattering, and depolarization acting either singularly or in combination are greater than the available gain at 6328 Å with the plasma tube that was available. Positive results had been expected due to the fact that Macek et al (1964) had obtained oscillation with a sample of carbon tetrachloride internal to a ring laser cavity. However, there are several distinct differences in their system and the one employed here. The ring used by Macek et al used a 3 meter plasma length operating at 1.15 μ and had an effective sample path length of 5.8 mm. The ring used for this work used a 1 meter plasma tube at 6328 Å and an effective sample length of 15.5 mm. Since

the gain of a plasma tube per unit length is approximately the same at 1.15 μ as at 6328 Å (Rigden and White, 1963), the useful gain of Macek's system could easily be eight times as great as for the system used here. The effect of the wavelength change on Rayleigh scattering is also quite noticeable. Since the scattering losses are proportional to λ^{-4}, any losses due to Rayleigh scattering at 6328 Å would be nearly eleven times as great as at 1.15 μ.

To determine roughly the loss due to the beam traversing the sample, equipment was set up to measure the loss as shown in Figure 21. A Spectra-Physics 132 circularly polarized laser was used to project a beam around the ring including through the liquid. After reflection off a front surface mirror, the beam was polarized linearly to simulate the conditions appropriate to operation of the ring laser. Measurements were taken for the empty cell as well as for the cell when filled separately with each of the three most promising liquids. The most promising liquids were chosen from the specifications in Table XXI. Desireable features are a large $dn/d\lambda$, n(liquid)/n(fused silica) ≈ 1.00, low optical absorption and scattering losses, and availability in pure form. Considering these features, the three most promising liquids in order of probable success were chosen to be carbon tetrachloride, toluene, and benzene, respectively. The results of the loss measurements which were taken for the liquids in the cell are tabulated in Table XXII. The loss of 0.1% due to the empty cell was sufficiently small for oscillation to take place quite readily, as was easily verified by using the empty cell in the ring. However, the power losses due to the liquids of 1.0% to 1.1% are probably too great for operation of this particular ring. Depolarization of the incident light could not read-

ily be measured, but would increase the losses. To ascertain that the losses were great enough that ring laser operation could definitely not be expected, the liquid filled cells were inserted internally in a He-Ne laser which exhibited a gain greater than 10% (see Figure 36). Under no conditions was oscillation achieved with this equipment. This experiment does not imply that the losses in the liquid were 10% because the liquid cell was inserted with its faces perpendicular to the beam so that surface losses could amount to an 8% power loss. The implication is, however, that the combined losses certainly exceeded 1% and were quite probably greater than 2%.

TABLE XXI

INDEX OF REFRACTION AND DISPERSION OF SELECTED LIQUIDS

Liquid	$n(0.6328\mu)$	$dn/d\lambda$ (μ^{-1})	$\frac{n(liq.)}{n(SiO_2)}$
water	1.3318	-0.028	0.9140
isoamyl alcohol	1.4071	-0.030	0.9657
amyl alcohol	1.4082	-0.032	0.9664
cyclohexane	1.4298	-0.031	0.9813
chloroform	1.4448	-0.038	0.9916
cyclohexene	1.4475	-0.040	0.9934
carbon tetrachloride	1.4619	-0.085	1.0033
toluene	1.4951	-0.062	1.0261
benzene	1.4983	-0.072	1.0283
chlorobenzene	1.5216	-0.076	1.0443
phenol	1.5389	-0.083	1.0561
nitrobenzene	1.5484	-0.104	1.0627
carbon disulfide	1.6234	-0.140	1.1141

TABLE XXII

TRANSMISSION LOSS THROUGH LIQUID CELL

Empty Cell		Carbon Tetrachloride		Benzene		Toluene	
Trial	Loss(%)	Trial	Loss(%)	Trial	Loss(%)	Trial	Loss(%)
1	0.02	1	0.90	1	1.10	1	0.88
2	0.10	2	0.96	2	1.46	2	0.90
3	0.06	3	1.34	3	1.56	3	0.96
4	0.14	4	1.16	4	1.54	4	0.94
5	0.18	5	1.26	5	1.00	5	1.14
6	0.06	6	0.88	6	0.82	6	1.06
7	0.12	7	1.44	7	0.80	7	1.04
8	0.22	8	0.80	8	0.90	8	1.14
9	0.08	9	0.80	9	0.82	9	0.96
10	0.16	10	1.08	10	0.80	10	1.24
		11	0.82	11	1.10	11	1.50
				12	1.18		
$\overline{\text{Loss}}$(%)	0.11		1.0		1.1		1.1
σ_{Loss}(%)	0.06		0.2		0.3		0.2

The fact that scattering losses were present was quite apparent when the liquid was viewed while a polarized laser beam at 6328 Å was being shined through the cell. The beam was polarized so that the E vector was in the plane formed by the incident beam and a normal to the front surface of the cell. This polarization duplicates the state of polarization which normally exists in this ring laser. The observation is portrayed in Figure 35 where the beam is incident from the left on the cell containing the liquid sample. A small, but noticeable, amount of light is scattered at the air-quartz (fused silica) interfaces due

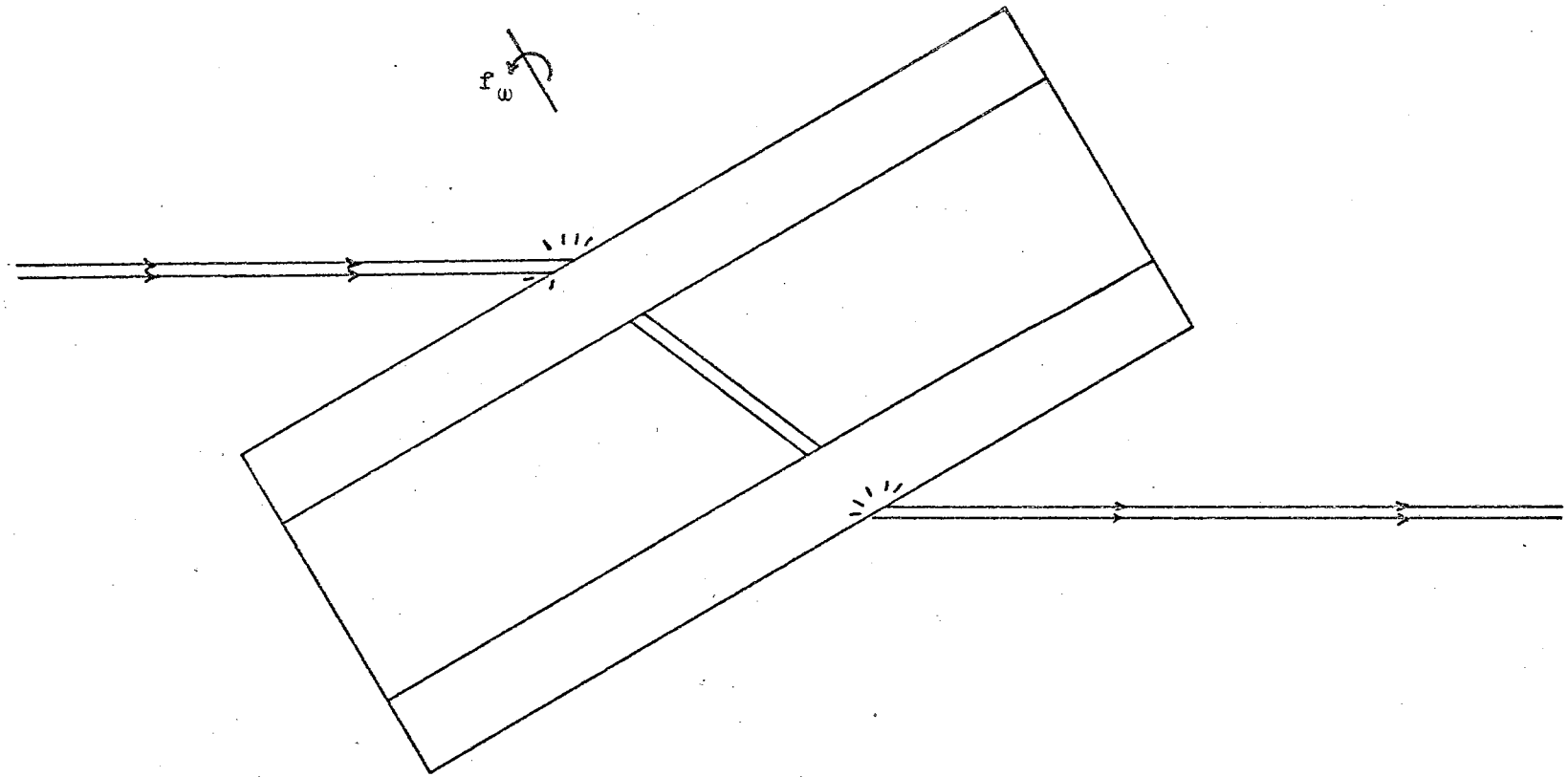

Figure 35. Diagram of Side View of Liquid Cell Illustrating Scattering Observed During Transmission Loss Measurements

to surface irregularities. In the quartz windows, the beam is completely invisible while within the liquid the beam is observed as a cylindrical, illuminated volume whose cross-section is that of the beam. There are no scattering or reflection losses at the quartz-liquid interfaces for the case of carbon tetrachloride. For toluene and benzene, only small reflection losses were apparent. Upon close visual inspection of the liquid, one sees only the gross scattering, i.e. the individual scattering centers are not observed as such. It is felt that this scattering is not a characteristic of the pure liquid, but is probably due to a minute particulate suspension. The most probable type of suspension would be air entrapment in the form of very small "bubbles" (diameter $< 1\ \mu$). Centrifuging was tried as a means of reducing the number of scattering centers. Each liquid sample was centrifuged up to 4000 RPM for at least fifteen minutes. The carbon tetrachloride sample was spun at 2500 RPM for one hour. In each case the secondary laser beam was shining through the liquid as illustrated in Figure 21 and Figure 35. During the first one or two minutes, an occasional "flash" could be seen as particulate matter crossed the beam. This, however, never occurred after the initial one to two minutes of centrifuging. The bulk scattering retained its original intensity as observed visually both during and after the centrifuging. Hence, the source of the bulk scattering was not centrifuged out. It is felt that the most probable type of suspension that could be responsible for this type of bulk scattering would be air entrapment in the form of very small "bubbles" (diameter $< 1\ \mu$).

CHAPTER VI

CONCLUSIONS AND SUGGESTIONS FOR IMPROVEMENT

VI.1. Conclusions

The area of interest examined in this work was to determine the effect of the dispersive term on the Fresnel drag coefficient. This was done by comparing the results of many experiments with the theory of the Fresnel drag coefficient both neglecting and including dispersion. The equipment chosen for these experiments generally gave both good results and precision. An exception on precision was the vernier device used for determining the radius of rotation for the rotating medium which contributed the largest single source of error, an error which ranged upward from 0.5%. Other measurement errors contributed only minor errors. The use of statistical averaging of the data further reduced the effect of the errors. Hence, under optimum conditions, the total errors involved in these measurements were less than 0.5%.

The data taken on flowing nitrogen gas demonstrated the capabilities of the ring laser and the frequency detection and processing equipment. The frequency bias of 43 Hz due to the earth's diurnal rotation was quite apparent in all the data, and was measured to $\pm$ 25% (i.e. $\pm$ 10 Hz) using the gas flow. It was apparent that special considerations must be given to determining the velocity of the gas flow

if the absolute magnitude of the drag coefficient is to be calculated from the data. In particular, the flow profile must be known quite well (Fenster et al, 1968).

The measurements performed on a rotating optic flat of fused silica gave an experimental drag coefficient α such that the Fresnel drag coefficient (neglecting dispersion) α_1 was not included in $(\alpha \pm \Delta\alpha)_{exp}$, whereas α_2, the Lorentz drag coefficient (which includes dispersion effects), was included. In fact, α agrees with the Lorentz drag coefficient to within the experimental error of 0.5%. Furthermore, the error between the experimentally measured drag coefficient and the theoretical Lorentz drag coefficient (expressed as a percentage of the dispersive term) of 13% is significantly smaller than the 20% accuracy in the red portion of the spectrum reported as the result of eight years' work by Zeeman (1914, 1915, 1920). Also, the method used by Zeeman can be improved only slightly with present techniques (Sommerfeld, 1954), whereas the method used here can very probably be refined to give an improvement in accuracy by a factor of 10 or more (see also Section II. 3.7.). Suggestions for these refinements will be given in Section VI.2. The dispersive term (which is not included in Fresnel's drag coefficient) of the drag coefficient changes the value of the drag coefficient by 2.5%. The very good agreement of the data over wide rotation ranges with linear data fitted curves illustrated the lack of angular acceleration dependent terms in the drag coefficient and substantiated the proposal of creating a tangential velocity component of the medium by rotating the medium.

Liquids proved to be more difficult to measure due to the larger optic losses involved. These losses, being larger than anticipated,

prevented oscillation of the ring laser when it contained a liquid sample and, hence, precluded any determination of the drag coefficient for liquids. For the three liquids tried (carbon tetrachloride, benzene, and toluene) the power losses on transmission through 15.5 mm of sample were determined to be greater than 1% and, in addition, depolarization of the incident beam occurred causing further losses. It was noted, however, that the indices of refraction were quite well matched between the fused silica windows on the liquid cell and the liquids contained. Also, the equipment for rotating the liquid to obtain a linear tangential velocity component operated quite satisfactorily in practice. Suggestions for improving the equipment used and for overcoming the problems which prevented successful operation with the liquids will be presented in the next section.

VI.2. Suggestions for Improvement

There are several areas where state-of-the-art devices could produce quite favorable improvements. The most notable improvement could be made in the vernier device used for determining the radius of rotation. Translation stages and/or micrometer drives are now available for travels of up to two inches and/or resolution to 0.025 microns (see Table XXIII). These could improve the determination of the radius by a factor of 4000 so that the associated error contributes less than a 0.001% error to the drag coefficient. The next most significant improvement could be made in the accuracy and stability of the beat frequency measurements. These measurements were made to $\pm$ 10 Hz accuracy here, but the state-of-the-art seems to be about $\pm$ 0.1 Hz (Killpatrick, 1967). However, very stringent requirements must be put on the ring

TABLE XXIII

X-Y TRANSLATORS

Company and Location	Model	Travel (in)	Resolution (micron)	Price
Coherent Optics, Fairport, N. Y.	424	0.500 x 0.500	1.3	$ 297
Areoptix Tech., Plainview, N. Y.	-	2.00 x 2.00	2.5	350
Oriel Optics, Stamford, Conn.	B-62-60	0.500 x 0.500	1	270
Oriel Optics, Stamford, Conn.	B-62-80	0.500 x 0.500	0.025	420
Kulicke and Soffa, Fort Washington, Pa.	-	0.5 x 0.5	2.5	-
Lansing, Ithaca, N. Y.	20.127	2.0 x 2.0	2.5	300

laser to achieve this type of readout accuracy. The beam path and reflecting surfaces must not provide any noticeable contribution to the frequency measurement which implies that both an evacuated path must be used and the ring laser must be maintained extremely vibration free (Killpatrick, 1967). It would undoubtedly be necessary to greatly increase the mass of the lower isolation table. In lieu of this approach or in association with it, another desirable feature would be to improve the techniques for detecting the beat frequency optically. The optical mixer appeared to work quite satisfactorily, but is a possible source of beat frequency broadening. The use of a combiner prism would alleviate the broadening problem, but might introduce stringent geometrical restrictions on the ring configuration. The optimization of the optical detector and use of an extremely narrow bandpass filter would also both contribute to better system performance. Although an extra red-sensitive photomultiplier was found to be the optimum detector for this system, it is probable that the use of a cooled solid state detector used in conjunction with a high gain op amp all in one compact, shielded case might allow for increased sensitivity and/or improved signal-to-noise ratio. One particular combination might be an EG&G SGD -100A diode and EG&G HA-100 op amp. The use of a narrow bandwidth optic bandpass filter over the detector would also reduce the effects of stray radiation and hopefully help to further improve the signal-to-noise ratio.

The reliance on manufacturer specification of the index of refraction could be eased if each sample whose index was desired was actually measured under controlled conditions at some well equipped laboratory. Under controlled conditions, the index of refraction could readily be

ascertained to an accuracy of ± 0.000001. This service should be available for a nominal fee from the National Bureau of Standards or from manufacturers of quality optical materials such as General Electric, Bausch and Lomb, etc.

The velocity determination used in this work was quite satisfactory. It should be a straightforward procedure to determine the angular rotation to within ± 0.1 RPM up to 10,000 RPM or more by the method used here even though these limits were not consistently achieved in this work. Also of importance at high rotation rates is the degree of balance of the rotating element. The elements used here were not balanced and did exhibit some moderate vibration at certain rotation rates. An advisable procedure for achieving very smooth, high angular rotation rates might be to have the entire rotating element dynamically balanced as a unit. This would certainly allow data to be obtained up to 10,000 RPM rather than being limited to 2500 RPM as was the case here.

Another area in which improvements could be made is the ring laser characteristics. The beam diameter that intercepts the sample should be as small as possible. This parameter is controlled by choosing the radii of curvature of the mirrors while regarding their geometric placement and providing for TEM_{ooq} mode operation (Fox and Li, 1963; Rigrod, 1965). A computer program to optimize these parameters would be quite valuable. The reflectance of the output mirror could also be optimized to obtain more output power to the detector to hopefully improve the signal-to-noise ratio.

Simple variations of the experiments performed here could include using different wavelengths or using simultaneous s- and p-plane polarizations. Wavelengths of 6328 Å, 1.15 μ, and 3.39 μ are available from

the He-Ne plasma tube by simply interchanging the mirrors. The use of various wavelengths would be quite valuable in verifying the nature and magnitude of the dispersive effects on the drag coefficient. Simultaneous s- and p-plane polarization oscillations are possible by using a plasma tube which incorporates perpendicular anti-reflection coated windows (Bagaev et al, 1966). This is a state-of-the-art plasma tube design. More sophisticated and long term projects utilizing the ring laser could involve further checks on relativity theory and on gravitation theory as mentioned elsewhere by Rosenthal (1962), Heer (1964), and Post (1967).

BIBLIOGRAPHY

Aharoni, Joseph. The Special Theory of Relativity. Oxford: Clarendon Press, 1959.

Anderson, James L. Principles of Relativity Physics. New York: Academic Press, 1967.

Bagaev, S. N., Y. V. Troitskii, and B. I. Troshin. "The Polarization of Radiation and the Frequency Characteristics of Ring Lasers With a Triangular Resonator." Opt. Spectr. USSR. 1966, 420-421.

Bergmann, Peter G. Introduction to the Theory of Relativity. New York: Prentice-Hall, Inc., 1942.

Born, Max, and Emil Wolf. Principles of Optics. New York: Pergamon Press, 1965.

Drude, Paul K. L. The Theory of Optics. New York: Dover, 1959.

Fenster, P., and W. K. Kahn. "An Optical Technique for Measurement of Gas Flow Profiles Utilizing a Ring Laser." Applied Optics 7. 1968, 2383-2391.

Fizeau, H. L. Comptes Rendus 33. 1851, 349; "Sur les Hypotheses Relatives a l'Etere Lumineux." Ann. Chem. Phys. 57. 1859, 385-404.

Fox, A. G., and T. Li. "Modes in a Maser Interferometer With Curved and Tilted Mirrors." Proc. IEEE. 1963, 80-89.

Fresnel, A. Ann. Chem. Phys. 9. 1818, 57.

Haress, F. "Die Geschwindigkeit des Lichtes in bewegten Korpern." Dissertation, Jena, 1912.

Heer, C. V. "Resonant Frequencies of an Electromagnetic Cavity in an Accelerated System of Reference." Phys. Rev. 134. 1964, A799-A804.

Hutchings, T. J., J. Winocur, R. H. Durrett, E. D. Jacobs, and W. L. Zingery. "Amplitude and Frequency Characteristics of a Ring Laser." Phys. Rev. 152. 1966, 467-473.

Javan, A., E. A. Ballik, and W. L. Bond. "Frequency Characteristics of a CW He-Ne Optical Maser." J. Opt. Soc. Am. 52. 1962, 96-98.

Jenkins, Francis A., and Harvey E. White. Fundamentals of Optics, 3rd ed. New York: McGraw-Hill, 1957.

Killpatrick, J. "The Laser Gyro." IEEE Spectrum. 1967, 44-55.

Laue, M. "Die Mitfuhrung des Lichtes durch bewegte Korper nach dem Relativitatsprinzip." Ann. d. Phys. 23. 1907, 989-990.

Lorentz, H. A. Versuch einer Theorie der elektrischen und optischen Erscheinungen in bewegten Korpern. Leiden: Brill, 1895; Lectures on Theoretical Physics, Vol. 3. New York: MacMillan, 1931.

Macek, W. M., and D. T. M. Davis, Jr. "Rotation Rate Sensing With Traveling-Wave Ring Lasers." App. Phys. Lett. 2. 1963, 67-68.

Macek, W. M., J. R. Schneider, and R. M. Salamon. "Measurement of Fresnel Drag With the Ring Laser." J. App. Phys. 35. 1964, 2556-2557.

Macek, W. M., and E. J. McCartney. Sperry Engr. Rev. 19. 1966, 8.

Maiman, T. H. "Optical Maser Action in Ruby." Brit. Commun. Electron. 7. 1960, 674-675; "Stimulated Optical Radiation in Ruby." Nature 187. 1960, 493-494.

McFarlane, R. A. "Frequency Pushing and Frequency Pulling in a He-Ne Gas Optical Maser." Phys. Rev. 135. 1964, A543-A550.

Michelson, A. A., and F. W. Morley. Am. J. Sci. 31. 1886, 377.

Podgorski, T.J., and F. Aronowitz. "Langmuir Flow Effects in the Laser Gyro." IEEE J. Quant. Electr., QE-4. 1968, 11-18.

Post, E. J. "Sagnac Effect." Rev. Mod. Phys. 39. 1967, 475-493.

Rigden, J. D., and A. D. White. "The Interaction of Visible and Infrared Maser Transitions in the Helium-Neon System." Proc. IEEE (Corres.) 51. 1963, 943-945.

Rigrod, W. W. "The Optical Ring Resonator." Bell Sys. Tech. J. 1965, 907-916.

Rosenthal, A. H. "Regenerative Circulatory Multiple-Beam Interferometry for the Study of Light-Propagation Effects." J. Opt. Soc. Am. 52. 1962, 1143-1148.

Rosser, W. G. V. An Introduction to the Theory of Relativity. London: Butterworth and Co., Ltd., 1964.

Sommerfeld, A. Lectures on Theoretical Physics, Optics, Vo. IV. New York: Academic Press, 1954.

Yariv, Amnon. Quantum Electronics. New York: John Wiley and Sons, 1967.

Zeeman, P. "Fresnel's Coefficient for Light of Different Colours - First Part." Proc. Roy. Acad. Amsterdam 17. 1914, 445-451; "Fresnel's Coefficient for Light of Different Colours - Second Part." Proc. Roy. Acad. Amsterdam 18. 1915, 388-408; "On a Possible Influence of the Fresnel-Coefficient on Solar Phenomena." Proc. Roy. Acad. Amsterdam 18. 1916, 711-715; "An Optical Method for Determining the Ratio Between the Mean and Maximal Velocities in the Turbulent Motion of Fluids in a Cylindrical Tube. Contribution to the Experiment of Fizeau." Proc. Roy. Acad. Amsterdam 18. 1916, 1240-1247; "Direct Optical Measurement of the Velocity at the Axis in the Apparatus for Fizeau's Experiment." Proc. Roy. Acad. Amsterdam 19. 1917, 125-132; "The Propagation of Light in Moving Transparent Solid Substances. I. Apparatus for the Observation of the Fizeau-Effect in Solid Substances." Proc. Roy. Acad. Amsterdam 22. 1920, 462-465.

Zeeman, P., and A. Snethlage. "The Propagation of Light in Moving Transparent Solid Substances. II. Measurements on the Fizeau-Effect in Quartz." Proc. Roy. Acad. Amsterdam 22. 1920, 512-522.

GLOSSARY OF SYMBOLS

A	Area enclosed by the ring laser. (m^2)
Å	Angstrom = 10^{-10} meter. (m)
b	Bias frequency due to the earth's diurnal rotation; hence, y-axis intercept for the equation $y = mx + b$. (Hz)
Δb	Standard deviation of b from the best fitted curve $y = mx + b$. (Hz)
c	Speed of light in vacuo. ($m\ sec^{-1}$)
d	Thickness of a sample. (m)
f	Frequency below 10 MHz. (Hz)
f_ω	Frequency of rotation. (Hz)
Δf_B	Frequency separation of the contracirculating oscillators in a ring laser, i.e. beat frequency. (Hz)
$\overline{\Delta f_B}$	The mean value of Δf_B for the data considered. (Hz)
h	Perpendicular distance between L_r and the axis of rotation. (m)
l	Length of the light ray from P_o. (m)
L	Optic path length of the oscillator cavity. (m)
L_r	Optic path length through a sample. (m)
$\overrightarrow{L_r}$	Light ray vector. (m)
m	Slope of data plots of Δf_B vs. v_a. ($Hz\ sec\ m^{-1}$, i.e. m^{-1})
Δm	Standard deviation of data points for m from the slope of the best fitted curve $y = mx + b$. ($Hz\ sec\ m^{-1}$)
n	Index of refraction.
N	Integral number.
q	Number of wavelengths around the complete ring laser path.

r	Simple correlation coefficient.
$\vec{r}$	Radius vector. (m)
R	Radius from center of optic flat to beam center. (m)
t	Time in a stationary frame. (sec)
t^*	Time in a stationary frame when transformed into a moving frame. (sec)
t_o^*	Initial time (at the start of an event) in a stationary frame when transformed into a moving frame. (sec)
v	Relativistic velocity of light in a moving medium relative to the observer. (m sec^{-1})
v_a	Linear velocity component of the moving medium parallel to the beam. (m sec^{-1})
v_t	Tangential velocity. (m sec^{-1})
$\vec{v}_t$	Tangential velocity vector. (m sec^{-1})
w	Classic velocity of light (phase velocity) in a medium at rest. (m sec^{-1})
x	Displacement in a stationary frame. (m)
x^*	Displacement in a stationary frame when transformed into a moving frame. (m)
α	Drag coefficient.
α_1	Fresnel drag coefficient (neglecting dispersion).
α_2	Lorentz drag coefficient (Fresnel drag coefficient modified by Lorentz to include dispersion).
β	Angle between the x-axis of the optic flat holder vernier and the plane of the ring. (degrees)
γ	Angle between the cylinder end and the transmitted ray. (degrees)
δ	Angle between a normal to the radius vector and the plane of incidence. (degrees)
Δ	Change in a parameter, e.g. Δz is the change in z.
θ_B	Brewster angle. (degrees)
θ_1	Angle of incidence. (degrees)

θ_n Angle between a normal to the surface of an optic flat and the plane which is both perpendicular to the ring and co-linear with the arm containing the optic flat. (degrees)

θ_t Angle of transmission. (degrees)

$\varkappa$ Constant.

λ Wavelength. (m)

λ_o Free space wavelength. (m)

μ Micron = 10^{-6} meter. (m)

ν Frequency above 10 MHz. (Hz)

$\Delta\nu_{ae}$ Frequency separation of axial modes in an empty oscillating linear laser cavity. (Hz)

$\Delta\nu_{ar}$ Frequency separation of axial modes in the oscillating ring laser. (Hz)

$\Delta\nu_{as}$ Frequency separation of axial modes in an oscillating linear laser cavity which contains a sample. (Hz)

$\Delta\nu_{axial}$ Frequency separation of axial modes in an oscillating laser cavity. (Hz)

ν_{ccw} Frequency of a counterclockwise circulating light beam in the ring laser. (Hz)

ν_{cw} Frequency of a clockwise circulating light beam in the ring laser. (Hz)

σ Standard deviation of a quantity, e.g. σ_z is the standard deviation of the quantity z.

τ Period of one cycle of the axial mode separation frequency. (sec)

φ X-axis direction cosine for $\vec{L}_r$. (degrees)

ξ Y-axis direction cosine for $\vec{L}_r$. (degrees)

ψ Z-axis direction cosine for $\vec{L}_r$. (degrees)

ω Angular velocity. (rad sec^{-1})

$\vec{\omega}$ Angular velocity vector. (rad sec^{-1})

Ω Angular rotation rate of the ring laser with respect to inertial space. (rad sec^{-1})

DELTA Δf_B	Frequency difference between the observed value of Δf_B and the data fitted value of Δf_B. (Hz)
$d\vec{l}$	Line element vector along $\vec{L_r}$. (m)
$dn/d\lambda$	Dispersion, i.e. rate of change of index of refraction with wavelength. (m^{-1})

APPENDIX A

AXIAL MODE EQUATIONS FOR A LINEAR LASER

In an oscillating cavity, the condition that a phase change of $2\pi N$ occurs over one complete path transversal implies

$$\Delta\nu_{axial} = \frac{c}{2nL} \tag{A-1}$$

so that since

$$\Delta\tau = \frac{1}{\Delta\nu_{axial}} \tag{A-2}$$

one has

$$\Delta\tau = \frac{2nL}{c} . \tag{A-3}$$

For a laser cavity of length L (see Figure 36) which contains a plasma tube of length d_1 and index of refraction n_1 with windows of total effective thickness d_2 and index of refraction n_2 and which cavity also contains another medium with length d_3 and index of refraction n_3, Eq. (A-3) becomes

$$\Delta\tau = \frac{2(L - d_1 - d_2 - d_3)n_{air}}{c} + \frac{2d_1n_1}{c} + \frac{2d_2n_2}{c} + \frac{2d_3n_3}{c} . \tag{A-4}$$

For $d_3 \neq 0$ (i.e. the operating cavity with no additional medium) an effective length can be given to the cavity for further computations so that Eq. (A-4) becomes

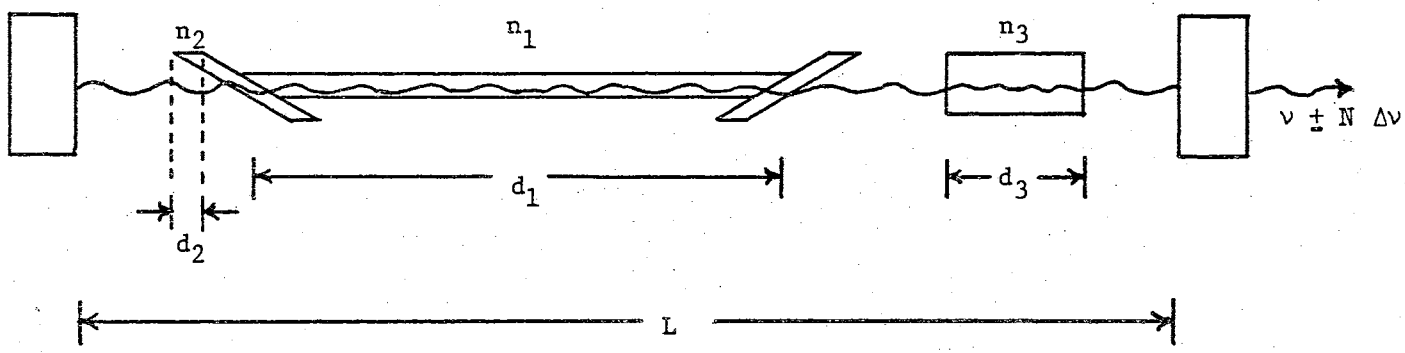

Figure 36. Schematic of a Linear Laser Cavity

$$\Delta\tau = \frac{2\, n_{eff}\, L_{eff}}{c} = \frac{1}{\Delta\nu_{ae}} \qquad \text{(A-5)}$$

where $\Delta\nu_{ae}$ is the axial mode separation for the empty cavity. If $d_3 = 0$, then Eq. (A-4) can be written

$$\Delta\tau = \frac{2\, n_{eff}\, (L_{eff} - d_3)}{c} + \frac{2\, d_3\, n_3}{c} \qquad \text{(A-6)}$$

which becomes for $n_{eff} \approx 1.00$

$$\Delta\tau = \frac{2}{c}\,[L_{eff} + d_3\,(n_3 - 1)] = \frac{1}{\Delta\nu_{as}} \qquad \text{(A-7)}$$

where $\Delta\nu_{as}$ is the axial mode separation for the cavity containing a sample of length d_3 and index of refraction n_3. Rearranging the terms in the second equality of Eq. (A-7) gives

$$n_3 = 1 + \frac{1}{d_3}\left[\frac{c}{2\Delta\nu_{as}} - L_{eff}\right] \qquad \text{(A-8)}$$

which may be put in terms of measurable parameters by substituting for L_{eff} from Eq. (A-5) ($n \approx 1.00$) so that

$$n_3 = 1 + \frac{c}{2d_3}\left[\frac{1}{\Delta\nu_{as}} - \frac{1}{\Delta\nu_{ae}}\right] \qquad \text{(A-9)}$$

or

$$n_3 = 1 + \frac{c}{2d_3}\left[\frac{\Delta\nu_{ae} - \Delta\nu_{as}}{\Delta\nu_{ae}\,\Delta\nu_{as}}\right]. \qquad \text{(A-10)}$$

APPENDIX B

AXIAL MODE SEPARATION MEASUREMENTS FOR THE RING LASER CONTAINING THE OPTIC FLAT AND COMPENSATOR FLAT

The raw data obtained for the ring laser cavity containing the Oriel Optics optic flat and the Special Optics compensator flat is given in Table XXIV, Table XXV, and Table XXVI. Table XXVII is a presentation of the statistics of these axial mode separations. Figure 19 illustrates the apparatus used to obtain the raw data.

TABLE XXIV

FIRST AXIAL MODE SEPARATION FOR THE RING LASER CAVITY CONTAINING OPTICS

First Axial Mode Separation, $\Delta\nu_{arl}$ (MHz)			
92.0216	92.0214	92.0205	92.0197
92.0216	92.0213	92.0208	92.0208
92.0107	92.0216	92.0208	92.0205
92.0211	92.0214	92.0211	92.0209
92.0209	92.0216	92.0213	92.0202
92.0211	92.0210	92.0212	92.0195
92.0206	92.0212	92.0217	92.0193
92.0204	92.0207	92.0216	92.0195
92.0201	92.0215	92.0214	92.0202
92.0206	92.0210	92.0220	92.0204
92.0211	92.0209	92.0219	92.0206
92.0212	92.0206	92.0217	92.0195
92.0213	92.0209		

TABLE XXV

SECOND AXIAL MODE SEPARATION FOR THE RING LASER CAVITY CONTAINING OPTICS

Second Axial Mode Separation, $\Delta\nu_{ar2}$ (MHz)			
184.0383	184.0393	184.0386	184.0391
184.0381	184.0385	184.0399	184.0388
184.0371	184.0381	184.0398	184.0385
184.0383	184.0378	184.0397	184.0384
184.0382	184.0377	184.0387	184.0382
184.0398	184.0377	184.0381	184.0381
184.0384	184.0379	184.0377	184.0383
184.0385	184.0376	184.0383	184.0380
184.0382	184.0373	184.0385	184.0381
184.0387	184.0379	184.0382	184.0398
184.0381	184.0385	184.0383	184.0394
184.0398	184.0385	184.0381	184.0378
184.0396	184.0383	184.0395	184.0373

TABLE XXVI

THIRD AXIAL MODE SEPARATION FOR THE RING LASER CAVITY CONTAINING OPTICS

Third Axial Mode Separation, $\Delta\nu_{ar3}$ (MHz)			
276.0581	276.0581	276.0598	276.0598
276.0597	276.0607	276.0601	276.0610
276.0607	276.0593	276.0613	276.0614
276.0597	276.0601	276.0602	276.0611
276.0606	276.0597	276.0598	276.0587
276.0600	276.0600	276.0614	276.0598
276.0600	276.0585	276.0605	276.0590
276.0599	276.0582	276.0594	276.0578
276.0594	276.0596	276.0601	276.0597
276.0584	276.0588		

TABLE XXVII

STATISTICAL DATA FOR AXIAL MODE SEPARATIONS
IN THE RING LASER CAVITY CONTAINING OPTICS

Term	Number of Data Points	Mean $\overline{\Delta\nu}$ (MHz)	Standard Deviation[1] $\sigma_{\Delta\nu}$ (kHz)	Normalized Mean[2] $\Delta\nu_i/i$ (MHz)
$\Delta\nu_1$	50	92.0209	0.6	92.0209
$\Delta\nu_2$	52	184.0385	0.7	92.0192
$\Delta\nu_3$	38	276.0597	0.9	92.0199

[1]The standard deviation $\sigma_{\Delta\nu}$ is the standard deviation of each sample from the mean, i.e.

$$\sigma^2 = \frac{\sum_{i=1}^{N} (\Delta\nu_i - \overline{\Delta\nu})^2}{N}.$$

[2]The normalized mean is the mean of the i^{th} axial mode separation beat note divided by i.

APPENDIX C

AXIAL MODE SEPARATION MEASUREMENTS FOR A LINEAR OSCILLATOR CONTAINING A SAMPLE

The raw data obtained for axial mode separations in the linear laser cavity (as illustrated in Figure 36) is presented in Table XXVIII and Table XXIX where $\Delta\nu_{aei}$ and $\Delta\nu_{asl}$ are the axial mode separation frequencies for the i^{th} separation in the empty cavity and for the first separation in the cavity containing the Oriel Optics optic flat, respectively. Table XXX presents this data statistically.

TABLE XXVIII

AXIAL MODE SEPARATION FOR THE LINEAR LASER WITHOUT A SAMPLE

$\Delta\nu_{ae1}$ (MHz)	$\Delta\nu_{ael}$ (MHz)	$\Delta\nu_{ae2}$ (MHz)	$\Delta\nu_{ae3}$ (MHz)	$\Delta\nu_{ae4}$ (MHz)
78.3695	78.3642	156.7321	230.1054	313.4454
78.3701	78.3693	156.7335	230.1054	313.4480
78.3662	78.3688	156.7337	230.1032	313.4495
78.3705	78.3658	156.7330	230.1017	313.4376
78.3705	78.3708	156.7333	230.1011	313.4481
78.3648	78.3647	156.7346	230.1078	
78.3654	78.3665	156.7339	230.1058	
78.3691	78.3654	156.7329	230.1044	
78.3669	78.3660	156.7330	230.0995	
78.3660	78.3669	156.7341	230.1098	
78.3661	78.3665			
78.3660	78.3677			
78.3650	78.3653			

TABLE XXIX

AXIAL MODE SEPARATION FOR THE LINEAR LASER
CONTAINING THE ORIEL OPTICS OPTIC FLAT

First Axial Mode Separation, $\Delta\nu_{asl}$ (MHz)			
78.1236	78.1234	78.1207	78.1230
78.1186	78.1251	78.1226	78.1227
78.1224	78.1221	78.1203	78.1190
78.1198	78.1233	78.1205	78.1184
78.1216	78.1235	78.1221	78.1224
78.1208	78.1209	78.1230	78.1243
78.1220	78.1162	78.1210	78.1176
78.1235	78.1204	78.1193	78.1242
78.1186	78.1184	78.1209	78.1231
78.1200			

TABLE XXX

STATISTICAL DATA FOR AXIAL MODE SEPARATION IN THE LINEAR LASER
BOTH WITHOUT AND CONTAINING THE ORIEL OPTICS OPTIC FLAT

Term	Number of Data Points	Mean $\overline{\Delta\nu}$ (MHz)	Standard Deviation $\sigma_{\Delta\nu}$ (kHz)	Normalized Mean $\Delta\nu_i/i$ (MHz)
$\Delta\nu_{ael}$	26	78.3674	0.0025	78.3674
$\Delta\nu_{ae2}$	10	156.7334	0.0007	78.3667
$\Delta\nu_{ae3}$	10	230.1044	0.0031	78.3681
$\Delta\nu_{ae4}$	5	313.4457	0.0048	78.3614
$\Delta\nu_{asl}$	37	78.1213	0.0021	78.1213

APPENDIX D

A VECTOR EVALUATION OF THE VELOCITY COMPONENT OF A ROTATING CYLINDER ALONG AN INTERSECTING RAY

The velocity component of the tangential velocity $\vec{v_t}$ of a rotating cylinder, where the velocity component is directed along a path $\vec{L_r}$ through the rotating cylinder, is specified as v_a and is easily found by the following vectorial considerations. Consider the conditions of Figure 37 where the intersecting ray $\vec{L_r}$ enters the cylinder through one end surface at the point P_o $(x_o,y_o,0)$ and exits the cylinder through the other end surface at the point P_p (x_p,y_p,d). The ray $\vec{L_r}$ has direction cosines of φ, ξ, and ψ (corresponding to the angular departure from the x-, y-, and z-axes, respectively). Consider a Cartesian coordinate system where one end face of the cylinder is the x-y plane and the axis of rotation is the z-axis, positive into the cylinder. The axes form a right-handed coordinate system, and the cylinder is a right cylinder.

The velocity component v_a is determined from

$$v_a = \vec{v_t} \cdot \frac{\vec{L_r}}{|L_r|} \quad . \tag{D-1}$$

Now

$$\vec{v_t} \cdot \vec{L_r} = \int_{P_o}^{P_p} \vec{v_t} \cdot d\vec{l} \tag{D-2}$$

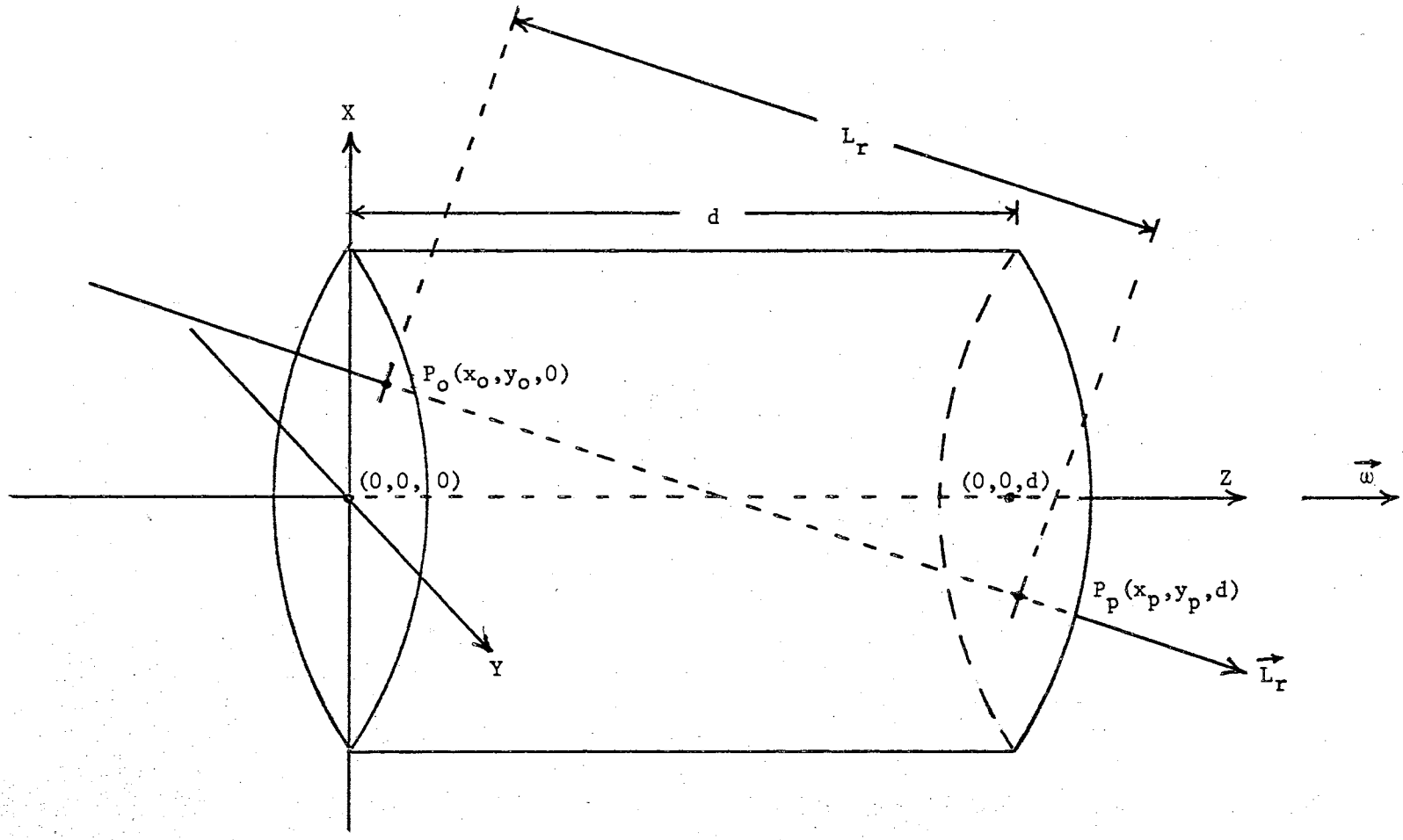

Figure 37. Right Cylinder With Coordinate System Illustrating Beam Penetration

where P_o = point of incidence

P_p = point of exit

$\vec{v_t}$ = tangential velocity vector

$d\vec{l}$ = line element vector along $\vec{L_r}$.

Hence, a determination of v_a requires an evaluation of the integral in Eq. (D-2).

The angular rotation vector $\vec{\omega}$ and the radius vector $\vec{r}$ are defined by

$$\vec{\omega} = \vec{\omega}(0,0,\omega_z) \tag{D-3}$$

$$\vec{r} = \vec{r}(x,y,0) \tag{D-4}$$

and, since

$$\vec{v_t} = \vec{\omega} \times \vec{r} \tag{D-5}$$

one has

$$\vec{v_t} = \begin{bmatrix} i & j & k \\ 0 & 0 & \omega_z \\ x & y & 0 \end{bmatrix} = -\omega_z (y\,\vec{i} - x\,\vec{j}) \tag{D-6}$$

where $\vec{i}$, $\vec{j}$, and $\vec{k}$ are unit vectors along the x-, y-, and z-axes, respectively.

Since the ray $\vec{L_r}$ enters the cylinder at the point P_o $(x_o,y_o,0)$ and has direction cosines φ, ξ, and ψ, $\vec{L_r}$ can be written as

$$\vec{L_r} = (x_o + 1\cos\varphi)\,\vec{i} + (y_o + 1\cos\xi)\,\vec{j} + 1\cos\psi\,\vec{k} \tag{D-7}$$

where 1 = length of the beam from P_o [i.e. $1(P_o) = 0$ and $1(P_p) = L_r$]. Then one can write for Eq. (D-2)

$$\vec{v_t}\cdot\vec{L_r} = \int_{1(P_o)}^{1(P_p)} [-\omega_z(y\vec{i}-x\vec{j})]\cdot[d1\cos\varphi\,\vec{i} + d1\cos\xi\,\vec{j} + d1\cos\psi\,\vec{k}] \tag{D-8a}$$

which, after performing the dot product, becomes

$$\vec{v_t}\cdot\vec{L_r} = \int_0^{L_r} \omega_z[-\cos\ \varphi\ (y_o + 1\ \cos\ \xi) + \cos\ \xi\ (x_o + 1\ \cos\ \varphi)]\ d1. \quad \text{(D-8b)}$$

Simplification yields

$$\vec{v_t}\cdot\vec{L_r} = \omega_z \int_0^{L_r} (x_o\ \cos\ \xi - y_o\ \cos\ \varphi)\ d1 \quad \text{(D-8c)}$$

which is

$$\vec{v_t}\cdot\vec{L_r} = \omega_z\ L_r\ (x_o\ \cos\ \xi - y_o\ \cos\ \varphi). \quad \text{(D-8d)}$$

From Figure 37, one observes that

$$d = L_r\ \cos\ \psi\ . \quad \text{(D-9)}$$

The direction cosines obey the relation

$$\cos^2\ \varphi + \cos^2\ \xi + \cos^2\ \psi = 1 \quad \text{(D-10)}$$

so that Eq. (D-9) can be rearranged to yield

$$L_r = \frac{d}{\sqrt{1 - \cos^2\ \varphi - \cos^2\ \xi}} \quad \text{(D-11)}$$

and Eq. (D-8d) becomes

$$\vec{v_t}\cdot\vec{L_r} = \omega_z\ d\ \frac{(x_o\ \cos\ \xi - y_o\ \cos\ \varphi)}{\sqrt{1 - \cos^2\ \varphi - \cos^2\ \xi}}\ . \quad \text{(D-12)}$$

Eq. (D-11) implies that the drag is determined solely by the entrance point $P_o\ (x_o, y_o, 0)$ and the direction cosines φ and ξ, the angles with respect to the x- and y-axes. Further, since the integrand in Eq. (D-8c) is independent of 1 (i.e. is not a function of x, y, or z), the velocity v_a (which is the component of $\vec{v_t}$ along the ray $\vec{L_r}$) is a constant at all points along any given $\vec{L_r}$. However, v_a will have different values for

different paths of $\vec{L_r}$.

Four separate conditions which are encountered in drag experiments with cylinders will be considered. These are:

Condition 1. $\varphi = \xi = 90°$.

For this condition, the ray $\vec{L_r}$ is parallel to the axis of rotation and Eq. (D-12) yields $\vec{v_t} \cdot \vec{L_r} = 0$ so that no drag would result along $\vec{L_r}$.

Condition 2. $\varphi = 90°$, $\psi = 0_t$.

This is the condition for intended operation as in the experiments reported in this work. If θ_t is the internal transmission angle with respect to the z-axis corresponding to external incidence at the Brewster angle θ_B (with respect to the z-axis also), then Eq. (D-10) implies that

$$\cos \xi = (1 - \cos^2 \psi)^{1/2} = \sin \psi . \tag{D-13}$$

Also, since $\theta_B + \theta_t = 90°$ at the Brewster angle, $\xi = \theta_B$. Hence, for these conditions Eq. (D-12) becomes

$$\vec{v_t} \cdot \vec{L_r} = \omega_z \, d \, x_o \frac{\cos \xi}{\sin \xi} . \tag{D-14}$$

Recalling that $n = \tan \theta_B$ allows one to write Eq. (D-14) as

$$\vec{v_t} \cdot \vec{L_r} = \frac{\omega_z \, d \, x_o}{n} . \tag{D-15}$$

Thus, the velocity v_a is independent of y_o so that a vertical displacement of $\vec{L_r}$ causes no error in v_a or, hence, in the drag.

Condition 3. $\psi = 90°$.

This condition is for $\vec{L_r}$ across the face of the cylinder, or parallel to the x-y plane anywhere in the cylinder. From Eq. (D-10), one has the relation

$$\cos^2 \varphi + \cos^2 \xi = 1. \tag{D-16}$$

If one now defines the center of $\vec{L_r}$ as P_o (x_o,y_o,z_o), and the distance from the axis of rotation [i.e. the point $(0,0,z_o)$] to P_o as h (see Figure 38), then

$$\cos \varphi = - \frac{y_o}{h} \tag{D-17}$$

$$\cos \xi = \frac{x_o}{h} \tag{D-18}$$

and Eq. (D-8d) becomes

$$\vec{v_t} \cdot \vec{L_r} = \omega_z L_r h. \tag{D-19}$$

The result of Eq. (D-19) is always positive, and depends only on L_r and h for constant ω_z. When L_r becomes zero ($\vec{L_r}$ tangent to the cylinder) or h becomes zero (i.e. $\vec{L_r}$ is a radial vector), then from Eq. (D-1) it follows that $v_a = 0$ and the drag is zero. If one introduces

$$h^2 + (L_r/2)^2 = r^2 \tag{D-20}$$

into Eq. (D-19) then

$$\vec{v_t} \cdot \vec{L_r} = 2 \omega_z r h \quad 1 - (h/r)^2 \tag{D-21}$$

which depends only on h (ω_z and r are predetermined) and which has a maximum for $r/h = 1/\sqrt{2}$.

It should be noted that for condition 3, $\vec{L_r}$ enters and exits through the outer surface of the cylinder and does not penetrate either end of the cylinder.

Condition 4. $\vec{L_r}$ passes through the point $(0,0,z_a)$, $-\infty < z_a < \infty$.

If $\vec{L_r}$ is written in the form [see Eq. (D-7)]

$$\vec{L_r} = (x - x_o)\,\vec{i} + (y - y_o)\,\vec{j} + (z - z_o)\,\vec{k} \qquad \text{(D-22)}$$

then $\vec{L_{xy}}$, the vector formed from the projection of $\vec{L_r}$ into the x-y plane (see Figure 39), is given by

$$\vec{L_{xy}} = (x - x_o)\,\vec{i} + (y - y_o)\,\vec{j}. \qquad \text{(D-23)}$$

Now, if $\vec{L_r}$ satisfies $(0,0,z_a)$, then $\vec{L_{xy}}$ must satisfy $(0,0,0)$ so that $\vec{L_{xy}}$ lies along a radial line. Hence, $\vec{v_t}\cdot\vec{L_r}$ can be evaluated by

$$(\vec{\omega} \times \vec{r}) \cdot (\varkappa\,\vec{r}) = 0 \qquad \text{(D-24)}$$

where $\varkappa$ is a constant. By definition, the dot product of two perpendicular vectors is zero. The result is that no net drag results when $\vec{L_r}$ passes through the z-axis.

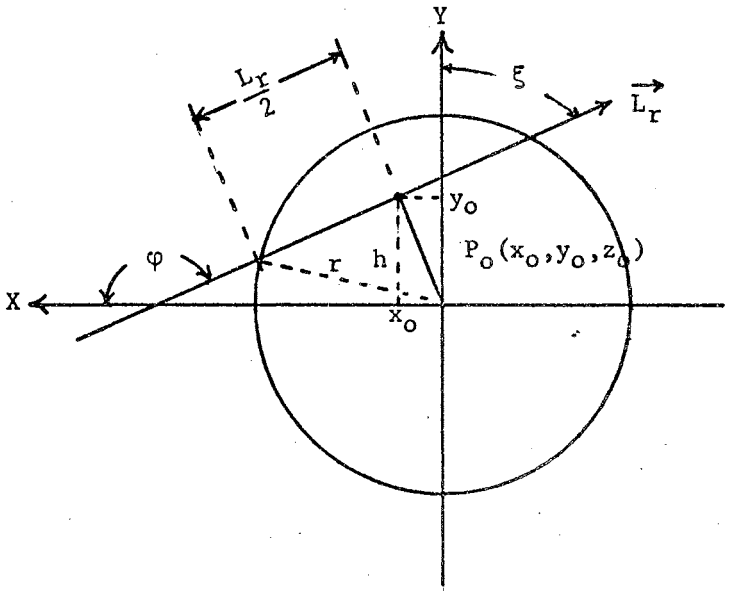

Figure 38. Relationships for $\vec{L}_r$ Parallel to the X-Y Plane

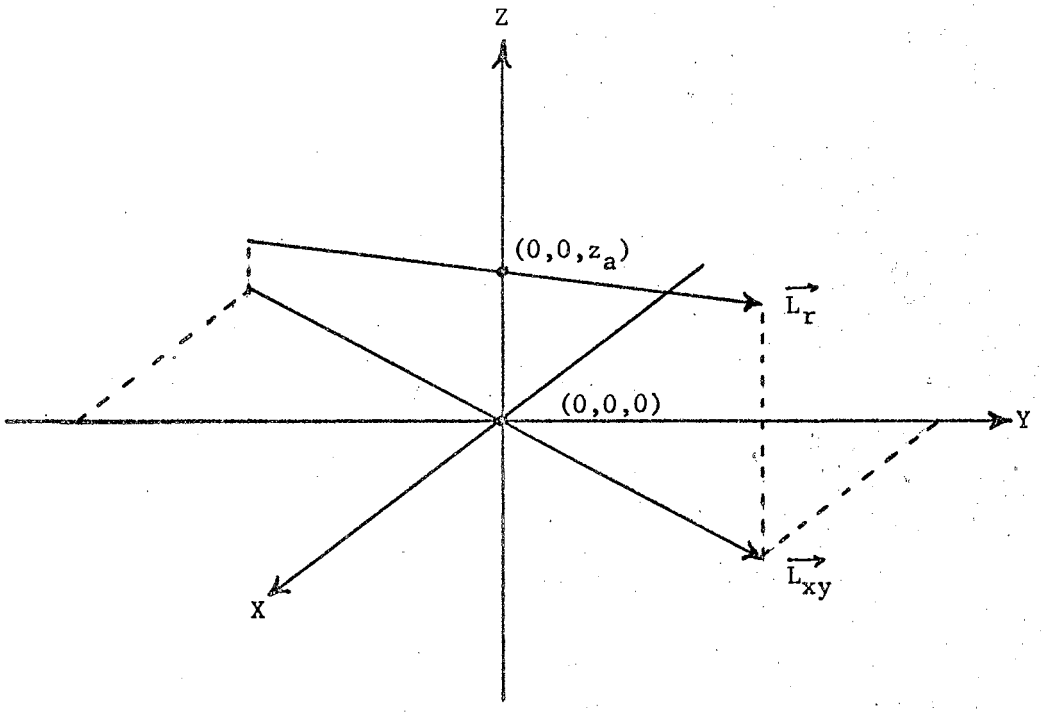

Figure 39. Illustrating $\vec{L}_{xy}$ Generation From $\vec{L}_r$

APPENDIX E

EQUIPMENT USED IN THE EXPERIMENTS

A complete listing of all of the equipment which was used in the experiments reported in this work is given in Table XXXI. The code is designated in the footnote following the table.

TABLE XXXI

A COMPLETE LIST OF THE EQUIPMENT UTILIZED IN THE EXPERIMENTS

Equipment Name	Manufacturer	Model	Code
Plasma Tube	PEK Labs	--	1
RF Transmitter	Viking	Challenger	1
Mirrors	Perkin-Elmer	582-1183 (2 units)	1
Mirrors	Spectra-Physics	140-4 (2 units)	1
Mirror	Perkin-Elmer	582-1185 (1 unit)	1
Mirror	Spectra-Physics	120-1 (1 unit)	1
Iris Diaphragm	Edmund Scientific	40997	1
Granite Block	Texas Granite Corp.	--	2
Isolation Feet	Korfund	LKA-33 (4 units)	2
Isolation Feet	Korfund	LKA-34 (4 units)	2
Beam Splitter	Edmund Scientific	3197	3
Mirror	Edmund Scientific	30286	3
Photomultiplier	RCA	4742	4
Photomultiplier	RCA	931-A	4
Photodetector	Philco	L4501	5
Photodetector	Philco	L4502	5
Photodetector	Philco	L4504	4
Photodetector	EG&G	SGD-100A	4
Operational Amplifier	EG&G	HA-100	4
Prefocused Light	General Electric	253	5

TABLE XXXI (Continued)

X-Y Graduated Mechanical Stage	Cenco	65250	6
Bearing	Split Ball Bearing Co.	3 TKR 41-52-U 0-5 Tight	6b
Bearing	Split Ball Bearing Co.	3 TNCR 41-52-U Free Turning 0.5 Loose	6c
Motor	Electro-Craft	E-350M	6
Motor Control	Electro-Craft	E-350MG	6
$\lambda/20$ Optic Flat - Fused Silica	Oriel Optics	A-43-464-80	6b
$\lambda/10$ Optic Flat - Fused Silica	Special Optics	10-403-2 III P	7
$\lambda/10$ Optic Flat - Fused Silica	Dell Optics	Custom (2 units)	6c
Lubricant - WSe_2	Cerac	1433	6
Compressed Nitrogen	Linde	High Purity, Dry	6a
Wet Test Meter	Curtin	63125	6a
Stopwatch	Heuer	503201	6a
Power Supply	Hewlett Packard	6215A	5
Power Supply	Fluke	413D	4
Constant Voltage Transformer	Sola	150 VA	6
Micro-Microammeter	Keithly	414	4
Interference Filter	Maser Optics	5 Å BW @ 6328 Å	4
Oscilloscope	Tektronix	502 (2 units)	4
Wave Analyzer	Hewlett Packard	310	4
Plug-In	Singer	UR-3	4
Spectrum Analyzer	Singer	MF-5	4
Bandpass Filter	Krohn Hite	335	5
Amplifier	Hewlett Packard	400C	5
Audio Oscillator	Krohn Hite	430AB	4
Electronic Counter	Hewlett Packard	524D	8
Electronic Counter	Hewlett Packard	5243L	5
Electronic Counter	Hewlett Packard	5280A	4
Universal Plug-In	Hewlett Packard	5285A	4
10-100 MHz Mixer	Hewlett Packard	525A	8
100-510 MHz Mixer	Hewlett Packard	525C	8
Digital Printer	Hewlett Packard	562A	4,5
Spectrum Analyzer	Tektronix	1L20	8
VHF Signal Generator	Hewlett Packard	608C	8
Oscilloscope	Tektronix	535	8
Digital Voltmeter	Hewlett Packard	3440A	9
Digital Voltmeter Plug-In	Hewlett Packard	3444A	9
Power Meter	Spectra Physics	401B	9
Power Meter	Optics Technology	610	9
He-Ne Laser (1 mw)	Spectra Physics	132	10
He-Ne Laser (35 mw)	Spectra Physics	125	8,11
Precision Angle Rotator	Special Optics	100-30	11

TABLE XXXI (Continued)

Electronic Air Cleaner	Honeywell	F38A	12
Hypodermic Syringe	Yale	20Y	6c

[1]The following is a designation of the code used: Code Number-Subsystem Equipment Was Used In: 1 - Ring Laser; 2 - Ring Laser Platform; 3 - Optical Mixer; 4 - Δf_B (Beat Frequency) Detection; 5 - f_ω (Frequency of Rotation) Detection; 6 - Moving Medium; 6a - Moving Medium - Gas Flow; 6b - Moving Medium - Solid; 6c - Moving Medium - Liquids; 7 - Compensator; 8 - $\Delta\nu_{axial}$ Detection; 9 - Power Measurements; 10 - Loss Measurements; 11 - n (Index of Refraction) Measurements; 12 - Air Filtration.

VITA

3

Alfred Ted Zavodny

Candidate for the Degree of

Doctor of Philosophy

Thesis: A DETERMINATION OF THE EFFECT OF THE DISPERSIVE TERM ON THE FRESNEL DRAG COEFFICIENT USING A RING LASER

Major Field: Electrical Engineering

Biographical:

Personal Data: Born near Red Rock, Oklahoma, March 10, 1941, the son of Joe and Katie Zavodny.

Education: Attended grade school in Perry, Oklahoma; graduated from Perry High School in 1958; received an Associate in Science degree from Northern Oklahoma College, Tonkawa, with a major in Engineering, in May, 1960; received the Bachelor of Science degree from the Oklahoma State University, with a major in Electrical Engineering, in May, 1962; received the Master of Science degree from the Oklahoma State University, with a major in Electrical Engineering, in August, 1965; completed requirements for the Doctor of Philosophy degree in May, 1970.

Professional Experience: Flight Test Engineer, Autonetics, Summer, 1962; Associate Research Scientist, Continental Oil Company, 1962-1970; Electronics Instructor, Northern Oklahoma College, Spring, 1968; Graduate Research Assistant, Oklahoma State University, Spring, 1969.